Annual Report 1993

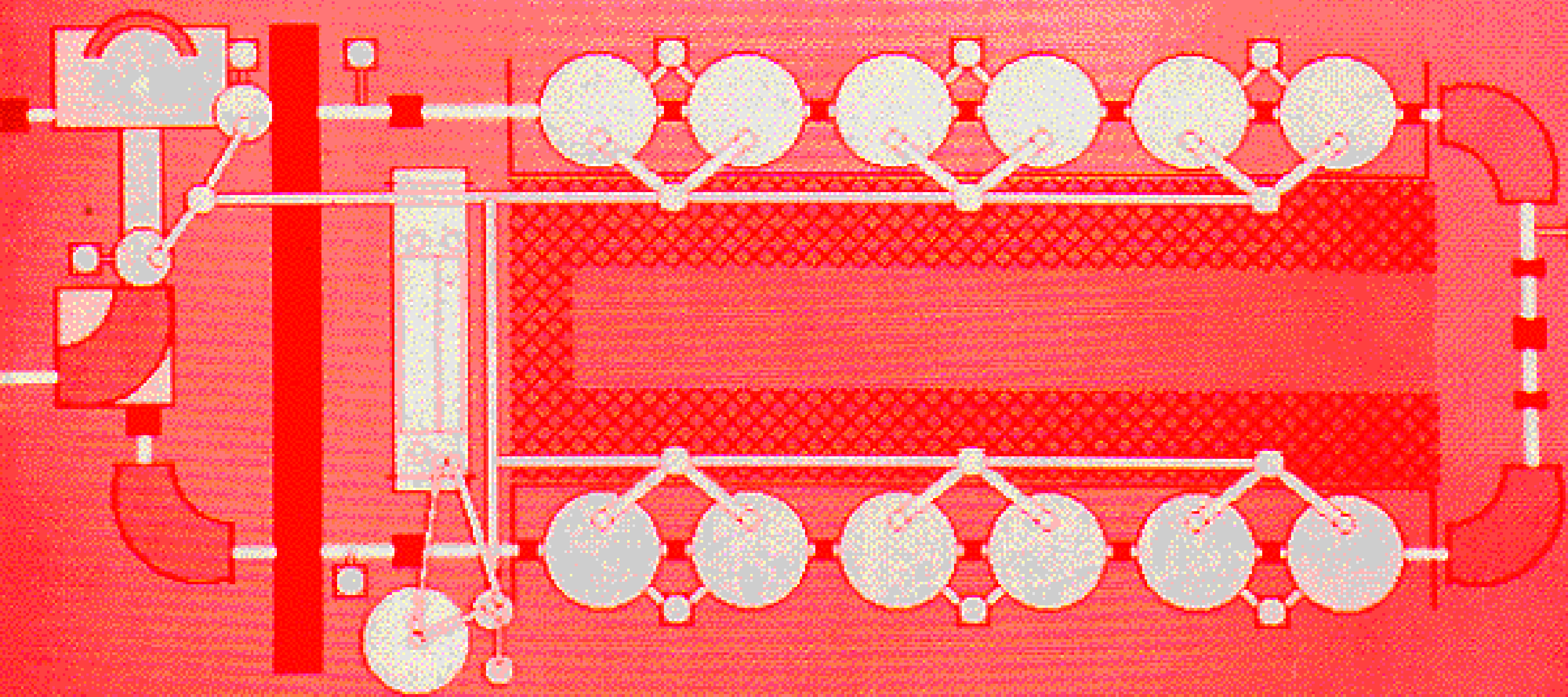

Nuclear Physics Laboratory
University of Washington

ANNUAL REPORT

Nuclear Physics Laboratory
University of Washington
April, 1993

Supported in part by the United States Department of Energy under grant DE-FG06-90ER40537

INTRODUCTION

The Nuclear Physics Laboratory of the University of Washington has for over 40 years supported a broad program of experimental physics research. The current program includes "in-house" research using the local tandem Van de Graaff and superconducting linac accelerators and non-accelerator research in gravitation as well as "user-mode" research at large accelerator facilities around the world. Our local studies of nuclear structure and reactions include nuclear astrophysics, giant resonance (GDR) studies, studies of fusion and high angular momentum phenomena in nucleus nucleus collisions, investigations of fundamental symmetries, AMS studies using the tandem as an ultra-precise mass spectrometer, and a variety of applied activities by outside users. There is an active program at the laboratory to develop instrumentation in support of both the in-house and the user-mode physics activities. The user-mode research includes work at the Argonne ATLAS facility, the CERN SPS, the Indiana Cyclotron, the Michigan State NSCL facility, the Saskatoon electron facility, the Tandar facility in Argentina, and the SLAC facility. Below we present some of the highlights of the UW NPL research program.

In our studies of GDR decay in highly excited nuclei, we've extended our search for highly deformed, very rapidly rotating light nuclei to the A $\sim$ 60 mass region. Again, as in the A $\sim$ 45 mass region, strongly broadened GDR strength distributions are observed, indicating highly deformed compound nuclei. Construction of a simple multiplicity filter is now complete, it will be used in coincidence experiments with high energy γ-rays to provide future information on the nature of the reaction processes.

A re-investigation of the spin distributions in near-barrier fusion of ^{16}O $+^{154}$Sm utilizing rotational state populations as a probe has been completed. The mean spins at lower energies are in better agreement with theoretical expectations than results from previous investigations. A study of the entrance-channel mass-asymmetry dependence of the mean spin in sub-barrier fusion is nearing completion. The results are in remarkable agreement with expectations in contrast to results from another study elsewhere for a similar set of reactions.

A study of the impact parameter dependence of pre-equilibrium proton and light cluster emission at 13.5 MeV/A has been completed. The proton impact parameter dependence is in good agreement with an extension of the nucleon exchange transport model. The ratio of light cluster to proton multiplicities is found to increase with increasing impact parameter, contrary to the expectation from a simple coalescence model. This study is being extended to much higher bombarding energies.

The Eöt-Wash group continued to expand the scope of their investigations. During this last year they published a test of the equivalence principle for ordinary matter falling toward galactic dark matter. They brought into operations a new torsion balance that is surrounded by a rotating three tonne uranium source.

The research in fundamental symmetries focuses on tests of symmetries in atomic, gravitational, and neutron physics. Two neutron experiments are being pursued: the search for an electric dipole moment of the neutron (time reversal symmetry violation) and a measurement of the parity violating interaction between neutrons and alpha particles. The neutron electric dipole moment experiment has been rebuilt to measure simultaneously in the same vessel the spin precession frequencies of trapped neutrons and mercury atoms. The experiment is scheduled to begin data collection in 1994. An apparatus to measure the parity violating rotation of the polarization vector of a neutron beam as it traverses a target of liquid helium is being constructed. Neutron beam time is scheduled at the NIST reactor in 1994. An experiment to measure the electric dipole moment of mercury atoms has been completed recently, in collaboration with Professors Fortson and Lamoreaux, and has yielded the highest precision ever achieved for an electric dipole moment search. A publication is being prepared.

In the accelerator mass spectrometry (AMS) program, work continues under the two-year NSF grant awarded last year as part of the PALE program (Paleoclimates of Arctic Lakes and Estuaries). The first objective, validation of our method of dating pollen from lake sediment and peat bog cores (extraction and purification of pollen, AMS measurement of $^{14}C/^{13}C$), has been achieved; we are now beginning work toward the second objective, tracing the migration of alder and spruce in Alaska following the latest period of widespread glaciation. The accuracy and precision of our measurements have been further enhanced by additional improvements in the high-energy beam transport and detector systems, and by changes in the low-energy beam transport system and in our method of tuning the ion beam through it.

The data from the Saskatoon pion photoproduction experiment have been analysed. The cross sections have a dependence on atomic mass which exhibits effects of Pauli blocking and of absorption of the pions as they exit the nucleus. The model we have used to explain our inelastic pion scattering measurements has been extended to photoproduction and it is able to reproduce the spectral shapes and angular distributions using the same parameters for the pion-nucleus interaction that were used in the scattering calculations.

The NE-18 collaboration at SLAC completed the analysis of the elastic electron scattering on the neutron and proton. The results show a significant deviation from the dipole form factor for elastic magnetic scattering on the proton and establish that the Dirac form factors of the neutron and proton are of comparable magnitude.

We have developed a new proposal for elastic photon scattering on the proton at high momentum transfer (SLAC E147). This second order electromagnetic interaction complements the elastic electron scattering.

The new ultra-relativistic heavy ion (URHI) physics research program of several members of this laboratory, initiated in mid-1990, is now well established, and URHI activities are well represented in this report. In 1991-92 the URHI group participated in two final runs of experiment NA35 at CERN. The approximately 200 gigabytes of time projection chamber (TPC) data collected during these measurements are now being analyzed here. The UW group is participating in development of new equipment and software for experiment NA49, to run at CERN in late 1994. Their activities in the past year have focused on the vertex TPCs and the data acquisition software for that experiment. The UW group is a founding institutional member of the STAR collaboration, which is constructing a solenoidal TPC tracking detector for use at the RHIC collider now under construction at Brookhaven National Laboratory and recently re-scheduled to come into operation in early 1999.

The Laboratory provides beams for a range of uses outside of conventional nuclear physics. This year researchers from the Ball Aerospace Systems Group and the Boeing Defense and Space Groups used beams from the tandem and booster to investigate radiation damage in various electronic devices. We have continued to study cross sections of interest in the production of isotopes for positron emission tomography.

The tandem accelerator has run for 27 years without a major upgrade. This year we requested funding for the installation of a pelletron charging system and spiral beam tubes to improve the quality and quantity of beams from the accelerator. We recently heard that this request will be funded in the near future. The linac continues to serve us well. No major breakdowns have occurred this year, nor have we made any significant modifications.

As always, we welcome applications from outsiders for the use of our facilities. As a convenient reference for potential users, the table on the following page lists the vital statistics of our accelerators. For further information, please write or telephone Prof. W.G. Weitkamp, Technical Director, Nuclear Physics Laboratory, University of Washington, Seattle, WA 98195; (206) 543-4080.

For the first time this year we plan to "publish" an electronic version of this 1993 Annual Report, using the World Wide Web (WWW) system developed at CERN. We have established one of our computers as a WWW server and will maintain an index connecting to PostScript files of the individual articles (including figures in most cases) of this report. The WWW address of the UW NPL entry point is "http://128.95.100.71:80/home_npl.html" and is accessible using a WWW browser such as xmosaic or midaswww. We encourage interested parties to access our Annual Report and other selected publications and documents using this system.

We close this introduction with a reminder that the articles in this report describe work in progress and are not to be regarded as publications or to be quoted without permission of the authors. In each article, the names of the investigators have been listed alphabetically, with the primary author underlined.

John G. Cramer
Editor

María Ramírez
Assistant Editor

Contents

1 Astrophysics

1.1 The excitation energy of the 1_1^- level in ^{14}O and the hot CNO cycle

E.G. Adelberger, A. García* and P.V. Magnus

The hot CNO cycle becomes an important source of stellar energy generation when the $^{13}\mathrm{N}(p,\gamma)$ reaction rate becomes faster than the ^{13}N β-decay rate. The $^{13}\mathrm{N}(p,\gamma)$ rate is dominated by a low-energy s-wave $E1$ resonance that corresponds to the 5.17 MeV first excited state of ^{14}O. For a given stellar temperature and pressure, the reaction rate depends sensitively on the parameters of the low-energy resonance, especially its radiative width, Γ_γ, and its resonance energy, E_R. Several direct determinations[1],[2] of the γ-ray branching ratio and a direct measurement[3] of the resonance strength using a radioactive ^{13}N beam give concordant results that can be combined to yield $\Gamma_\gamma = 3.64 \pm 0.85$ eV. This 'best value' is in excellent agreement with the value $\Gamma_\gamma = 3.1 \pm 0.6$ eV determined indirectly[4] from the breakup of ^{14}O projectiles in the Coulomb field of ^{208}Pb.

On the other hand, a disagreement has arisen concerning the value of E_R. The accepted value[5] for the excitation energy of the ^{14}O first excited state, $E_x = (5173 \pm 10)$ keV, implies $E_R^{cm} = (545 \pm 10)$ keV, while an analysis of $^{13}\mathrm{N}+p$ scattering[3] yielded $E_R^{cm} = (526 \pm 1)$ keV where only the statistical error was quoted, and an unpublished[6] $^{14}\mathrm{N}(^3\mathrm{He,t})$ measurement gives $E_x = (5168.5 \pm 1.8)$ keV, corresponding to $E_R^{cm} = (540.5 \pm 1.8)$ keV. This discrepancy is significant; a 19 keV reduction in the $^{13}\mathrm{N}(p,\gamma)$ E_R^{cm} would increase the reaction rate by 40% at $T = 4 \times 10^6$ K.

We have therefore remeasured the excitation energy of the ^{14}O first excited state, and as a byproduct the mass of the ^{18}Ne ground state which was known with a relatively large uncertainly of ± 5 keV. We used the University of Washington pulsed-beam time-of-flight (TOF) spectrometer in a differential mode, by comparing the TOF of a neutron group of interest to an essentially equal TOF of a well-known calibration group produced in a different target at the same bombarding energy.

First, by comparing TOF spectra for the $^{16}\mathrm{O}(^3\mathrm{He},n)^{18}\mathrm{Ne}(1.88)$ and $^{11}\mathrm{B}(^3\mathrm{He},n)^{13}\mathrm{N}(T=3/2)$ reactions at a beam energy of 7.30 MeV, the mass of the ^{18}Ne 1.88 MeV first excited state was determined. (The Q value of the $^{11}\mathrm{B}(^3\mathrm{He},n)^{13}\mathrm{N}(T=3/2)$ reaction is known to 0.4 keV.) Subtracting the well-known excitation energy of the 1.88 MeV level, the mass excess of the ^{18}Ne ground state is found to be (5315 ± 2) keV. Having established this secondary standard, we then measured the mass of ^{14}O(5.17) by comparing its TOF in the $^{12}\mathrm{C}(^3\mathrm{He},n)$ reaction to that of the ^{18}Ne(3.38) (the excitation energy is again well known) group populated in $^{16}\mathrm{O}(^3\mathrm{He},n)$ at a bombarding energy of 9.00 MeV (see Fig. 1.1). This comparison yielded a ^{14}O(5.17) mass excess of (13168 ± 2) keV, which corresponds to an excitation energy of (5161 ± 2) keV. Our excitation energy is in agreement with the previously accepted value (5173 ± 10) keV because of its large error bar, but not with

*Lawrence Berkeley Laboratory, 1 Cyclotron Road, Bldg 88, Berkeley, CA 94720.

[1] P.B. Fernández *et al.*, Phys. Rev. C **40**, 1887 (1989).

[2] P. Aguer *et al. Proc. Int. Symp. Heavy-Ion Phys. and Nucl. Astrophys. Prob.*, eds. S. Kubono, M. Ishihara and T. Nomura, World Scientific, Singapore (1989), p. 107.

[3] Decrock *et al.*, Phys. Rev. Lett. **67**, 808 (1991) and Nucl. Phys. A **542**, 263 (1992).

[4] T. Motobayashi *et al.* Phys. Lett. **B264**, 259 (1991).

[5] F. Ajzenberg-Selove Nucl. Phys. **A523**, 1 (1991).

[6] T.F. Wang, PhD Thesis, Yale University, 1986.

either the (5154 ± 1) keV value of Decrock *et al.*[3] or the (5168.5 ± 1.8) keV value of Wang.[6] Work on this problem is continuing.

1.2 Gamma-ray branching ratios of proton-unbound levels in ^{37}K

E.G. Adelberger, N. Cabot, P.V. Magnus and H.E. Swanson

The isospin-analog GT strength distributions measured in ^{37}Ca($\beta^+\nu_e$) and ^{37}Cl(p,n) show several large discrepancies.[1] This has raised questions about the reliability of GT strength distributions deduced from intermediate-energy, zero-degree (p,n) cross sections. It should be noted that the the two largest low-energy discrepancies (to the first $1/2^+$ and the second $5/2^+$ states) could be resolved if the E_x = 3.24 MeV $5/2^+$ state in ^{37}K, which is unbound to proton decay by 1.382 MeV decays primarily by γ emission with a 2% proton branch corresponding to a proton spectroscopic factor of only $S_p = 1 \times 10^{-6}$. In this case the β-delayed proton yield would not properly reflect the β^+ branching ratios.

We have studied the decays of low-lying levels in ^{37}K using the ^{40}Ca($p,\alpha p$) and ^{40}Ca(p,αX) reactions at a proton energy of 18 MeV. Here X is either a ^{36}Ar or a ^{37}K. The ^{37}K(p,α) reaction was first examined at 30, 37 and 45 degrees in order to determine an optimum angle for the detector in the coincidence measurement. The ^{40}Ca($p,\alpha p$) reaction was then measured with a thin alpha detector at 37° which tagged events populating various excited states in ^{37}K. Measurement of coincident protons in detectors at +141°, -140° and -90° then allowed an estimate of the fraction of the time the levels proton decay. The ^{40}Ca(p,αX) reaction was measured with the α counter at 120 deg and a coincident counter with an opening angle of 5 degrees placed either at $-34.19°$ or $-36.71°$ to detect the recoiling heavy ion (either ^{37}K or ^{36}Ar). Because the ^{36}Ar's from the proton decay of ^{37}K* have a larger opening angle and a larger energy spread than the ^{37}K's from the gamma decay of ^{37}K*, the measured coincidence efficiency and energy distribution of the heavy ions can be used to determine the decay branching ratios. These data are being compared to a Monte Carlo simulation that includes multiple scattering in the target foil, momentum kick from the decay, and geometry of the target and detectors.

The data analysis is not complete. However, some things can already be inferred. We observe all the levels listed in the compilation[2] up to E_x=3.5 MeV and see two additional levels at E_x=2.97 MeV and E_x=3.27 MeV. The level at E_x=2.97 MeV was observed at lab angles of 30, 37 and 45 degrees, and its kinematics confirm that it is in mass 37. In those data the E_x=3.27 MeV level was in an unresolved triplet. In addition, the sum of the alpha and outgoing proton energies from the ^{40}Ca($p,\alpha p$) data are consistent with both new levels being in ^{37}K.

Our preliminary results on the proton branching ratios of the levels in ^{37}K indicate that the 2.17, 2.29, 2.97 and 3.24 MeV levels predominantly γ decay while the 2.75, 3.08, 3.27 and 3.31 MeV levels predominantly proton decay. This is in agreement with previous information about the 2.17, 2.29, and 2.75 MeV levels where ^{36}Ar+p data are available. After the analysis is complete quantitative results will be available.

It should be noted that even if the low-energy discrepancies between ^{37}Ca β-decay and ^{37}Cl(p,n) are resolved, problems apparently remain at higher excitation energies.

[1] A. García *et al.* Phys. Rev. Lett. **67**, 3654 (1991).
[2] P.M. Endt, Nucl. Phys. **A521**, 1 (1991).

2 Giant Resonances and Photonuclear Reactions

2.1 Giant dipole resonance decays of Cu nuclei formed at high spins and temperatures

A.W. Charlop, Z.M. Drebi, M.S. Kaplan,* M. Kicinska-Habior,† K.A. Snover, D.P. Wells‡ and D.Ye

We continued our studies of the giant dipole resonance decays of nuclei around mass 60. The motivation is to investigate nuclear structure at extreme conditions, particularly the shape evolution as a function of spin and temperature. At nuclear temperatures above 1–2 MeV and spins just below the fission limit, the rotating liquid drop model (RLDM)[1] predicts a shape transition from oblate noncollective to triaxial collective-prolate-like with very large deformation. Our experiments are designed to search for evidence for such a shape transition. We measured the spectral shapes and the angular distributions of the high energy γ rays emitted in the decays of Cu nuclei formed in ^{18}O + ^{45}Sc and ^{32}S + ^{27}Al reactions. Some of these measurements results were presented earlier.[2] Here we will discuss the ^{32}S + ^{27}Al measurements.

^{32}S beams at projectile energies 90–215 MeV (in the center of target) were used with self-supported rolled ^{27}Al targets to form ^{59}Cu compound nuclei at excitation energies ranging from 54 to 111 MeV and with spins up to 43 $\hbar$ in the highest bombarding energy case. Our large NaI spectrometer was used to detect high energy γ rays at five lab angles in the range 40–140 degrees with respect to the beam direction. The angular distributions in the C.M. frame were fitted with a second order Legendre polynomial expansion.

The measured energy spectra in the GDR energy range 13–30 MeV were fitted with the statistical model CASCADE. The Reisdorf level densities formulation was used, and a RLDM moment of inertia with the oblate to triaxial shape change was used to calculate the statistical yrast line. In all calculations complete fusion was assumed, and measured fusion cross sections were used. From these fits, the average cross sections $\sigma_{abs}(E_\gamma)$ for the inverse process of photoabsorption can be extracted.[3] These cross sections together with the extracted angular distribution coefficients a_1 and a_2 are plotted in Fig. 2.1-1. A One-Lorentzian GDR strength function was sufficient to fit the lowest three energy cases. In the highest two energy cases a suggestion of a second peak or shoulder at $E_\gamma \sim 25$ MeV was observed, and a two-Lorentzian strength function was necessary to fit the data.

The deduced GDR width (FWHM) increases from 9.2 MeV to 15.8 MeV in the E_{proj}=90 to 215 MeV range. This broadening of the strength function is due to two effects: the spin-induced equilibrium deformation of the nucleus, and the temperature-induced fluctuations around these equilibrium deformation shapes. Experimentally we can not separate these two effects. Full thermal

*Now at: University of Washington Medical Center, Department of Radiology, Seattle, WA 98195.

†Present address: Institute of Experimental Physics, University of Warsaw, Poland.

‡Now at: Environmental Radiation Section, Department of Health, Radiation Protection Division, Olympia, WA 98504.

[1] S. Cohen, F. Plasil, and W.J. Swiatecki, Ann. Phys. 82, (1974), 557.

[2] Nucear Physics Laboratory Annual Report, University of Washington (1992) p. 14 and Nuclear Physics Laboratory Annual Report, University of Washington (1991) p. 3–6.

[3] $\sigma_{abs} = \sigma_{abs}^{fit}.\sigma_\gamma^{measured}/\sigma_\gamma^{cascade}$.

shape and orientation fluctuation calculations are needed to interpret the data. These calculations are in progress.

The inferred $a_1(E_\gamma)$ coefficients are consistent with zero in the GDR region of interest. However large negative values along with a γ yield are observed at $E_\gamma \leq$12 MeV. This excess γ-yield is due presumably to emission from excited binary or fission reaction fragments.

The angular distribution $a_2(E_\gamma)$ coefficients show, as expected, a negative dip in the low side of the GDR peak. This dip should increase with increasing nuclear deformation, which is not apparent in our data. This can be due to thermal orientation fluctuations which tend to reduce the size of the $a_2(E_\gamma)$ coefficients. Furthermore, the a_2's should turn positive at $E_\gamma > \; E_{GDR}$, for prolate-collective or oblate noncollective shapes, which is not apparent in our data due to the poor statistics.

Fig. 2.1-1. First row: The measured γ cross section, and the CASCADE fits (solid lines). Second and Third rows: The corresponding angular distribution coefficients a_2, and a_1 respectively.

2.2 High energy gamma rays from Ni + Zr reactions

Z. Drebi, M. Kaplan,* K.A. Snover, D. Wells† and D. Ye

We have completed our analysis of the high energy gamma ray spectra measured[1] in the reactions ^{58}Ni +^{92}Zr at E_{lab} = 241 Mev. The purpose of our experiment is to address the possibility of the persistence of large deformation, associated with the near mass-symmetric entrance channel, for times comparable to the compound nuclear lifetime. Our technique is based on an analysis of the decay of the Giant Dipole Resonance. This technique should be particularly sensitive, since GDR decay tends to occur early in the evaporation cascade, and the GDR strength function has a well-known sensitivity to deformation.

Corrections were applied to the measured spectra for the contributions from light target contaminants, and for γ decay following deep inelastic scattering. The light target contaminant corrections were based on spectra measured at E_{lab} = 196 MeV, below the Coulomb barrier for ^{58}Ni + ^{92}Zr, using ^{92}Zr, C and O targets. These corrections amounted to 15–20% in the high energy region. Gamma decay contributions from deep inelastic scattering were estimated from Cascade calculations for the decay of product nuclei produced with cross sections estimated from a published study[2] of deep inelastic scattering of ^{58}Ni + ^{112}Sn. Deep inelastic corrections were important only for $E_\gamma \leq 8$ MeV. We attribute the resulting corrected spectra to decay of the compound nucleus ^{150}Er (E^*= 57 MeV). A single-Lorentzian GDR strength function was varied in a fit of the Cascade statistical model calculation to the data, with the result S=1.4$\pm$ 0.2, E_{GDR} = 13.5 $\pm$ 0.3 MeV and Γ = 8.1 $\pm$ 0.6 MeV. With the possible exception of E_{GDR}, which is somewhat low (typical values are 14–14.4 MeV in this mass region), the fitted GDR parameters are in agreement with systematics.

In order to examine the possibility that anomalous shape persistence effects may depend on the compound nuclear isotope, we have carried out similar measurements for the reaction ^{64}Ni + ^{92}Zr at the same bombarding energy. Preliminary analysis shows that these data, like the ^{58}Ni + ^{92}Zr data describe above, show no evidence for an excess yield of gamma rays at high energies, above the GDR peak, in contrast to previously published results.[3]

*Now at: University of Washington Medical Center, Department of Radiology, Seattle, WA 98195.

†Now at: Environmental Radiation Section, Department of Health, Radiation Protection Division, Olympia, WA 98504.

[1] Nucear Physics Laboratory Annual Report, University of Washington (1992) p. 10.

[2] F.L.H. Wolfs, Phys. Rev. C **36** 1379 (1987).

[3] M. Thoennessen *et al.*, Inst. Phys. Conf. Series # 109, 135 (1990).

2.3 Isospin mixing in highly excited medium mass nuclei

J.A. Behr,* Z. Drebi, M. Kaplan,† K.A. Snover, D. Wells‡ and D. Ye

We have studied isospin mixing in A $\approx$ 60 compound nuclei by comparing the γ-ray production cross sections for GDR decay of ^{60}Zn formed in the fusion of ^{28}Si and ^{32}S at E* $\approx$ 47, 63 and 80 MeV with the cross sections for forming the neighboring N $\neq$ Z compound nuclei ^{59}Cu and ^{58}Ni at similar excitation energies in the ^{31}P + ^{28}Si, ^{32}S + ^{27}Al and ^{31}P + ^{27}Al reactions. Results from the present data indicated $\alpha^2_> \leq 0.1$ at all 3 excitation energies. When the present results are combined with the results of an earlier study of $(\alpha, \alpha), (p, \alpha)$ and (p, p) reactions which indicated $\alpha^2_> \approx 0.4$ at E* $\cong$ 20 MeV, the combined results provide the clearest indication to date of the restoration of compound nuclear isospin symmetry at high excitation energy.[1]

Calculations using the Reisdorf prescription for the level density show that the constant value $\Gamma \downarrow_> = 20$ keV provides a good description of the experimental data. Calculations with the Puhlhofer level density imply a larger value $\Gamma \downarrow_> \sim 40$ keV. Current efforts are focussed on a determination of a best value and an uncertainty for $\Gamma \downarrow_>$.

*Now at: Department of Physics, State University of New York, Stony Brook, Stony Brook, NY 11794.
†Now at: University of Washington Medical Center, Department of Radiology, Seattle, WA 98195.
‡Now at: Environmental Radiation Section, Department of Health, Radiation Protection Division, Olympia, WA 98504.
[1]See also J.A. Behr *et al.* Phys. Rev. Lett., in press.

3 Nucleus-Nucleus Reactions

3.1 Refinements of the nucleon-exchange transport model for the emission of hard photons and nucleons

S. J. Luke,* J. Randrup† and R. Vandenbosch

We have extended an earlier[1,2] nucleon exchange transport model to include proton emission in addition to neutron emission. This extension is relatively straightforward, requiring only additional effects of the Coulomb barrier for the escaping protons and the effect of the Coulomb potentials of both donor and receptor nuclei on the outgoing proton. The multiplicity of the pre-equilibrium protons is lower than that of the neutrons and the proton spectra are harder than the neutron spectra as expected.

We have also incorporated the effect of the known diffuse momentum distributions of the nucleons in the nuclear ground state. This has been done in a somewhat *ad hoc* manner since it goes beyond the basic one-body nature of the model. The diffuseness used in our calculations is based on simulating the experimental ground state nucleon momentum distribution rather than by fitting pre-equilibrium particle emission spectra. It is therefore gratifying to find that the high-energy slopes of the calculated emission spectra are in good agreement with experiment. This extension is most important for low bombarding energy and for more asymmetric systems at a given bombarding energy, as it increases the multiplicity and hardens the spectra most in these circumstances. For higher bombarding energies and more symmetric systems energy dissipation at the early stages of the collision leads to hot nuclei with diffuse momentum distributions which dominate the contribution from the diffuse corrections to the ground state momentum distribution.

We have also investigated changes in the expected *pn* nucleon-nucleon bremsstrahlung due to both the aforementioned diffuse momentum distributions and quantum-mechanical effects on the elementary production mechanism. The latter had been treated classically in the earlier work.[2] Nakayama[3] and Schäfer *et al.*[4] have shown that quantum-mechanical effects are most important at higher nucleon-nucleon energies and for photons near the kinematic limit. The enhancements are typically less than a factor of two. When incorporated in our transport model they are most important for proton-induced reactions where it is possible to measure the photon emission near the kinematic limit, and for heavy-ion reactions at higher bombarding energies.

We have pursued a suggestion of Stuart Gazes that deceleration of the partners in the heavy ion reaction during the transit time of an exchanged nucleon may modify the emission probability more for jets originating from the heavier reaction partner than for those originating from the lighter partner. The results obtained are in the direction expected, but their effect on residue velocity is modest. Predictions of mean residue velocities exhibit the correct trend with mass asymmetry of the entrance channel but underestimate considerably the magnitude of the dependence. This underestimation is attributed to the fact that considerable momentum is carried away by composite

*Present address: Lawrence Livermore National Laboratory, L-397, Livermore, CA 94551.
†Lawrence Berkeley Laboratory, University of California, Berkeley, CA 94720.
[1] J. Randrup and R. Vandenbosch, Nucl. Phys. A **474**, 219 (1987).
[2] J. Randrup and R. Vandenbosch, Nucl. Phys. A **490**, 418 (1988).
[3] K. Nakayama,, Phys. Rev. C **39**, 1475 (1989).
[4] M. Schäfer, T.S. Biró, W. Cassing, U. Mosel, H. Nifenecker and J.A. Pinston, Z. Phys. A **339**, 391 (1991).

particles, particularly α particles. These composite particles may arise from massive transfer or breakup-fission mechanisms, as well as from coalescence mechanisms.

3.2 Rotational state populations in near-barrier fusion

J.D. Bierman, A.W. Charlop, D.J. Prindle, R. Vandenbosch and D. Ye

We have completed our study of the populations of the ground state rotational band of the 4n channel decay of ^{170}Yb produced using two entrance channels: ^{16}O + ^{154}Sm and ^{4}He + ^{166}Er. We have used three large Compton-suppressed intrinsic germanium detectors and coincidence techniques to measure the rotational state transitions. The populations were determined more accurately and more completely than a previous detector system[1] allowed. We were able to clean up the spectra enough so that three transitions, which before were unobservable, could be studied. At last report[2] we had obtained data at two oxygen bombarding energies, 68 and 65 MeV, and had also repeated the experiment using the ^{4}He + ^{166}Er reaction at 48 MeV. The latter reaction matches the higher energy oxygen system in excitation energy but is well above the barrier and is thus used to calibrate the parameters in the statistical model code PACE. We have now also obtained data for both systems at lower energies which match in excitation energy, 63 MeV for the oxygen system and 43 MeV for the alpha system. We were then able to confirm that the PACE parameters, which we determined from the higher alpha energy, were valid over our entire energy span. We have used the PACE code to convert our rotational state population results into values of the average angular momentum for the ^{16}O + ^{154}Sm system at all three near-barrier energies. Figure 3.2 shows our results as well as results from experiments using discrete gamma tagging techniques and evaporation residue tagging techniques.[3] Also shown is a coupled channels calculation using the code CCDEF. Our results compare well with the calculation and are slightly lower than the results from the previous multiplicity measurements. This suggests that the rotational state population method is a better probe of mean angular momentum values in the near-barrier energy regime than the multiplicity method because of the problems with converting multiplicities to mean angular momentum at near-barrier energies. We have also been able to determine a more detailed idea of what the actual spin distribution of the compound nucleus is. We found that the oxygen system at near-barrier energies had a much broader distribution in the compound nucleus than the sharp-cutoff like distribution which can be predicted for the asymmetric, well above barrier, ^{4}He + ^{166}Er system. While this experimental method is limited in the number of systems which are practical for study, we have found that if a proper calibration system is also studied that useful information about the spin distribution of compound nuclei resulting from near-barrier fusion can

[1] R. Vandenbosch, B.B. Back, S. Gil, A. Lazzarini, and A. Ray, Phys. Rev. C 28 1161 (1983).

[2] Nuclear Physics Laboratory Annual report, University of Washington, (1992) p. 22.

[3] S. Gil, A.W. Charlop, A. Garcia, D.D. Leach, S.J. Luke, S. Kailas, and R. Vandenbosch, Phys. Rev. C 43 701, (1991).

be extracted.

Fig 3.2 Mean l for ^{16}O + ^{154}Sm determined from conversion of rotational band populations using the evaporation model code PACE. Also shown are results from gamma multiplicities from discrete gamma (Ge) tags and evaporation residue (Deflector) tags. The full curve is from a coupled channels calculation.

3.3 Impact parameter dependence of pre-equilibrium light charged particle emission at 13.5 MeV/A

A.W. Charlop, C.E. Hyde-Wright, S. Kailas,* D.J. Prindle, and R. Vandenbosch

The analysis of our previously reported experiment[1] on light charged particles produced in ^{16}O bombardment of Tb, Ta, and Au has been completed. For the first two targets we have extracted LCP multiplicities for both evaporation residue (ER) and fission fragment (FF) tags. For the Au target we only have multiplicities for FF tags. From these results we have been able to deduce the dependence of pre-equilibrium multiplicities on impact parameter. The multiplicity of pre-equilibrium protons falls off with increasing impact parameter at a rate that is in good agreement with expectations from a nucleon exchange transport model.[2] The ratio of any complex particle (d, t,He) multiplicity to proton multiplicity however is found to increase with increasing impact parameter, as illustrated in Fig. 3.3-1. This dependence continues a trend first observed by Awes *et al.*[2] who compared pre-equilibrium multiplicities of peripheral collisions with central collisions. The present experiment has enabled us to examine the impact parameter dependence within the single "central" collision bin associated with nearly full momentum transfer.[2] Our observations are inconsistent with a simple coalescence model. They suggest a dynamical dependence on where the cluster formation occurs. A particular model based on an extension of the nucleon exchange transport model has been suggested in a previous report.[3]

Fig. 3.3-1. Ratio of pre-equilibrium complex particle multiplicity to proton multiplicity as a function of impact parameter.

*Present address: Nuclear Physics Division, BhaBha Atomic Research Center, Bombay, 400 085 India.

[1]Nuclear Physics Laboratory Annual Report, University of Washington (1990), p. 11.

[2]T.W. Awes *et al.*, Phys. Rev. C **25** (1982) 2361.

[3]Nuclear Physics Laboratory Annual Report, University of Washington (1991) p. 19.

3.4 Impact parameter tagged light charged particle emission at 25, 35 and 100 MeV/u

D. Bowman,* G. Cren,* M. Chartier,* R. Desouza,† J. Dinius,* A. Elmaani, D. Fox,† K. Gelbke,*W. Hsi,* C.E. Hyde-Wright, W. Jiang, W. Lynch,* T. Moore,† G. Peaslee,* D.J. Prindle, C. Schwarz,* M.-Y. Tsang,* R. Vandenbosch and C. Williams*

3.4.1 Introduction

The mechanism for producing pre-equilibrium complex fragments in heavy ion collisions is not well understood. This is particularly true for more central collisions where prompt and sequential decays of projectile-like particles do not contribute. At low bombarding energies, complex particles are primarily limited to particles with masses 2–4. At higher bombarding energies considerably larger complex particles are produced in appreciable yield.

An important aspect of any reaction process is the impact parameter dependence. Characterization of impact parameter on an event-by-event basis is difficult, particularly for central collisions where the energy deposition for a wide range of impact parameters is similar. We have shown that it is possible to use the angular momentum dependence of evaporation-fission competition to generate tags for the most and less central impact parameters within the general class of fusion-like impact parameters.[1] Using this technique we have shown that at 13.5 MeV/u the pre-equilibrium proton multiplicity falls off with increasing impact parameter while the ratio of pre-equilibrium complex particle to proton multiplicity increases with increasing impact parameter. In the present experiment we extend this study to higher bombarding energies and to coincidence detection of two or more light charged particles.

We used the MSU Miniball detector[2] to measure charged particle yields in 25 MeV/u ^{16}O and 35 MeV/u & 100 MeV/u ^{14}N on Au, Sm, Ta, and Tb targets. The forward Miniball ring was replaced with an array of Si (E,veto) telescopes to measure coincident evaporation residues. In each of the remaining rings, one Miniball element was replaced with an Ion Chamber-Si-CsI (IC) telescope. We used the ion chambers primarily to measure the coincident fission fragments.

From the information obtained in this experiment we will also be able to address some other issues. One of the current topics for these intermediate energy heavy-ion induced reactions is the probe of nuclear matter properties via particle interferometry, or small-angle particle-particle correlations. The major driving forces for these correlation measurements are the emission space-time extent of the particle pair used to construct these correlations.[3] We intend to use relative momentum and reduced velocity correlation functions, respectively, to characterize the mean emission lifetime for light charged particles (LCP) and intermediate mass fragments (IMF). Our evaporation residue and fission tags will allow us to compare results for the most and less central collisions as described above.

---

*National Superconducting Cyclotron Laboratory, Michigan State University, E. Lansing MI.
†Indiana University Cyclotron Facility, Indiana University, Bloomington IN.
[1]See section 3.3 of this report.
[2]R.T. Desouza *et al.,* Nucl. Inst. Meth. A **295**,109(1990).
[3]A. Elmaani *et al.,* Phys Rev **C43** R2474 (1991), and A. Elmaani *et al.,* Nucl. Inst. Meth. **A313** 401 (1992).

The study of the evolution of the emission timescales over a wide range of excitation energies (25–100 MeV/u) will be used to look for a change in the emission mechanism. We are particularly interested in the transition from fusion-like reactions, which occur on a timescale of hundreds of fm/c, to nuclear breakup, occurring on timescales of a few fm/c.

In addition to small angle particle-particle correlations, we will compare the yields of complex particles with the coincidence yields of their (approximate) constituents, *e.g.* d *vs.* pp, ^{4}He vs pt, dd, etc, as a further guide to the emission mechanism.

3.4.2 Particle identification and energy calibration

The signal from each miniball detector was fanned out into 4 signals: 1 timing signal and 3 analog signals. The analog signals were integrated over 3 separate gates, defined relative to the constant fraction discriminator output from the timing signal. The Fast gate has a 5 ns delay and 35 ns width. The Slow gate has a 200 ns delay and a 400 ns width. The Tail gate has a 2 μs delay and a 2 μs width.

Fig. 3.4.1. (a) Energy calibration points and the resulting quadratic fits for ^{1,2}H and ^{4}He measured in element 19 of the Miniball. (b) The corresponding energy spectra for ^{1,2}H, ^{4}He produced in the reaction of 25 MeV/u ^{16}O + ^{181}Ta and detected at $\theta_{lab} \approx 20°$.

We identified ^{1}H, ^{2}H, ^{3}H, ^{3}He, and ^{4}He by drawing 2-d gates in a plot of Tail *vs.* Slow, for each detector. This separation is possible because of the variable intensity and lifetime of the different light components in CsI as a function of ionization density.[4]

We have energy calibration runs with a ^{12}C beam on a polyethylene target. This produces two proton points from $p(^{12}\mathrm{C}, p)^{12}\mathrm{C}$ and $^{12}\mathrm{C}^*$(4.4 MeV). Also we have a mixed deuteron and alpha beam on a polyethylene target which produce 2 proton points from $p(\alpha, p)\alpha$ and $p(d, p)d$. Deuteron points and α calibration points were produced by passing a mixed deuteron and alpha beam through a variable degrader and then scattering on a gold target. We separately calibrate the Tail *vs.* energy and Slow *vs.* energy. We use a common quadratic fit for energy vs light output for H isotopes and a separate quadratic fit for He isotopes. Sample calibration data and energy spectra from one element of the Miniball are shown in Fig 3.4-1

3.4.3 Evaporation residue and fission fragment angular distributions

The forward array of Si telescopes was used to measure evaporation residues. The Miniball array of ten Ion-Chamber, Si, CsI telescopes from 19° to 150° was used to measure both evaporation residues and fission fragments. In the forward array, the first Si counter of each telescope stopped the residues, and the second counter vetoed quasi-elastic events. Residues were also identified by their correlated pulse height *vs.* time-of-flight distributions. Two of the Si telescopes were on a moveable arm, reaching from 3.5° to 15.5°. In the IC telescope, evaporation residues are identified by a ion-chamber signal in anticoincidence with the Si counter. In these same elements, the fission fragments were identified by coincidence between the Si and a large pulse height in the ion-chamber in anticoincidence with the CsI. Angular distributions of evaporation residues and fission fragments are shown in Fig. 3.4-2.

Fig. 3.4.2. Evaporation residue and fission fragment angular distributions.

[4]R.S. Storey, W. Jack and A. Ward. Proc. Phys. Soc. 75 (1958) 72.

3.4.4 Fission fragment angular correlations

In Figs. 3.4-3 and 3.4-4 we present preliminary result for the reaction 25 MeV/u ^{16}O + ^{181}Ta $\rightarrow$ $FF1+FF2$. $FF1$ is the trigger fission fragment measured in one of the ion chambers and $FF2$ is the complementary fragment observed in coincidence in one of the regular Miniball plastic-CsI elements. In Fig. 3.4-3, we show the relative azimuthal angular correlation. The 180° preference clearly indicate the fission fragment co-planarity. And in Fig. 3.4-4 we show the polar angle correlation of these same coincident fission fragment. We will be able to extract the mean momentum transfer to the fissioning nucleus from the fragment-fragment polar angle correlation.

Fig 3.4.3. Azimuthal angular correlation for fission fragments detected in coincident events between an Ion Chamber and a Miniball Phoswich detector.

Fig. 3.4.4. Surface plot of the polar angular distribution (θ_1, θ_2) of both fission fragments. The coincidence yield as a function θ_1 (FF1 detected as a trigger fragment in one of the ion chambers) and θ_2 (FF2 detected in one of the Phoswich detectors of the Miniball Array).

3.5 Fusion cross sections for three systems that produce ^{170}Hf at near and sub-barrier energies

D. Abriola,* J.D. Bierman, A.W. Charlop, Z. Drebi, A. Etchegoyen,* M. Etchegoyen,* S. Gil,* F. Hassenbale,* D.J. Prindle, D. Rodriguez,* J. Testoni* R. Vandenbosch and D. Ye

We have completed our analysis of the fusion cross sections for several systems (^{28}Si + ^{142}Ce, ^{32}S + ^{138}Ba, and ^{48}Ti + ^{122}Sn) that lead to the same compound nucleus, ^{170}Hf.[1] This work was done as part of a program to search for entrance channel effects in sub-barrier fusion.[2] These fusion cross sections were measured in a collaborative effort between the Nuclear Physics Laboratory and the Tandar Laboratory in Buenos Aires, Argentina.

The evaporation residue (ER) cross section was measured at the Tandar Laboratory using a delayed X-ray technique that they perfected.[3] This technique is able to determine the absolute ER cross section as well as the partial cross sections for the individual ER channels from the X-rays emitted by the radioactive decay of the ER's. The extracted cross sections are sensitive to the decay properties of the ER's and their daughters. Considerable effort has been devoted to estimating the decay properties for the nuclei produced in these reactions.

For the systems ^{32}S + ^{138}Ba and ^{48}Ti + ^{122}Sn, it was determined that there was a significant fission contribution to the total fusion cross section at energies just above the barrier. The fusion-fission cross sections for these two systems were measured with beams of ^{32}S and ^{48}Ti from our superconducting linac for lab energies in the range of 150–165 MeV and 192–220 MeV respectively. The forward fragment was detected at 55° in the center of mass with a ΔE–E telescope. The thickness of the ΔE detector was chosen such that the fission fragments were stopped in the detector but not the elastic particles. The complementary fission fragment was detected in a silicon strip detector centered at approximately 125° in the center of mass. The strip detector consisted of seven independent strips. The position of the backward detector was chosen so that all of the complementary fragments were within the active area of the strip detector.

The total fusion cross section, ER + fission, is shown in Fig. 3.5-1 for all three systems studied in the our search. The fission cross sections are shown as the shaded areas of the bottom two panels of the figure. For the ^{28}Si + ^{142}Ce system the fission cross section is estimated from PACE calculations that reproduce the ER yields for all three systems and the experimental fission yields measured here. The lines in Fig. 3.5-1 are coupled channels fits to the fusion cross sections using the code CCDEF.[4] The only adjustable parameters in the coupled channel fits was the depth of the nuclear potential and for the ^{32}S and ^{48}Ti systems the coupling strength of a 1-neutron transfer channel. For each system, the quadrupole and octupole deformations are obtained from tabulated B(E2) and B(E3) values respectively. The experimental fusion cross sections are well accounted for by our coupled channels calculations.

---

*Present address: TANDAR, Departamento de Fisica, CNEA, Buenos Aires, Argentina.

[1] Nuclear Physics Laboratory Annual Report, University of Washington (1991) p. 18.

[2] Nuclear Physics Laboratory Annual Report, University of Washington (1992) p. 21.

[3] D. DiGregorio, Phys. Rev. C 42 2108 (1990).

[4] J. Fernández-Niello, Comp. Phys. Comm. **54**, (1989) 409–412.

Fig. 3.5.1. Fusion excitation functions for ^{28}Si + ^{142}Ce (top), ^{32}S + ^{138}Ba (middle), and ^{48}Ti + ^{122}Sn (bottom). Solid curve is coupled channels fit to the experimental data using literature values for the deformation parameters. Dashed curve is the same coupled channels calculation with the couplings turned off.

3.6 A search for entrance channel effects in near and sub-barrier fusion

J.D. Bierman, A.W. Charlop, Z. Drebi, S. Gil,* D.J. Prindle, R. Vandenbosch and D. Ye

We have completed our efforts to search for a possible correlation between the mass asymmetry of the entrance channel and the broadening of the compound nuclear spin distribution at energies near and below the fusion barrier. We have measured the fusion cross section and γ-multiplicities for three systems (^{28}Si + ^{142}Ce, ^{32}S + ^{138}Ba, and ^{48}Ti + ^{122}Sn) that lead to the same compound nucleus (^{170}Hf) within the same excitation energy range. In a previous report[1] we discussed the γ-multiplicity measurements. The fusion cross sections have been determined for all three systems.[2]

The mean spin of the compound nucleus was determined using a formula based on the procedure of Halbert.[3] The statistical model code PACE was used to estimate the multiplicity of the statistical γ-rays and the average spin carried off by each evaporated particle and emitted statistical γ-ray, and the average spin of the fission branch. The parameters for the statistical model were determined by fitting the experimental relative yields of the evaporation and fission channels over the entire excitation energy range for all three systems simultaneously.

Fig. 3.6-1 shows the mean spins as a function of excitation energy for each of the three systems. The solid curves are the predictions of the coupled channels fits to the excitation functions.[2] The agreement between the model and the experimental results is excellent. There is no evidence for significant changes in the spin distribution of the compound nucleus formed by different entrance channels that are not accounted for in the coupled channels model using literature values of the deformation parameters.

*Present address: TANDAR, Departamento de Fisica, CNEA, Buenos Aires, Argentina.
[1] Nuclear Physics Laboratory Annual Report, University of Washington (1992) p. 21.
[2] Nuclear Physics Laboratory Annual Report, University of Washington (1993), sec. 3.5.
[3] M.L. Halbert *et al.*, Phys. Rev. C **40**, 2558 (1989).

Fig. 3.6.1. Mean spin of the compound nucleus as a function of excitation energy for ^{28}Si + ^{142}Ce (top), ^{32}S + ^{138}Ba (middle), and ^{48}Ti + ^{122}Sn (bottom). Solid curve is from a coupled channels fit to the experimental data using literature values for the deformation parameters. Dashed curve is the same coupled channels calculation with the couplings turned off.

3.7 Scattering of 87 Mev ^{6,7}Li on ^{12}C

W.J. Braithwaite,[*] J.G. Cramer, S.J. Luke,[†] B.T. McLain, D.J. Prindle, and D.P. Rosenzweig

We are in the last stages of our study of the scattering of ^{6,7}Li at 10–15 MeV/nucleon. We have measured elastic and inelastic cross sections for 87 MeV ^{6}Li + ^{12}C from 4° to 100° in the center of mass and for 87 MeV ^{7}Li + ^{12}C from 4° to 82°. We were able to resolve the first excited state of ^{7}Li at every angle.

Our data extend out far enough in angle to determine unique optical model potentials from the few discrete potentials that fit the inner angle data. Fig. 3.7-1 shows our ^{7}Li cross sections and optical model fits using a shallow, deep, and intermediate depth Woods-Saxon real potential. The shallow potential does not fit the large angle data very well and the deep potential provides the best overall fit. The situation is reversed in our ^{6}Li data where the shallow potential provides the best fit. Near-far decompositions of the cross sections show that the large angle data is dominated by the far side amplitude and exhibits the airy minima and maxima of a nuclear rainbow. The deep potential that fits the ^{7}Li data gives two or three airy minima while the shallow ^{6}Li potential gives only one. The transmission coefficients from our fits indicate that ^{7}Li is much more transparent than ^{6}Li at small impact parameter so the trajectories from the deeper potentials can more easily penetrate the nucleus and interfere with the larger impact parameter trajectories to produce the minima and maxima of the rainbow.

The inner angle data, which is sensitive mainly to the potential at or outside the nuclear surface, also exhibit differences between the ^{6}Li and ^{7}Li cases. As shown in figure 3.7-2, at larger radii both the shallow and deep potentials are greater in magnitude for ^{7}Li than for ^{6}Li. Also, the forward angle ^{6}Li fit is fairly good and does not improve noticeably with modifications of the potential, but the ^{7}Li fit at forward angles is not as good and can be improved considerably by a slight modification of the potential at about 10 fm. We plan to use folding model potential fits to see how these differences can be related to differences in the density distributions of ^{6}Li and ^{7}Li and compare the results to electron scattering data which show a large tail in the charge distribution of ^{6}Li comparaed to ^{7}Li.

Figure 3.7-1. Elastic scattering angular distribution for 87.0 MeV ^{7}Li + ^{12}C with optical model fits.

Figure 3.7-2. Woods-Saxon real potentials for 87.0 MeV ^{6}Li + ^{12}C and 87.0 MeV ^{7}Li + ^{12}C.

[*]Department of Physics and Astronomy, University of Arkansas at Little Rock, Little Rock, AK 72204.
[†]Lawrence Livermore National Laboratory, L-397, Livermore, CA 94551

3.8 The APEX experiment

T. A. Trainor and APEX collaboration*

The APEX double-arm beta spectrometer is nearing completion at the ATLAS facility at Argonne National Laboratory. It is intended to investigate the production mechanism for electron-positron pairs observed in connection with elastic nucleus-nucleus collisions for masses near uranium and beam energies near 6 MeV/A. The mechanism for producing these pairs, which appear to be decay products of neutral objects with discrete mass spectra, has remained elusive after ten years of study at GSI by three research groups.

APEX is designed to be a kinematically complete spectrometer with high efficiency. The heavy ion collision partners are detected in a nearly 4π position sensitive avalanche counter array which determines the kinematics of the collision and serves as a trigger condition. Electrons and positrons produced at the target spiral in a 300G field to symmetrically placed 36 cm long axial silicon arrays, each with 216 1 mm thick silicon diode detectors. Positrons annihilating on a silicon array produce back-to-back 511 keV gamma rays which are detected with high efficiency by NaI barrels surrounding the two silicon arrays. Each barrel is azimuthally segmented into 24 bars, and each bar is a position-sensitive gamma detector with resolution of about 2 cm. Thus, detection of a 511 keV pair in two nearly opposite bars serves to identify and locate a positron hit on the corresponding silicon array. This is the primary trigger condition for a positron event.

The hit position on the segmented silicon array combined with the particle energy and time of flight determined by the individual silicon detector serve to characterize completely the kinematics of the detected positron or electron. For each positron identified by a NaI barrel-silicon array combination an invariant mass spectrum is formed in combination with each coincident electron on either arm of the spectrometer. The GSI observations imply that a discrete mass spectrum superposed on a combinatoric background should result.

Questions to be addressed with APEX include the apparent motion of the hypothetical neutral "source" object, the relative kinematics of the pair (e.g., opening angle distribution), the variation of the mass spectrum with heavy ion collision system and kinematics, and the heavy-ion CM energy dependence of the pair production rate. The APEX-ATLAS combination represents a nearly 20-fold increase in pair detection rate and complete determination of invariant mass spectra.

One arm of the spectrometer has now been fully instrumented, and initial beam tests are underway. The accompanying articles describe the progress in further detail.

*Argonne National Laboratory, Argonne, IL 60439; Michigan State University, East Lansing, MI 48824; Princeton University, Princeton, NJ 08543; Yale University, New Haven, CT 06520; Florida State University, Tallahassee, FL 32306; and University of Rochester, Rochester, NY 14627.

3.9 APEX silicon array cooling system

G.C. Harper, D. Henderson,* E Roa,† and T.A. Trainor

The silicon detector arrays for APEX located in the arms of a symmetric two-arm beta spectrometer each contain 216 1 mm thick silicon diode detectors. These detectors are required to operate with resolutions of <5 keV in energy and <2 ns in time in order to best meet the physics goals of APEX.

The time resolution in particular is sensitive to the detector temperature, and temperatures below -60 C are required to optimize timing performance. Therefore, a cooling scheme was required to achieve these temperatures with reasonable cycle time and minimal additional mass in the region of the detectors.

We decided to use liquid nitrogen boiloff as the coolant. Liquid nitrogen in a double-walled stainless steel dewar is heated with a 400 W heater. The duty cycle of the heater is servo controlled to maintain a pressure of 5 psig above the liquid, independent of gas flow out of the dewar. The cold gas passes through a cryogenic needle valve and a 2.5 m coaxial transmission line to an end flange on the APEX apparatus. The gas passes through the end flange and into a 4 mm ID G-10 tube which serves as the axis for the 36 cm long G-10 assembly on which the silicon detectors are mounted. The detector array is surrounded by a kapton shroud sealed to the end flange. Gas emerging from the far end of the G-10 center tube returns inside the kapton shroud, passing over the detectors and cooling them.

After exiting the shroud the cold gas passes over the signal transmission strip lines from the detectors to reduce the heat load into the array. The gas then leaves the end flange and travels along a second 2.5 m coaxial exit line. The gas leaving this line is warmed to room temperature, passes through a Baratron pressure gauge and motorized Baratron valve assembly and finally into a Leybold DR-25B vacuum pump. The Baratron assembly regulates the pressure above the valve, and hence within the shroud region, to the selected operating pressure (150 or 250 Torr) independent of gas flow.

The shrouds are made of 8 micron or 12 micron aluminized kapton. A shroud is constructed on a series of jigs. First a 5 cm diam. tube is formed. The seam is a 1 mm overlap and is 20–30 microns thick. The seam and other joints are formed with Armstrong A-12 epoxy mixed in a cryogenic proportion of resin to hardener. The 40 cm long kapton tube is then epoxied on a second jig to an acrylic disk on one end and an acrylic flange with o-ring seal on the other. The jigs insure that the resulting shroud assemblies have very good geometric properties. The shrouds have burst strength exactly corresponding to the kapton sheet tensile strength. For the two thicknesses the burst pressures are 500 Torr and 750 Torr. The shrouds are operated at one third of the failure pressure. The aluminum layer is connected to the APEX vacuum vessel by small strips of aluminized kapton and silver epoxy to provide rf shielding for the detectors.

The coaxial lines, a double-walled region at the end flange, the double walls of the nitrogen dewar, and a cold valve box surrounding the cryogenic needle valve and solenoid-driven ASCO

*Physics Division, Argonne National Laboratory, Argonne, IL.
†Physics Department, Florida State University, Tallahassee, FL.

shutoff valves are all evacuated to provide cryogenic insulation. These regions are also wrapped with several layers of superinsulation to further reduce heat transfer. The major heat load on the gas occurs in the cold valve box, and is dependent on the quality of the insulating vacuum. The performance of the system has improved sharply as small leaks from the shroud region through the end flange assembly into the insulating vacuum have been eliminated.

With a nitrogen mass flow of 1 g/s (about 1/3 capacity) the detector array cools down to the desired temperature range (-80 C) in about 1/2 hour. There is provision to switch from boiloff nitrogen to room temperature dry nitrogen to complete a warmup cycle to room temperature in about the same time interval.

3.10 APEX monitor detector system

T. A. Trainor and S.P. Van Verst*

Incorporated in the APEX double-arm beta spectrometer is a system of monitor detectors. This system includes two high-resolution ion chambers, two CsI detectors, a parallel-plate avalanche counter (PPAC) and a Ge detector. This system is intended to monitor various beam and target properties

The ion chambers are mounted in the vertical plane through the beam and target at lab angles of +/− 11 degrees. They are housed in 15 cm diam. and 35 cm long stainless steel cylinders. The entrance windows are 220 $\mu g/cm^2$ aluminized mylar. The stopping medium is 25 cm of isobutane at 150 Torr. The entrance apertures are 1.5 mm by 25 mm slots oriented horizontally to minimize kinematic energy spread. The apertures are located at radii of 2 m.

The cathode and Frisch grid are separated by 50 mm and are parallel to and symmetrically placed about the aperture slot. The anode is 10 mm below the Frisch grid. The aluminized entrance window is placed at the cathode potential and tilted at 10 degrees from perpendicular to the particle tracks toward the anode to insure complete collection of created charge.

The large spacing and symmetry of the cathode and Frisch grid were found to be important for achieving sub 1% resolution because of the problem of completely collecting secondary charge deposited by finite range delta rays from the heavy ion track. The cathode and entrance window assemblies are designed to operate at up to 10 kV in order to provide high drift field intensities and reduce recombination in the track plasma.

During recent tests with 6 MeV/A uranium beam the ion chambers have operated with 0.5% resolution and negligible background. The dominant source of energy spread at this level is still kinematic broadening, due to the 2–3 mm beam spot on target. The remaining sources of spread in the detection process are estimated to make a 0.1–0.2% contribution to the overall resolution.

The motivation for achieving high energy resolution is the need to monitor carefully the effective beam energy on target and the state of the target when the beam intensity is limited by target sputtering and melting. The GSI experimental results indicate that the electron pair production depends sensitively on bombarding energy, but target instabilities made detailed studies of this aspect problematic.

The two ion chambers in the vertical plane combined with low resolution CsI detectors in the horizontal plane (also at 11 degrees) provide a monitor of the beam position on target through ratios of the counting rates. Precise information on the beam position is essential in order to make inferences on particle kinematics and angular correlations of electron pairs.

A single PPAC at 11 degrees serves as a beam time structure monitor. The PPAC is a 1.25 mm gap operating with 5 Torr of isobutane at 430 volts. The gap area is 20 mm diam. and the electrodes are 220 $\mu g/cm^2$ aluminized mylar with additional 2.5 μ mylar pressure windows. The rise time after one stage of Philips 776 preamplifier is 1.5 ns, with a S/N ratio greater then 25.

*University of Virginia, Department of Physics, Charlottesville, VA 22901.

The detector-rf timing resolution is estimated to be better than 100 ps, and the typical optimized ATLAS beam time spread is observed to be 500 ps FWHM at APEX.

3.11 Initial operating experience with APEX

T. A. Trainor and the APEX collaboration*

In February of this year APEX was operated with about 1 pnA of 6 MeV/A uranium beam from ATLAS and with representative parts of all major components in position. This marked the transition from the construction phase to the data acquisition phase for this spectrometer and also signaled a major accomplishment for the ATLAS uranium beam program.

Tests in late Summer and Fall, 1992 centered around beam optics, using intermediate mass test beams, and finally the first low-intensity uranium beams. The beam transport system was studied and optimized. Beam spot sizes and beam halos were measured. Background gamma-ray levels from the beam dump, especially into the NaI arrays, were also investigated. Monitor detector energy and time spectra were obtained with uranium beam, and the silicon array cooling system was successfully tested with representative silicon detectors in place on an array. Representative elements of the heavy ion counter array were operated with beams. Successful completion of these various diagnostics opened the way to commencement of the experimental program.

For the February, 1993 run APEX was operated single-ended, with one silicon array partially filled with detectors. The degree of instrumentation was limited essentially by the delivery schedule of commercial electronic components. In addition, the full heavy ion detector array and a complete NaI barrel were operational. This was also a first test of the back-to-back 511 keV gamma topology trigger in combination with the heavy ion array and silicon array.

Much of this initial run period was devoted to a step-by-step check of each detector system for cabling errors, gas leaks, software glitches and defective elements. The trigger system was analyzed in terms of expected vs observed accidental coincidence rates. Toward the end of the period all systems were run conjointly to examine the positron detection process. With the short time remaining this was not an attempt to observe details of positron spectra but rather a first investigation, with real hardware and beam, of background processes and efficiencies.

Given the complexity of the APEX spectrometer, the results achieved during this first run period are very satisfying. The various systems have performed as expected or better, and the stage is set for an aggressive data acquisition schedule in the future.

---

*Argonne National Laboratory, Argonne, IL 60439; Michigan State University, East Lansing, MI 48824; Princeton University, Princeton, NJ 08543; Yale University, New Haven, CT 06520; Florida State University, Tallahassee, FL 32306; and University of Rochester, Rochester, NY 14627.

4 Fundamental Symmetries

4.1 New equivalence principle results

E.G. Adelberger, M.G. Harris, B.R. Heckel and Y. Su

We have been taking data with the Eöt-Wash rotating pendulum instrument after the apparatus was completely rebuilt last year[1]. Our new 1-σ results for a Weak Equivalence Principle test, using two different composition dipoles, are

$$m_g/m_i(\mathrm{Be}) - m_g/m_i(\mathrm{Al}) = (-2.7 \pm 3.4) \times 10^{-12}$$

and

$$m_g/m_i(\mathrm{Be}) - m_g/m_i(\mathrm{Cu}) = (-1.6 \pm 4.2) \times 10^{-12}$$

Our measurements set stringent limits on composition-dependent macroscopic interactions. For example, the data set 2-σ constraints on the coupling constant of a vector interaction that couples to baryon number of $\alpha_5 = (0.5 \pm 3.0) \times 10^{-4}$ and $\alpha_5 = (1.2 \pm 2.8) \times 10^{-9}$ for Yukawa ranges of 1m and 10^7m respectively.

During the data taking and analysis, we found that it was necessary to investigate higher-order gravity gradient effects than we had considered previously. We now measure up to the third-order gravity field gradient at our pendulum location with special test bodies and have installed local masses to cancel the second and third-order gradients. The first-order gravity gradient was zeroed to better than 1% previously. However, in the past year we discovered that as rainwater penetrated the soil outside of the laboratory, the first-order local gravity gradient changed by as much as 1% of its value, so that our compensation of the first-order gravity gradient was worse than we had thought. To solve this problem, we modified our pendulum to make it less sensitive to the first-order gravity gradient. Data with this modified pendulum are still being taken.

In the near future we will outfit our pendulum with new test bodies made from perfect single-crystal silicon. This will provide a test of the so-called Weber solar-neutrino effect as well as additional Equivalence Principle measurement. We are now beginning design studies for a new-generation apparatus that should allow us to improve our sensitivity by another factor of 10.

[1] Nuclear Physics Laboratory Annual Report, University of Washington (1992), p. 26.

4.2 A test of the equivalence principle for ordinary matter falling toward dark matter

E.G. Adelberger, B.R. Heckel, G.L. Smith and Y. Su

The observed centripetal accelerations of stars in spiral galaxies are much greater than can be accounted for by the gravitational attraction of the visible matter in the galaxy. This has led to the conclusion that ~ 90 % of the mass in galaxies is non-luminous dark matter, apparently in some exotic form. This conclusion rests on the very reasonable assumption that gravity is the only long-range force acting between ordinary matter and dark matter. We have checked this assumption using the Eöt-Wash rotating torsion balance. The results have recently been published.[1]

We measured the differential acceleration of two different test-body pairs toward the center of our galaxy. By comparing this differential acceleration to the acceleration attributed to the Galactic dark matter, $a_{gal}^{DM} \approx 5 \times 10^{-9}$ cm/s^2, we find the Equivalence Principle parameters:

$$\eta^{DM}(\mathrm{Be, Cu}) = \Delta a(\mathrm{Be, Cu})/a_{gal}^{DM} = (0.0 \pm 1.2)10^{-3}$$

$$\eta^{DM}(\mathrm{Be, Al}) = \Delta a(\mathrm{Be, Al})/a_{gal}^{DM} = (+0.7 \pm 1.4)10^{-3}.$$

If we separate the acceleration of ordinary matter due to dark matter into its gravitational and non-gravitational components, $a_{gal}^{DM} = a_g^{DM} + a_{ng}^{DM}$, then our result probes the *differential* contribution of a_{ng}^{DM} for two materials (Be and Al, or Be and Cu). This can be related to the *total* non-gravitational acceleration of ordinary matter toward dark matter if we assume the non-gravitational interaction couples to a charge q_5, that is carried by both ordinary and dark matter. Then

$$\frac{a_{ng}^{DM}}{a_{gal}^{DM}} = \eta^{DM} \frac{\langle q_5/m \rangle}{\Delta(q_5/m)} ,$$

where $\langle q_5/m \rangle$ is the average of the two test body q_5-to-mass ratios and $\Delta(q_5/m)$ is their difference. (Note that this relation is independent of the q_5-to-mass ratio of dark matter.)

To proceed farther one must evaluate the q_5/m ratios for our two test-body pairs. In ref. 1 we consider various plausible tree-level values of $\langle q_5/m \rangle/\Delta(q_5/m)$ and show that except for a small region around $q_5 \propto m_f$, where m_f is the mass of a fermion constituent of our test bodies (*e.g.* e, p, or n), an EP-violating acceleration toward dark matter greater than 1/10 that of gravity is ruled out by our results. Even in this region where our sensitivity is poorest we find $a_{ng}^{DM}/a_{gal}^{DM} = (+0.11 \pm 0.39)$, which rejects by 2σ the hypothesis that a_{gal}^{DM} is predominantly non-gravitational.

In summary, we have provided laboratory evidence for the usual assumption that gravitation is the only significant long-range interaction between dark matter and ordinary matter.

[1] G. Smith *et al.*, Phys. Rev. Lett. **70**, 123 (1993).

4.3 Improvements to the rotating source experiment

E.G. Adelberger, T. Bast,[*] J.H. Gundlach, J. Haeuser,[†] M.G. Harris, B.R. Heckel, G.L. Smith, H.E. Swanson, H. Vija[‡]

Construction of the rotating-source torsion-balance has been completed and we are continuing to improve its performance. The leading cause of systematic effects is the gravitational coupling of the pendulum to the 3 tonne source mass located just 10 cm from the pendulum. The source contains 120 depleted Uranium blocks which were rolled and sheared to trapezoidal shapes. The tolerances on these pieces exceeded specifications making it difficult to achieve a homogeneous mass density. The blocks were removed and individually weighed, sized, and pressed flat. The source was then rebuilt using jigs to obtain a considerably more uniform mass distribution. The Q_{21} gradient was reduced by a factor of ten. The remaining Q_{21} and Q_{44} gradients were nearly canceled using compensator masses. The $L = 3$, $|M| = 1$ moments of the source and pendulum were measured with special test sources and test masses. The $L = 5$ gravitational coupling ($Q_{55}q_{55}$) was utilized to align the turntable center of rotation with the torsion fiber to better than 0.001". (The pendulum q_{55} moment arises from the q_{44} moment displaced from the center.)

A magnetic damper, consisting of a copper disk in a cylindrically symmetric magnetic field, was added to the top of the fiber. The swing and wobble modes of the pendulum were greatly attenuated with little effect on the damping of the torsional mode. Damping is required to run at high vacuum or when the isolation table is floating.

Compensator masses on the pendulum were originally designed to cancel the q_{20} moment of the entire pendulum, but not the q_{40} moment. We experimented with compensators which also canceled the q_{40} moment, as a tilt of the pendulum would produce a spurious signal (because q_{40} rotates into q_{41}). These compensators resulted in data with 3 times the statistical fluctuations of the original ones and were not used.

We developed a set of computer programs to investigate the gravitational torques felt by the pendulum. These run on a 33MHz 486 PC and were written in Turbo Pascal and Fortran. MULTI computes spherical multipole moments and gradients for both gravitational and Yukawa interactions. Its input is a descripter file which gives the mass configuration (pendulum or source) in terms of basis shapes that can be translated and rotated about the origin. Torques are computed on a multipole by multipole basis. MOVE calculates the effective multipole distribution resulting from a rotation or a displacement of the pendulum's origin relative to the source's. The descriptor file can generate an AUTOCAD drawing for visual checks of the object. These programs have proven useful in designing test bodies with specific multipole moments and for estimating torques that arise from imperfections in the pendulum or the source.

We have locked the angular velocity of our source mass to a crystal reference oscillator. This gives us the capability of rotating the source mass in resonance with the torsion pendulum.

[*]Johannes Gutenberg Universität, Mainz, Germany.
[†]Justus Liebig Universität, Giessen, Germany.

4.4 New constraints on composition-dependent interactions with ranges down to 1 cm

E.G. Adelberger, J.H. Gundlach, M.G. Harris, B.R. Heckel, G.L. Smith and H.E. Swanson

We have used our new rotating-source torsion-balance to set limits on fundamental, composition-dependent interactions with ranges, λ, down to 1 cm ($m_b = 20\ \mu$eV). The results are particularly sensitive to interactions coupled to the third component of isospin, I_3, but establish new limits for couplings to B and L as well. The apparatus is described in previous Annual Reports; an update on recent developments is given in this volume.

We have collected 24 days of data with a Pb/Cu detector dipole, during which we made two reversals of the dipole on the pendulum and one reversal of the Uranium source on the turntable. To limit the potentially largest systematic error, from gravitational quadrupole gradients, we measured the pendulum mass multipole moment q_{21} and the source field, Q_{21}, whenever the configurations were changed. This was done using a known Q_{21} arrangement of the source or special q_{21} testbodies respectively. We found no significant systematic effect at this multipole order. We tested for other potential systematic effects by exaggerating the assumed source (thermal, magnetic, electric, tilt). Linear extrapolations to the measured level at which these quantities varied at the rotation frequency yielded negligible systematic effects.

Combining all data, we obtain a preliminary value of 6.1 ± 8.0 nrad for the pendulum deflection amplitude properly correlated with the position of the Uranium source. The error is purely statistical, we infer that systematic errors are negligible at this scale. We do observe an ≈ 76 nrad signal that is independent of the dipole orientation on the pendulum tray. Data taken with the two dipole configurations, the two source orientations on the turntable, and with two orientations (180° apart) of the pendulum tray in the vacuum can, show that the common-mode signal depends on the relative orientations of the pendulum *tray* (not the dipole) and the Uranium source. This is consistent with a small deformation of the pendulum tray coupled to a residual gravity gradient of the source, and is being investigated further. The common-mode signal does not contribute substantially to our error as it is subtracted away by our various configuration flips; furthermore it does not point toward the center of the source.

Our data limit the strength of an interaction coupled to a charge $q_5 = (B - 2L)/\sqrt{5}$ to $\alpha_5 = (-7 \pm 9) \times 10^{-6}$ for $\lambda > 1$ m and $\alpha_5 = -0.7 \pm 0.9$ for $\lambda = 1$ cm.[1] The short-λ limits are particularly interesting because astrophysical constraints on exotic interactions are not restrictive in this region (the Turner window[2] on axions is $10^{-3} - 10^{-6}$ eV). Long-range $1/r^3$ QCD forces as suggested by Feinberg[3] are also significantly constrained by our results. In addition, we set constraints in a regime where experiments using the Earth as a source are relatively insensitive ($\lambda = 10 - 1000$ km).

We are currently running near the Brownian noise limit of the pendulum and plan to operate at a higher vacuum to reduce this noise.

[1] q_5 and α_5 are defined in Phys. Rev. D **42** (1990) 3267.
[2] M.S. Turner, Physics Reports **197** (1990) 67.
[3] G. Feinberg, Comments Nucl. Part. Phys. **19** (1989) 51.

4.5 Development of a spin-polarized torsion pendulum

E.G. Adelberger, M.G. Harris and B.R. Heckel

We are developing a new torsion pendulum to test for a spin-dependent potential of the form $V(r) = \alpha\hat{\sigma}\cdot\hat{r}[m/r + 1/r^2]e^{-mr}$, which would arise from the exchange of a low-mass particle (mass m) that was a CP-violating scalar/pseudoscalar mixture.[1] Such a potential could arise from a CP-violating axion exchange and would be intriguing because it violates CP symmetry on a macroscopic scale. To obtain a pendulum with a spin-dipole moment while minimizing the systematic errors that result from the accompanying magnetic dipole fields we have fabricated several magnetized tori. Each is composed of a semi-torus of SmCo joined to a similar semi-torus of AlNiCo which is magnetized *in situ* to produce a uniform internal magnetic field, and a minimum external 'leakage' field. Since the relative contributions to the field from spin- and orbital-angular momentum of the two materials are different, we obtain a net electron spin polarization. In an effort to further reduce the external magnetic fields, four such rings will be stacked in the pendulum with successive rings flipped about their spin axes in an A-B-B-A pattern. This operation preserves the spin direction but reverses the internal magnetic fields, thereby raising the multipolarity of the external fields.

With an internal field of 6000 Gauss we have achieved leakage fields of less than 1 Gauss, 2 cm from the 4 cm diameter ring. This corresponds to a magnetic dipole moment (to which our apparatus is sensitive) of 0.06 erg/Gauss. We plan to place the pendulum in our rotating-source apparatus.[2] The paramagnetic susceptibility of the three tonnes of uranium rotating in the Earth's magnetic field will cause a rotating field of at most 10^{-6} Gauss. With magnetic shielding this will result in deflections in the micro-radian region, larger than the signal-to-noise limitations of our detection system. This corresponds to measuring an interaction potential of some 10^{-22} eV/spin and would constitute the most sensitive test for an electron spin coupled force, comparing favorably with Wineland and Ramsey's result[3] of 2×10^{-19} eV/spin for nuclear spins.

Improvements will come from further reduction of the magnetic dipole moment, cancellation of the Earth's magnetic field, and actual corrections for the magnetic torque. This will be done by exaggerating in turn the external field and the dipole moment of the pendulum, which will permit us to measure accurately the magnetic properties of the detector and source.

[1] J.E. Moody and F. Wilczek, Phys. Rev. D **30**, 130 (1984).
[2] See J.H. Gundlach and G. Smith, *Improvement to the rotating source apparatus* in this Annual Report.
[3] D.J. Wineland and N.F. Ramsey, Phys. Rev. A **5**, 821 (1972).

4.6 Design of an apparatus to measure the PNC spin rotation of transmitted cold neutrons in a liquid helium target

E.G. Adelberger, B.R. Heckel, S.K. Lamoreaux,* D.M. Markoff, H.E. Swanson, and Z. Zhao

Detailed design work has continued and construction has begun on the apparatus to measure the parity non-conserving (PNC) spin-rotation of transversely polarized neutrons through a liquid helium target. The motivation for this experiment—to improve the experimental constraints on the isovector pion-exchange amplitude in the meson-exchange potential that describes the weak interaction between hadrons—and its overall design have been discussed in previous Annual Reports.[1]

Oxford Instruments, Inc. is designing to our specifications a cryostat that contains a central cold bore on which we will mount an insert containing the liquid helium targets, the target-gas transfer system, and the single central π-coil. This removable insert will separate the liquid helium target medium from the liquid helium cryogenic coolant, thus reducing the frequency of filling the target helium reservoir. The insert system is sufficiently flexible that it can be used in future spin-rotation experiments with other cold targets (such as para-hydrogen). The target chambers have been built; construction of the remaining parts of the insert awaits our review of the final cryostat drawings to assure compatibility.

Our design for the π-coil has changed since last year's Annual Report. The coil now consists of two solenoid coils placed side-by-side with their symmetry axes, the field axis, in the vertical direction so that the fields are in opposite directions in each coil. The return consists of three radially concentric toroidal coils that guide the field from one solenoid coil to its neighbor. The windings and sizes were determined using a computer calculation. Leakage fields and deviations from the field in the vertical direction should be reduced to less than one part in 10^{-3} while maintaining reasonably practical dimensions for construction. The input and output coils will use the previously developed three-solenoid design (a central solenoid coil with two half-width coils on both sides to serve as the return). Test coils measurements show that adding μ-metal at the ends of the coils to guide the return field gives a five-fold reduction in the leakage fields. This feature will be incorporated into the design.

The detector is a segmented ionization chamber run in integration mode to collect the 10^8 neutrons per second expected from the NIST reactor in Gaithersburg, Maryland. With a segmented detector that separates neutrons of different velocity groups, we take advantage of the fact that the neutron spin rotation due to magnetic fields is velocity dependent, while the desired PNC effect is independent of velocity. We will minimize the magnetic field in the target region by adjusting external field coils (previously described)[2] until each velocity group sees the same rotation.

The apparatus is designed to reduce false signals to less than 10^{-8}radians. To check for systematic effects, the collecting plates of the detector will be divided into four sections so that neutron flux and apparent spin rotation can be studied as a function of detector region. By comparing results from the different detector regions for the front and back target positions, we hope to identify

*Department of Physics, University of Washington, Seattle, WA 98195.

[1]Nuclear Physics Laboratory Annual Report, University of Washington (1987) p. 27; (1989) p. 18 and (1990) p. 33.

[2]Nuclear Physics Laboratory Annual Report, University of Washington (1992) p. 25.

any target-dependent signals that mimic the PNC effect.

4.7 Isovector radiative decays of the 16.6 and 16.9 MeV doublet in ^{8}Be

E.G. Adelberger, L. DeBraeckeleer, J.H. Gundlach, M.S. Kaplan,* D.M. Markoff, A.M. Nathan,* W.R. Schief, K.A. Snover and D.W. Storm

It is presumed that in the limit of good isospin both the conservation of the vector current and the absence of second class currents are exact symmetries[1,2], but they are broken by quark mass differences. Thus there is much interest in testing these symmetries with precision enough to probe the level of expected isospin violating effects[3]. Our goal is to make a test of CVC in mass 8 nuclei with improved precision.

To make an improved test in mass 8, the width of the analog isovector M1 transition and the E2/M1 ratio must be remeasured with better accuracy. These quantities are determined from measurements of the angular distributions of the photons emitted in the reaction ^{4}He(α,γ) at the energies of the 16.6 and 16.9 MeV states and from the measurement of the excitation function across both resonances.

Previous measurements[4,5] of the angular distributions were done with a long gas cell in order to shield the detector from the background generated by the cell windows. However, several disadvantages are incurred by this approach. Among them is the fact that the γ-ray collimators must be different for each angle, thus making the calculation of the correct angle-dependent solid angle a possible source of error.

We have taken a different approach, using a short gas cell. To eliminate the background from the windows, we measure photon spectra with the cell filled alternately with helium and hydrogen, to match the dE/dx of the He gas, and subtract the hydrogen spectra from the helium. The problems of the long cell are thus avoided. One systematic correction we must make to the data is for incomplete beam bunching by our LINAC. Without an analyzing magnet, we monitored the beam energy at frequent BIC intervals by measuring the energy of α's elastically scattered from a thin gold foil.

We have measured the angular distributions at both resonances and the excitation function across both resonances. Preliminary analysis shows $a_2 = 0.75 \pm .04$ on the upper (16.9 MeV) resonance, and $a_2 = 0.25 \pm .06$ on the lower (16.6 MeV) resonance, in disagreement with previous measurements[4,5]. Since the predominant decay resonance is isovector M1, and pure M1 decay would result in $a_2 = \pm 0.5$, our angular distribution results indicate that the dominant E2 component has opposite sign on the two resonances and hence is predominantly isoscalar. Final analysis of the data, including the excitation curve, is presently under way.

---

*Department of Radiology, University of Washington Medical Center, Seattle, WA 98195.

†Physics Department, University of Illinois at Urbana-Champaign, Urbana, Illinois 61820.

[1] E. Commins and P. Bucksbaum, Weak interactions of Leptons and Quarks (Cambridge University Press, Cambridge, England, 1983).

[2] E. Henley and L. Wolfenstein, Phys. Lett. 36B, 28 (1976).

[3] A Long Range Plan for Nuclear Science, a report by the DOE-NSF Nuclear Science Advisory Committee, 1983, pp. 25–27.

[4] A.M. Nathan *et al*, Phys. Rev. Lett. 35, 1137 (1975).

[5] T.J. Bowles and G.T. Garvey, Phys. Rev. C 18, 1447 (1978).

4.8 Improved limits on scalar currents in weak interactions

E.G. Adelberger

Although there is much evidence for the $V-A$ form of the charged weak current, the constraints on scalar couplings that would arise if a massive charged scalar boson were exchanged instead of the $W^{\pm}$ are surprisingly poor.[1] This occurs because the scalar couplings must be inferred from observables (particularly the e-ν correlation) in which they enter quadratically, unless one makes restrictive assumptions about their parity or time-reversal properties. Furthermore, the scalar exchange amplitudes participate only in Fermi decays, and there have been no measurements of the e-ν correlation in a pure Fermi transition.

The e-ν correlation is usually measured by the lepton-recoil effect on the energy of the daughter nucleus. This is a formidable task because of the low recoil energy (of order 100's of eV) and possible distortion of the recoil-energy distribution by energy loss and chemical effects. It has not been appreciated that β-delayed proton emitters provide a powerful tool for determining the e-ν correlation in pure Fermi decays. I have extracted new limits[2] on scalar weak coupling from recent data of Schardt and Riisager[3] on the shapes of the β-delayed proton peaks corresponding to the superallowed decays of ^{32}Ar and ^{33}Ar. Because of the CM-to-lab transformation, the β-delayed protons are given an energy *spread* that exceeds the energy of the recoiling nucleus by a factor of roughly 50. Thus the difficult problem of measuring the $\approx$600 eV energy of a recoiling ^{32}Cl ion has been transferred into the much easier problem of measuring the $\approx$30 keV spread in energies of a 3 MeV proton group. Because their proton decays are isospin-forbidden, the natural widths of the superallowed proton groups are negligible ($\approx$100 eV). On the other hand, the proton decay occurs very rapidly compared to the slowing-down time of the recoil ions, so that the proton energy spread is not affected by energy loss of the recoil ions.

Schardt and Riisager's data yields a value

$$a_F = 1.016 \pm 0.036 \qquad (1)$$

for the e-ν correlation coefficient in a Fermi transition, where the error is 2σ. (In ref. 2, I show that the Gamow-Teller component of the ^{33}Ar superallowed decay has no significant effect on the extracted value of a_F.) This establishes a 2σ limit on the scalar exchange amplitudes of

$$\frac{|C_S|^2 + |C_S'|^2}{|C_V|^2 + |C_V'|^2} \leq 1.0 \times 10^{-2} \qquad (2)$$

where I employ the conventional notation[4] for the scalar and vector amplitudes. This result represents a substantial improvement over previous constraints on both time-reversal even (ref. 1) and time-reversal odd[5] scalar weak amplitudes. Details may be found in ref. 2.

Together with D. Schardt, J. Sromicki and K. Riisager, I am planning a new experiment at the ISOLDE on-line isotope separator at CERN to obtain substantially improved data on the e-ν correlation in the superallowed decays of ^{32}Ar and ^{33}Ar.

[1]A.I. Boothroyd *et al.*, Phys. Rev. C **29**, 603 (1984).
[2]E.G. Adelberger, submitted to Phys. Rev. Lett., January 1993.
[3]D. Schardt and K. Riisager, Zeitschrift für Physik A, to be published.
[4]J.D. Jackson, S.M. Treiman and H.W. Wyld Jr., Nucl. Phys. **4**, 206 (1957).
[5]M.B. Schneider *et al.*, Phys. Rev. Lett. **51**, 1239 (1983).

5 Accelerator Mass Spectrometry

5.1 Scientific program

T.A. Brown, G.W. Farwell and P.M. Grootes

5.1.1 AMS ^{14}C dating of pollen from lake sediments and peat deposits

Most of our efforts over the last year have been devoted to completing the development and validation of our method for the extraction of pollen concentrates from lake sediment and peat samples. Results from a preliminary set of measurements have been published.[1] Since those measurements, we have made some changes to the extraction method and have extracted and dated pollen concentrates from 8 sediment cores obtained from lakes and bogs in northern California, the Puget Lowlands, the east side of the Cascade Range and southern Vancouver Island. The samples taken from these cores were associated with the Mazama ash layer which fell following the Mount Mazama eruption that formed Crater Lake, Oregon, about 6700 years ago. These measurements were designed to demonstrate that the extraction and AMS dating of pollen from sediment cores provides more consistent and reliable radiocarbon dates than the traditional sample preparation techniques of β-counting radiocarbon dating.

The modifications we have made to the pollen extraction procedure have improved the rejection of nonpollen contaminants while minimizing damage to the pollen grains. The major modification was the introduction of a sulphuric acid step specifically designed to remove cellulose fragments. This step is based on procedures previously developed to determine quantitatively the component monosaccharides of a broad range of natural samples.[2]

The samples for pollen extraction and radiocarbon dating were taken from immediately above and below the Mazama ash layer in each of the 8 sediment cores. Two pollen concentrate fractions were prepared from each core sample following the procedures we have developed. In addition, a subsample from each sample was prepared for AMS radiocarbon dating following the normal β-counting method of treatment with 1.0 N HCl. In total, the radiocarbon ages of 48 samples were determined; typical uncertainties for these measurements were 50–70 years (corresponding to 0.6–0.9% measurement uncertainties). In general, the dates obtained are within the wide range of previous dates for the Mazama ash layer. While a detailed discussion of our dates is beyond the scope of this summary, it is clear that the dates we have obtained show several features that have not been resolvable in previous dating of the ash layer. One obvious feature of the data set is a significant offset between the dates obtained for the above and below the ash layer samples; preliminary modelling of deposition processes indicates that bioturbation effects could account for this offset. We are currently analyzing these dates and have presented preliminary results at the 23rd Arctic Workshop, held April 2–4, in Columbus, Ohio.[3]

We intend to continue our work on the extraction and dating of pollen from lake sediment and peat samples of paleoclimatic interest. In particular, we intend to expand our area of study to the

[1] T.A. Brown, G.W. Farwell, P.M. Grootes and F.H. Schmidt, Radiocarbon **34**, 550 (1992).
[2] G.L. Cowie and J.I. Hedges, Analytical Chemistry **56**, 497 (1984).
[3] T.A. Brown, G.W. Farwell, and P.M. Grootes (abstract), 23rd Arctic Workshop, April 2–4, 1993, Byrd Polar Research Center, Columbus, Ohio.

Arctic regions, concentrating initially on the migrations of spruce and alder across Alaska in the early to mid-Holocene. This research is funded in part by a NSF grant to P.M. Grootes and G.W. Farwell under the Paleoclimate of Arctic Lakes and Estuaries Initiative of the ARCSS Program (Grant No. ATM 91-23963).

5.1.2 Atmospheric methane

We have continued our time-series measurements of the ^{14}C concentration of atmospheric methane in collaboration with Paul Quay, School of Oceanography, University of Washington. This research is supported in part by a NASA grant to Dr. Quay (Grant No. NAGW-844).

Preliminary analysis of our most recent measurements on samples from the clean air site at Cheeka Peak on the coast of the Olympic Peninsula, Washington, gives an average value for 1991 of about 125 percent Modern Carbon (pMC) and shows some evidence of a small increase in the ^{14}C concentration of atmospheric methane during the period from 1989 to 1992 (it is not clear at this stage if this increase is statistically significant given the scatter of the measurements over that period). Significantly lower pMC values have been reported previously for atmospheric methane in the southern hemisphere[4] and there has been a suggestion of a significant increase (on the order of 1 pMC/year) in the ^{14}C concentration of atmospheric methane in the southern hemisphere since 1990. Our time-series data coupled with the results from the southern hemisphere and new data from other groups in the northern hemisphere should add significantly to our understanding of the sources, sinks and atmospheric transport of methane.

As a part of this project we measured the ^{14}C concentration of an interlaboratory comparison methane sample; this sample is also being measured by three other groups who are actively involved in developing time-series records of the ^{14}C concentration of atmospheric methane. We obtained a value of 121.1 $\pm$ 0.8 pMC for the intercomparison sample. Unfortunately, the other three laboratories have not reported their results at this time.

5.2 Technological program

5.2.1 Performance of the HE beam transport system and the wide-aperture detector

The wide-aperture ^{14}C detector and associated modifications to the high energy (HE) beam transport system (implemented in late 1991[5]) have significantly reduced the sensitivity of our measurement system to fluctuations in the accelerator terminal voltage. Modified tuning of the HE beam transport system to take full advantage of the large acceptance window of the detector, together with improved uniformity in the magnetic field of the "Wien filter" velocity selector (achieved by the addition of steel shims outside the beam tube), has resulted in a wide and flat terminal voltage transmission plateau at the detector (typically 24–28 kV). The reduced sensitivity to terminal voltage fluctuations that results at both the detector position and the image position of the 90° analyzing magnet has significantly decreased the difficulties encountered in tuning the beam through the HE transport system to the detector and has improved the sample wheel-to-sample wheel reproducibility of measurements obtained with our AMS system.

[4] D.C. Lowe, C.A.M. Brenninkmeuer, S.C. Tyler and E.J. Dlugkencky, J. Geophys. Research **96**, 455 (1991).
[5] Nuclear Physics Laboratory Annual Report, University of Washington (1992) p. 34.

During the year we found that the slits and slit box at the object position of the 90° analyzing magnet were all out of alignment; the most significant misalignment was that the top slit was 0.15 inches below the center line when its position indicator showed it as being centered. This particular misalignment seems to have been the cause of considerable difficulties in trying to tune the ion beam through the HE transport system with a minimum of vertical steering during previous AMS runs. We have now aligned all of the elements in the object slit box properly.

Reorganization of the detector electronics to optimize the signal-to-noise ratios of our ΔE and E detectors and eliminate parasitic ground-loop noise has resulted in a significant improvement in the performance of our detector telescope. Under current operating conditions, the FWHM of the ΔE peak is 0.28 MeV (4% of the 7 MeV deposited in the ΔE detector), the FWHM of the E peak is 0.40 MeV (1.5% of the 28 MeV deposited in the E detector), and the FWHM of the E_{total} peak is 0.28 MeV (0.8% of the 35 MeV total energy of the $^{14}C^{4+}$ ions). The improved detector resolution increases our ability to discriminate against scattered non-$^{14}C^{4+}$ ions which may, by chance, produce ΔE and E signals close to those detected from $^{14}C^{4+}$ ions.

The variations in the energy deposited in the ΔE detector (0.28 MeV FWHM) can be largely attributed to the outward bulge of the mylar window of the detector under the typical counting-gas pressure of 200 Torr. The variations in the energy lost by the ions in the ΔE detector gas then appear as a contribution to the width of the E peak (0.28 MeV out of the total width of 0.40 MeV; the other 0.28 MeV component of the E peak width is probably due to the resolution of the E detector). Hence, the 0.28 MeV FWHM value for the E_{total} (the sum of ΔE and E) peak shows that the ΔE and E values are correlated (extra energy detected in the ΔE detector due to increased path length in the gas results in decreased energy being detected in the E detector for that ion) and that the variations in path length in the ΔE detector do not contribute significantly to the observed peak width of our E_{total} measurements.

5.2.2 Alteration in the tuning of the LE beam transport system

During the last year we tested and implemented two changes to the low energy (LE) beam transport system. Firstly, we removed the 5/32 inch diameter LE aperture that we had previously inserted at the image position of the inflection magnet and now use the ion-source einzel lens to maximize the C^- beam current at the LE Faraday cup. This change has increased the C^- ion transmission from the source to the LE Faraday cup by about 35% and altered the beam profile so that transmission is insensitive to small differences in beam trajectory between samples. Secondly, we operated our measurement system without inserting the grid lens at the entrance to the accelerator beam tubes. This has eliminated the 10% beam loss on the grid of the entrance lens and also reduced the sensitivity of ion beam transmission to small differences in beam trajectory. Together these changes have increased the beam current transmitted from the ion source through the tandem by about 50% and reduced the sensitivity of our system to potential differences between samples.

5.2.3 Current performance of the measurement system

The current performance of our ^{14}C AMS measurement system can be summarized as follows:

1. The ion source is operated at low to medium output levels (20–30 uA $^{12}C^-$) to ensure continuous long term operation; $^{14}C^{4+}$ count rates for approximately modern samples are typically

45–60 cps; our typical measurement uncertainty for a routine determination of the $^{14}C/^{13}C$ ratio of an approximately modern sample is $\pm 0.7\%$,

2. The $^{14}C/^{13}C$ ratios obtained for our Chinese Sucrose laboratory standard over the course of a sample wheel (about 20 measurements of the standard for each wheel) have a 1σ scatter of about 0.69% while the 1σ counting statistics errors for these measurements average about 0.64%; this implies that only 0.26% of the 1σ scatter observed in our $^{14}C/^{13}C$ determinations cannot be accounted for by counting statistics,

3. In recent measurements we obtained percent Modern Carbon (pMC) values of 22.73 ± 0.15 and 151.1 ± 0.8 for the IAEA intercomparison materials C-5 and C-6, respectively; these values are in acceptable agreement with the consensus values for these samples of 23.05 ± 0.02 and 150.61 ± 0.11, respectively,[6]

4. In recent measurements we obtained a ^{14}C age of 6120 ± 50 BP for the approximately one half-life old sample QL11658, which agrees with the 6120 ± 30 BP ^{14}C age obtained previously by high precision β-counting (Minze Stuiver, pers. com.).

5. As part of our pollen study we prepared and measured sputter source target pairs from 27 graphitized CO_2 subsamples of our pollen extracts; within statistics, we found no evidence of significant differences between the measured $^{14}C/^{13}C$ ratios of target pairs; ie., we found no evidence of significant target-dependent scatter in the differences between the $^{14}C/^{13}C$ ratios for target pairs.

[6] K. Rozanski *et al.* Radiocarbon **34**, 506 (1992).

6 Medium Energy

6.1 Inclusive pion photoproduction on several nuclei

K.G. Fissum,* M. Frodyma,† K. Garrow,* I. Halpern, H. Kaplan,* D.P. Rosenzweig, D.W. Storm, and J. Vogt*

We measured photoproduction of positive pions on nuclei in order to obtain information about the mean free path of pions in nuclear material. The photons illuminate the nucleus uniformly. Then if we assume the photoproduction proceeds as it would on free (but moving) nucleons, limited only by Pauli blocking, we can calculate spectra. In fact, guided by our scattering studies, we include the possibility that the Delta-like object, produced when a proton absorbs a photon, may de-excite by interacting with a neighboring nucleon rather than by emitting a pion. The pions emerging from the photon interaction site are attenuated, causing a reduction in the magnitude of the cross section. By comparing measured with calculated cross sections, one hopes to determine the effective cross section for attenuation of pions which can be combined with nuclear density to obtain a mean free path. Since the pions have a broad range of energies (due to the nucleon Fermi motion), these quantities can be obtained as a function of energy. The angular distributions calculated for the photoproduced pions are obtained from the angular distributions for production on free nucleons after accounting for Fermi motion and Pauli blocking. The semi-classical calculation that we have developed for pion scattering is well suited for photoproduction as well.

Results of preliminary data analysis were reported last year.[1] We have now completed the data analysis and have obtained spectra of π^+ produced at four angles by tagged photons in the energy range 179 to 217 MeV. The targets were C, Ca, Sn, and Pb, as well as CH_2 used for calibration. The detectors were plastic scintillator telescopes. Positive pions were identified by detecting the muon from the pion decay.

Since we are using the free photoproduction cross section in our calculations and we have measured this cross section, we can compare our results on complex nuclei with the results on hydrogen. We do this by normalizing our measured cross sections by a single common factor, obtained by matching our measured cross sections for photoproduction on hydrogen to the Blomqvist-Laget[2] formulation. Then we use that parameterization in the calculation, where cross sections are needed over a range of photon energies, because of the nucleon Fermi motion.

It should be possible to determine the absolute cross section without normalizing to hydrogen measurement, using the measured photon flux and corrections described in last year's annual report.[1] (Preliminary results presented last year had an error in the detection efficiency, resulting from an incorrect value for the time interval after the pion pulse during which the muon can not be detected.) After applying these corrections we find that our measured differential cross sections for photoproduction on hydrogen are about 1/2 those predicted by the parameterization of Blomqvist and Laget. The disagreement between the Blomqvist-Laget formulation and various other measurements is around the 10 to 20% level, rather than a factor of two. Thus, it seems that there is

*University of Saskatchewan, Saskatoon, S7N 0W0, Canada.
†Now at: Stanford Linear Accelerator Center, Stanford, CA 94309.
[1] Fissum *et al.,* Nuclear Physics Laboratory Annual Report, University of Washington, p. 39 (1992).
[2] I. Blomqvist and J.M. Laget, Nucl. Phys. **A280**, 405 (1977).

a factor of about 2 error in our absolute normalization.

In Fig. 6.1-1 we present doubly differential cross sections averaged over incident photon energies of 211 to 217 MeV, compared with calculations using the free pion-nucleon cross section (obtained from the phase shifts of Rowe *et al.*[3]) for the pion attenuation calculation. The detector threshold at 15 Mev is responsible for the lack of agreement at the highest excitation energies. Otherwise the agreement is reasonably good, with the calculation lower than the data at high excitation for light targets, but at low excitation for heavy targets. Integrating over energy (with a cut off at the detector threshold) and over angle gives the results presented in Fig. 6.1-2. From this figure we see that the calculation reproduces both the offset in cross section between hydrogen and complex nuclei as well as the decreasing cross section (per proton) with increasing atomic mass. The former is attributed to the combination of Pauli blocking and the process that, in the scattering calculation, corresponds to pion absorption. The branching absorption parameter,[4] a, is taken to be 1., which gives credible results for scattering also.

Fig. 6.1-1. Examples of double differential cross sections for photoproduction of π^+ on two nuclei at two angles. These results are for a 6 MeV band of photon energies centered at 214 MeV. The curves are for the calculation described in the text. Statistical uncertainties are shown.

Fig. 6.1-2. Integrated photoproduction cross section *per proton* for pions of energy above 15 Mev for four targets. The curve connects calculated values, using the calculation described in the text. The decrease of this quantity with increasing atomic mass is assumed to result primarily from pion attenuation in the nuclear material. The additional shift downwards compared to the result for hydrogen is assumed to result from Pauli blocking or from de-excitation of the "Delta" by interactions taking place before pion emission.

[3] G. Rowe, M. Salomon and R.H. Landau, Phys. Rev. C **18** 584 (1978).
[4] D.P. Rosenzweig *et al.* Phys. Rev. C **46** 1968 (1992).

6.2 Fermi gas calculations of inclusive pion photoproduction

D.W. Storm

A quantum mechanical calculation of pion photoproduction in the impulse approximation for a Fermi gas target has been described in the literature.[1] This calculation uses the Blomqvist-Laget amplitude[2] in a factorized approximation with a non-interacting, zero-temperature Fermi gas describing the initial nuclear state and a final nuclear state differing from the initial one by a single nucleon knock-out. Although it has been pointed out[3] that the assumption of an abruptly vanishing momentum distribution will give the wrong threshold behavior of the cross section, such a calculation provides a useful tool for understanding the effects of Fermi motion and Pauli blocking on the reaction we have studied experimentally at the Saskatchewan Accelerator Laboratory.[4]

For photons in or above the energy range of our measurement, the authors of Ref. 1 report, for example, a substantial reduction in the photoproduction cross section per proton when comparing either Ca or Pb with hydrogen. Furthermore, as one would expect for a reduction due to Pauli blocking, it is most significant at forward angles. Consequently, we wrote a computer code which reproduces the calculations of Ref. 1. (Incidentally, some of the equations of Ref. 1. have some typographic errors; following the discussion of the paper the typographic errors in the derivation become apparent. When the correct equations are used we duplicate the graphs of Ref. 1.) We obtain the Blomqvist-Laget cross section from a program by J. Koch and others.[5] Different Fermi momenta are entered for the proton and neutron distributions. We find that in the limit of very small Fermi momentum the cross sections per proton that we obtain are identical to those obtained directly using the Blomqvist-Laget amplitudes. These checks lend credibility to our calculation.

As expected, Fermi motion spreads the spectra out over nearly the entire available energy range, except at the forward angles where energy and momentum conservation require the pions have relatively large energy. At the same time Pauli blocking reduces the cross section for the high energy pions. In general, Pauli blocking especially supresses the forward cross section, but, at the low momentum transfers available in this reaction, it reduces the cross section per proton from that for a free proton at all angles. For the heavy nuclei, with N>Z, the Fermi momentum for the neutrons is larger than for the protons, so that the Pauli blocking of positive pion photoproduction is magnified. Calculations for hydrogen, calcium, and lead are illustrated in the figures. These calculations do not include any effects of nucleon optical potentials or of pion distortion. Only the modification of the free interaction by Fermi motion and by Pauli blocking are included.

---

[1] W.M. MacDonald, E.T. Dressler and J.S. O'Connell, Phys Rev. C **19**, 455 (1979).

[2] I. Blomqvist and J.M. Laget, Nucl. Phys. A **280**, 405 (1977).

[3] M. Lax and H.Feshbach, Phys Rev **81**, 189 (1951).

[4] see previous article.

[5] Obtained from A. Nathan.

Fig. 6.2-1. Double differential cross sections *per proton* for photoproduction of π^+ on a nucleus with Fermi momentum of 250 for both protons and neutrons (Ca) and for a nucleus with Fermi momentum of 265 for protons and 306 for neutrons (Pb). The photon energy is 214 MeV.

Fig. 6.2-2. Photoproduction angular distributions *per proton* for the cases listed in the previous figure as well as for hydrogen. The supression of the cross section due to Pauli blocking is evident.

6.3 Nucleon form factors at high momentum transfer

J. Alster,* L. Andivahis,† R.G. Arnold,† P.E. Bosted,† C.C. Chang,‡ F.S. Dietrich,§ W. Dodge,¶ R. Gearhart,|| J. Gomez,** K. Griffioen,†† R. Hicks,‡‡ C.E. Hyde-Wright, C. Keppel,† S. Kuhn,† J. Lichtenstadt,* A. Lung,† R. Miskimen,‡‡ G.A. Peterson,‡‡ G.G. Petratos,* S.E. Rock,† S. Rokni,† W.K. Sakumoto,* M. Spengos,† L. Stuart,** K. Swartz, Z. Szalata† and L.H. Tao†

In SLAC experiment NE-18 we measured elastic electron scattering on the proton and inelastic scattering on the deuteron. Electron beams of 1.5 to 9.8 GeV and 0.5 to 10 μA were scattered from a 15 cm liquid hydrogen cell. Electrons were detected in the 8 GeV and 1.6 GeV spectrometers. Using a Rosenbluth separation, we separated the Sachs form factors G_E and G_M from the proton data[1] for $Q^2 \leq 8.8$ GeV^2. The charge form factor is consistent with the dipole fit

$$G_{E,p}(Q^2) \approx G_D = 1/\left[1 + Q^2/(0.71\,\mathrm{GeV}^2)\right].$$

However, the magnetic form factor $G_{M,p}(Q^2)$ shows a significant deviation from the dipole fit, falling 10% (three standard deviations) below $\mu_p G_D(Q^2)$ at $Q^2 = 8.8$ GeV^2.

We extracted the neutron form factors from the quasi-free D(e, e') data[2] for $Q^2 \leq 4.0$ GeV^2. Using the impulse approximation we subtracted the quasi-free proton and quasi-free $N(e, e')N\pi$ continuum to obtain the quasi-free $n(e, e')n$ response. The measured $p(e, e')N\pi$ continuum was modeled as a resonant (Δ) and non-resonant piece. The non-resonant $n(e, e')N\pi$ continuum was assumed to have the same shape as the proton cross section, but the strength was treated as a free parameter. The neutron magnetic form factor is consistent with the dipole fit:

$$G_{M,n}(Q^2) \approx \mu_n G_D(Q^2).$$

However, the neutron electric form factor is consistent with zero and, in particular, disagrees by four standard deviations at each Q^2 point from the assumption that $F_{1,n} \approx 0$.

Our analysis of the $N \to \Delta$ transition form factors is in preparation for publication.

---

*University of Tel-Aviv, Ramat Aviv, Tel-Aviv 69978, Israel.
†The American University, Washington, D.C. 20016.
‡University of Maryland, College Park, MD 20742.
§Lawrence Livermore National Laboratory, Livermore, CA 94550.
¶National Institute of Standards and Technology, Gaithersburg, MD 20899.
||Stanford Linear Accelerator Center, Stanford, CA 94305.
**Continuous Electron Beam Accelerator Facility, Newport News, VA 23606.
††University of Pennsylvania, Philadelphia, PN 19104.
‡‡University of Massachusetts, Amherst, MA 01003.
* University of Rochester, Rochester, NY 14627.
** University of California, Davis, California 95616.

[1] P.E. Bosted *et al.,* Phys Rev Lett **68** 3841 (1992).

[2] A. Lung *et al.,* Phys Rev Lett **70** 718 (1993).

6.4 Scaling analysis of Compton scattering on the proton

J. Beck and C.E. Hyde-Wright

In experiment E147 proposed for the Stanford Linear Accelerator (SLAC), we plan to measure the $p(\gamma,\gamma' p)$ and $p(\gamma,\pi^0 p)$ cross sections from 45° to 100° in the C.M. and for photon energies 6 GeV$\leq k < 13$ GeV. These are fundamental processes that probe the short range structure of the proton (& pion). Dimensional counting[1] predicts that at high energy, the Compton and π^0 cross sections should scale as: $d\sigma(\gamma,\gamma')/dt = s^{-6} f_\gamma(\cos\theta_{CM})$ and $d\sigma(\gamma,\pi^0)/dt = s^{-7} f_\pi^0(\cos\theta_{CM})$, where s is the invariant mass squared and t is the invariant momentum transfer squared. The angular distribution f_γ is particularly sensitive to the light cone wave function of the proton.[2]

In order to estimate the cross sections to be expected at large s and t, we compared existing Compton data with the scaling law. In the left hand panel below, we plot s^6 times the differential cross sections of Shupe *et al.*[3] Although the data are roughly consistent with the scaling law (horizontal on this plot), there are significant discrepancies at 45° and 90°. Even larger discrepancies are found for the π^0 data.

In the right hand panel below we compare Compton scattering and elastic electron scattering data. The scaling laws also predict that at high Q^2, the (e,e') cross section at fixed θ_{CM} scales as S^{-6}. In the right hand panel we plot the ratio of the Compton scattering data divided by a parameterization[4] of the electron scattering data, evaluated at the same incident energy and same momentum transfer $t(\gamma,\gamma') = Q^2(e,e')$. No firm conclusions can be drawn, but there is some improvement in the scaling, particularly at 45°.

[1] S.J. Brodsky and G.R. Farrar, Phys Rev Lett **31** 1153 (1973).
[2] A.S. Kronfeld and B. Nižić, Phys Rev **D44** 3445 (1991).
[3] M.A. Shupe *et al.*, Phys Rev **D19** 1921 (1979).
[4] $G_E = G_D$ (dipole), G_M from M. Gari and W. Krümpelmann, Z Phys A322 689 (1985).

6.5 Compton scattering and exclusive π^0 photo-production on the proton

J.F. Amsbaugh, J. Beck, P. Bosted,* C.E. Hyde-Wright and D.W. Storm

In SLAC Experiment E147 we propose to measure the Compton: $p(\gamma, \gamma' p)$ and exclusive π^0: $p(\gamma, \pi^0 p)$ cross sections at high momentum transfer. We will use the endpoint of a high flux bremsstrahlung beam on a 2 g/cm^2 liquid hydrogen target in End Station A at SLAC. Recoil protons will be detected in the 8 GeV spectrometer. Photons will be detected in a 1 m $\times$ 2 m Pb-Glass calorimeter segmented into 6 cm $\times$ 6 cm blocks. Compton and exclusive π^0 events are identified by the $p(\gamma, p\gamma)$ and $p(\gamma, p\gamma_1)\gamma_2$ reactions. These kinematics are constrained by the photon angular measurements alone and do not depend on photon energy resolution.

We estimate the count rates for Compton scattering and exclusive pion photo-production by extrapolating the lower energy data[1] assuming the scaling laws are valid (see previous article). Table 6.5 lists the kinematics of our proposed experiment. The count rates are listed in cols. 4 and 5 and various signal to background ratios are listed in cols. 6–8.

The $p(\gamma, \gamma' p)$ and $p(\gamma, \pi^0 p)$ reactions must be separated to identify each process. Both produce real coincidences between a proton and at least one photon. The difficulty in separating the processes is that the Compton cross section is 10 to 50 times smaller than the exclusive π^0 cross section. Because of the small mass of the pion, the four-momentum of a exclusive π^0 is nearly identical to the four-momentum k' of a Compton photon, and the recoil proton four-momenta for Compton and coherent π^0 events are not resolvable. The π^0 decays into two photons with the leading photon of energy $E_\pi/2 \leq k_1 < E_\pi = k'$ in a cone (in the laboratory) of half angle $\theta_1 \leq m_\pi/E_\pi$. In contrast, the Compton photon is spread out in solid angle only by the overall coincidence angular resolution. The ratio of the Compton photons to exclusive π^0 photons is determined by the ratio of cross sections divided by the fraction of the π^0 photons falling within the Compton angular resolution. The angular resolutions in- and out of- the scattering plane are σ_θ and σ_ϕ, respectively (1–5 mr, each). The ratio of Compton to exclusive π^0 photons within the Compton angular resolution is (Table 6.5, col. 6):

$$\frac{S[p(\gamma, p\gamma)]}{N[p(\gamma, p\gamma_1)\gamma_2]} = \frac{d\sigma(\gamma, \gamma')}{d\sigma(\gamma, \pi^0)} \frac{63\%}{2} \frac{m_\pi/k'}{\sigma_\theta} \frac{m_\pi/k'}{\sigma_\phi},$$

where 63% is the area within 1σ of a 2-D gaussian distribution.

In addition to true gamma-proton coincidences from Compton scattering and π^0 production, we will also face a background of inclusive $p(\gamma, p)X$ triggers in the 8 GeV Spectrometer in accidental coincidence with inclusive $(\gamma, \gamma')X$ photons in the calorimeter. The SLAC measurements[2] of the $p(\gamma, p)X$ yield at $-t \approx 1$ GeV and $k = 11.5$ GeV show that the integrated $p(\gamma, p)\pi\pi$ yield below ρ-threshold is approximately equal to the $p(\gamma, p)\pi^0$ yield. On the calorimeter side there is a large flux of inclusive photons, mostly from inclusive π^0 production. We have used unpublished measurements at SLAC of the inclusive charged pion yield (integrated over the bremsstrahlung flux) to estimate the inclusive photon production yield from the decay of neutral pions. Our resulting estimates are

*The American University, Washington D.C. 20016.

[1] M.A. Shupe *et al.,* Phys Rev **D19** 3828 (1973).

[2] R. Anderson *et al*, Phys. Rev. **D1** (1970) 27.

in agreement with inclusive photon data.[3] The mean energy from π^0 decay photons summed over four calorimeter blocks (solid angle $\Delta\Omega_4$) and integrated over 30 ns is always less than $0.1k'$. We have calculated the probability that the fluctuations in the inclusive photons yield a pile-up energy summed over four calorimeter blocks exceeding $0.3k'$ when integrated over any random 30ns ADC gate. The result we denote by P_{30}. We require four Pb-Glass blocks in order to fully contain the shower. We set a software threshold of $0.3k'$ to maximize our acceptance for π^0 photons $k_1 \geq k'/2$ while still maximizing our background suppression. We also assume that with a TDC on each calorimeter block, we can do proton-photon coincidence timing to a precision of 5 ns (full width), thus effectively dividing the ADC gate into 6 intervals. Thus the ratio of the Compton signal to accidental coincidences background is (Table 6.5, col. 7):

$$\frac{S[p(\gamma,\gamma p)]}{N[p(\gamma,\gamma')X]} = \frac{d\sigma(\gamma,p\gamma)}{d\sigma(\gamma,p)X} \frac{63\%}{(\pi\sigma_\theta\sigma_\phi)} \Big/ \frac{(P_{30}/6)}{\Delta\Omega_4}.$$

The net signal to background for Compton photons is the inverse of the sum of the inverses of columns 6 and 7 of Table 6.5.

The leading photons from exclusive π^0 production must also be separated from the random coincidence background. One half of the leading photons lie within a solid angle $\pi(m_\pi/k')^2/3$ Thus the signal to noise ratio for the leading photons from exclusive π^0 production is (Table 6.5, col. 8):

$$\frac{S[p(\gamma,p\gamma_1)\gamma_2]}{N[p(\gamma,\gamma')X]} = \frac{d\sigma(\gamma,p)\pi^0}{d\sigma(\gamma,p)X} \frac{3/2}{\pi(m_\pi/k')^2} \Big/ \frac{P_{30}/6}{\Delta\Omega_4}.$$

Although the exclusive pion rate is much greater than the Compton rate, the photons from exclusive pion production are spread out over a much larger solid angle.

[3] A.M. Eisner *et al*, Phys. Rev. Lett. **33** (1974) 865 and D.O. Caldwell *et al, ibid.*, 868.

Table. 6.5

$p(\gamma,\gamma' p)$ Kinematics, Count Rate, and Signal to Background

1	2	3	4	5	6	7	8
θ_{CM} (deg)	$-t$ (GeV/c)^2	k' (GeV)	$p(\gamma,p)\gamma$ (Hour^{-1})	$p(\gamma,p)\pi^0$ (Hour^{-1})	$\frac{S[p(\gamma,\gamma)p]}{N[p(\gamma,\pi^0)p]}$	$\frac{S[p(\gamma,\gamma)p]}{N[p(\gamma,\gamma')X]}$	$\frac{S[p(\gamma,\pi^0)p]}{N[p(\gamma,\gamma')X]}$
k = 6.0 GeV		S = 12.1 GeV^2					
51.4	2.0	4.9	42.0	1383.	3.0	8.9	2.2
60.0	2.6	4.6	21.9	715.	2.6	8.1	2.3
69.5	3.4	4.2	13.5	430.	2.3	7.7	2.6
79.6	4.3	3.7	10.5	323.	1.9	7.2	2.8
90.0	5.2	3.2	10.3	306.	1.4	3.9	2.0
100.4	6.1	2.7	11.8	341.	1.0	1.6	1.2
k = 8.8 GeV		S = 17.4 GeV^2					
60.0	3.9	6.7	9.2	208.	2.8	7.8	2.1
69.5	5.1	6.1	5.8	127.	2.4	4.4	1.4
79.6	6.4	5.4	4.5	97.	2.0	4.9	1.9
90.0	7.9	4.6	3.6	74.	1.5	2.3	1.2
100.4	9.3	3.9	3.1	63.	1.0	1.0	0.8
110.5	10.6	3.2	3.0	59.	0.6	0.4	0.5
k = 12.9 GeV		S = 25.2 GeV^2					
69.5	7.6	8.9	2.0	30.	2.3	3.4	1.1
79.6	9.6	7.8	1.1	16.	1.9	2.1	0.9
90.0	11.7	6.7	0.8	11.	1.4	1.4	0.7
100.4	13.8	5.6	0.7	9.	1.0	0.7	0.5

6.6 Shielding studies for a high energy photon calorimeter

J.F. Amsbaugh and C.E. Hyde-Wright

Our proposed measurements of the Compton: $p(\gamma,\gamma' p)$ and exclusive π^0: $p(\gamma,\pi^0 p)$ cross sections were described in the previous article. Here, we discuss some GEANT monte carlo studies of the calorimeter response. The calorimeter, located 20 m from the target, consists of 20×25 F-2 lead glass segments each 6 cm square and 60 cm long, along the photon flight path. The radial extent of a few GeV shower is half a segment. We will integrate each block with a 30 ns gate and sum four adjacent blocks in software to reconstruct the desired shower signal, including events near a block edge or corner. In addition to our signal, we face a background from pile-up of atomic compton photons: $e(\gamma,\gamma')e$ and photons from inclusive π^0 production: $p(\gamma,\pi^0)X$.

In the figures below, we present calculations of the separation of signal from background for the kinematics $k = 8.8$ GeV, $k' = 4.7$ GeV and $\Theta_\gamma^{\mathrm{CM}} = 90°$ (see table 6.5). In these kinematics, the pile-up of atomic compton photons is 185 photons of 5 MeV each (integrated over 30 ns and summed over 4 blocks), or 20% of k'. We will place a low-Z (C) absorber in front of the the calorimeter to preferentially absorb these low energy photons. After 2 radiation lengths of C ($2X_0$), the atomic compton pile-up is only 4% of k'. In Fig. 6.6-1 we show the pile-up in the calorimeter of photons from inclusive π^0 production. The distribution is generated from a fit to unpublished π^- production data at SLAC. The histograms are for absorbers of $0X_0$, $2X_0$, & $3X_0$. We plan on setting a software threshold at 30% of k' to separate our signal from background pile-up. In Fig. 6.6-1, the probability of pile-up in excess of $0.30k'$ is 5%, 1.25%, and 0.4% for $0X_0$, $2X_0$, & $3X_0$, respectively. The signal to background ratios in Table 6.5-1 were generated using the $0X_0$ results. In Fig. 6.6-2, we show the energy distribution in the calorimeter for the leading photon from exclusive π^0 production: $p(\gamma, p\gamma_1)\gamma_2$; $(k'/2) \leq k_1 < k'$. The three curves are again for $0X_0$, $2X_0$, & $3X_0$. With a threshold at $0.30k'$, the leading photon inefficiency is 0.0%, 0.2%, and 3.4%, for $0X_0$, $2X_0$, & $3X_0$, respectively

We conclude that the background of inclusive and atomic compton photons can be separated from our signal. More complete calculations are in progress.

7 Ultra-Relativistic Heavy Ion Collisions

7.1 Ultra-relativistic heavy ion physics: an introduction

H. Bichsel, P. Chan, J.G. Cramer, D.J. Prindle, T.A. Trainor and X. Zhu

The ultra-relativistic heavy ion (URHI) group of the University of Washington Nuclear Physics Laboratory is interested in the physics of nucleus-nucleus collisions in which the rest masses of the colliding nuclei represent a negligible fraction of the net mass energy of the system. Up to now our physics focus has been on Hanbury-Brown-Twiss interferometry on such systems, using the Bose-Einstein correlations of the many pions from the collision to deduce the space-time evolution of the hot pion source.

We are participants in three major experiments: CERN Experiment NA35, CERN Experiment NA49, and the Brookhaven/RHIC STAR detector system. The NA35 experiment used a 1.5 T superconducting magnet to analyze particles produced in the collisions and records tracking data from a streamer chamber and a large time projection chamber (TPC). The data collection phase of NA35, involving collisions of 200 GeV/A oxygen and sulfur beams from the CERN SPS with various fixed targets, extended from 1986 to 1992 and is now complete. The UW URHI group participated in the last two CERN runs of the experiment (fall 1991 and spring 1992). Much of the recent activity of our group has been focused on refining techniques for the analysis of data from the NA35 TPC and understanding the problems implicit in the detection and recording techniques.

Experiment NA49 is an expanded version of Experiment NA35. It will use four TPCs, two of which will be placed in two high-field magnets. It will run in the last half of 1994, when lead beams are available from the CERN SPS. The participation of the UW URHI group in NA49 is focused on development and construction of the "vertex" TPCs located in the two magnets. Our investigations of the tracking problems in the NA35 TPC is in part related to improvements in the design of the TPCs for NA49, where much higher track densities will be present.

The STAR detector (Solenoidal Tracker At RHIC) is one of the two major detector systems for the Relativistic Heavy Ion Collider (RHIC) presently under construction at Brookhaven National Laboratory. The STAR system consists of a large "warm" solenoidal magnet producing a longitudinal magnetic field of 0.5 T, within which are several layers of detectors. From the collision vertex outward, the detector systems of STAR are: (1) the silicon vertex tracker (SVT), (2) the time projection chamber (TPC), (3) the time-of-flight system and central multiplicity trigger (TOF), and (4) the electromagnetic calorimeter (EMC). The UW URHI group's participation in STAR has been concentrated up to now in the SVT system and the triggering system.

In the past year we have received a special Capital Equipment Grant from the U. S. DOE that allowed us to purchase two high speed HP-9000/710 RISC workstations and associated equipment. One of these machines was taken to CERN for the spring 1992 NA35 run and proved extremely valuable for monitoring the data stream, analyzing data, and performing simulations during the run. The workstations have also provided powerful support for analysis and simulations at the NPL in the past year. They are described in more detail in article 12.2.

7.2 Comparison of "candidate" 3-body Coulomb corrections to HBT

J.G. Cramer and V. Efimov*

Several thousand pions of each charge may be emitted by one central heavy ion collision at the ultra-relativistic energies of the planned RHIC (BNL) and LHC (CERN) colliders. With this large number of final-state particles it is very likely that any pair of pions selected for low relative momentum for use in Hanbury-Brown-Twiss (HBT) interferometry will have one or more *additional* pions nearby in momentum space. Therefore in using interferometric methods to determine emission source sizes, HBT analysis with three or more particles may be unavoidable.

The Coulomb correction is a serious difficulty in HBT interferometry with three or more charged particles because there is no known general solution to the n-body Coulomb problem with $n > 2$. Published three-particle HBT analyses[1] have used the *ad hoc* Coulomb correction: $F_1 = G(\eta_{12})G(\eta_{23})G(\eta_{31})$, where $G(\eta_{ij}) = 2\pi\eta_{ij}/[\exp(2\pi\eta_{ij}) - 1]$ is the Gamow penetrability and $\eta_{ij} = z_i z_j \alpha/\beta_{ij}$ is the Sommerfeld parameter, with $z_k e$ the electric charge of particle k, α the fine structure constant, and β_{ij} the relative velocity between the interacting particles. This three-particle Coulomb correction is not unique. One of us[2] has used superposition arguments to construct two alternative three-particle Coulomb corrections that have the forms: $F_2 = \frac{1}{3}[G(\eta_{12})G(\eta_{23}+\eta_{31}) + G(\eta_{23})G(\eta_{31}+\eta_{12}) + G(\eta_{31})G(\eta_{12}+\eta_{23})]$ and $F_3 = G(\eta_{12}+\eta_{23}+\eta_{31})$.

As a way of testing these and other "candidate" forms of three-particle Coulomb correction, we have considered the general Coulomb three-body problem in several limiting cases in which it is more tractable. In particular, we have considered the cases where (a) all three particle pairs are at very large relative momentum, (b) pairs 23 and 31 are at very large momentum while pair 12 is at an intermediate relative momentum, (c) three like-charge pairs (+++) are all at very small momentum, and (d) three mixed-charge pairs ($+-+$) are all at very small momentum. All three of the functions given above are found to have the proper asymptotic behavior in the high momentum limits (a + b)ve the proper asymptotic behavior in the high momentum limits (a + b), but all have incorrect asymptotic behavior in the low momentum limits (c + d).

Therefore, we have constructed a fourth Coulomb correction factor which has the correct asymptotic behavior in all for momentum limits. It has the form:

$$F_4 = F_3\ [1 + C_4/(\eta_{12}^{-2} + \eta_{23}^{-2} + \eta_{31}^{-2})]^{\frac{3}{2}},$$

where C_4 is an undermined constant to which we assign a provisional value of 3. Comparison of the four candidate functions shows that all have very similar behavior for the like-charge (+++) case but differ markedly for the mixed-charge ($+-+$) case.

---

*Physics Department, University of Washington, Seattle, WA 98195.

[1]Y.M. Liu, D. Beavis, S.Y. Chu, S.Y. Fung, D. Keane, G. Van Galen, and M. Vincent, Phys. Rev. C **34**, 1667 (1986).

[2]J.G. Cramer, Phys. Rev. C **43**, 2798 (1991).

7.3 Maximum likelihood analysis in HBT interferometry

J.G. Cramer, D. Ferenc* and M. Gaździcki*

HBT interferometric measurements are quite demanding experimentally because they require high statistical and systematic precision and good momentum resolution from the experimental apparatus. The HBT technique has already been used effectively in collisions where the source size is about 1–6 fm. However, as the source size increases with the energy and masses of the colliding nuclei, HBT interferometry becomes more difficult because the correlation function becomes very narrow in relative momentum, reducing the statistics of correlated particle multiplets in the region of source-size sensitivity and demanding very good momentum resolution for meaningful analysis. It is therefore of considerable interest to devise an analysis scheme that uses all of the available information about the data and its systematic and statistical errors.

We have devised a new Maximum Likelihood procedure for fitting the space-time size parameters of the particle production region in ultra-relativistic heavy ion collisions. The probability $S(\vec{q};\,\vec{r})$ of finding pairs of pions correlated with relative momentum $\vec{q}$ from a pion source with space-time geometry described by $\vec{R}$ is:

$$S(\vec{q};\vec{R}) = C(\vec{q};\vec{R})G(\vec{q})B(\vec{q})/N(\vec{R})$$

where $C(\vec{q};\,\vec{R})$ is the Bose-Einstein correlation function, $G(\vec{q})$ is the Coulomb correction (usually a Gamow penetrability), $B(\vec{q})$ is the uncorrelated background distribution, and $N(\vec{R})$ is the probability normalization factor obtained by integrating the other terms over $\vec{q}$. We find that if the S factor for each input data point is convoluted over the local error matrix of the measurements before including its contribution to the likelihood function, one is in effect taking into account all of the available information on experimental errors and applying appropriate point-by-point weighting of this information.

This procedure offers two significant advantages over the usual binning and chi-squared fitting procedure: (1) it does not require sorting of the correlation data into arbitrary bins in the multidimensional momentum space and (2) it applies all available information on the experimental resolution error matrix separately to each correlated particle multiplet analyzed. These features permit extraction of maximum information from the data. The technique may be particularly important in ultra-relativistic heavy ion collisions, because in this energy domain large source radii and long source lifetimes are expected, and high-multiplicity HBT interferometry with a single collision event is a possibility.

This work is reported in detail in IKF Report IKF-HENPG/92-3, which is available on request. We plan to test the method with simulations and to publish a paper on the results.

*Institut für Kernphysik, Universität Frankfurt, Germany.

7.4 HBT source size dependence on (p_t,y) and TPC resolution

T.A. Trainor

The technique of using spacio-temporal correlations among radiated bosons to determine radiating source sizes was first developed by Hanbury-Brown and Twiss to measure stellar diameters. More recently it has been applied to populations of charged pions emitted during nuclear collisions to determine the dimensional properties of hot nuclear matter. In the latter studies it is of interest to determine whether the apparent source size depends on the momenta of emitted bosons in order to investigate the dynamical changes in the source during the particle emission phase.

The natural kinematic variables for a relativistic collision are (p_t,y), where p_t is the emitted particle momentum component transverse to the beam direction and y is the rapidity ($y=\frac{1}{2}\ln((E+p_{11})/(E-p_{11}))$). Each detected pion for a collision event is located in this space by the detector system. HBT analysis is then a study of correlations in the metric space (p_t,y). The finite resolution of the detector system sets limits on the magnitude of the source size which can be determined with the HBT technique. Certain aspects of the measurement process can be seen as "mixing" the metric space within some characteristic length and setting a lower limit on the validity of the metric definition. Due to the reciprocal nature of source size and metric resolution this mixing sets an upper limit on source size sensitivity. Another limiting factor is the Coulomb interaction among the radiated particles in flight, which is treated elsewhere.[1] Since a goal of the ultrarelativistic heavy ion program is to look for large source sizes as a signal of quark deconfinement or other unusual QCD phenomena it is of interest to understand how the finite resolution of the boson detection system limits the size determination.

[1]See section 7.2, this report.

The system of choice for large-acceptance measurements of emitted particle phase space is the time projection chamber (TPC). In other articles included here we review our efforts to understand in detail the error system for a large-volume TPC with high track density as used in recent runs at the CERN SPS (NA35). I sketch here the relation between these error determinations and the implications for HBT analysis.

In Fig. 7.4-1 I show a cartoon of a projection of phase space corresponding to a TPC some distance from a fixed target and offset from the beam (NA35), with error pixels added to represent the error as determined from our data analysis. Fig. 7.4-2 shows the result of mapping these pixels into the corresponding (p_t,y) space. It can be seen from this simple exercise that, whereas the errors may be fairly uniform in the TPC measurement space, the consequential errors in the momentum space vary widely with mean momentum. The result is that the inferred source dimensions, uncorrected for finite resolution, may have an apparent momentum dependence which is not characteristic of the true collision dynamics. The correction process involves a representation of the error as a tensor field on (p_t,y) which is then transformed into the Q_{inv} correlation space, and unfolded from the uncorrected correlation. The correction process may be carried out either in a binned correlation space or with a bin-free approach using the maximum likelihood method.[2]

[2] See section 7.3, this report.

7.5 NA35 TPC track variance analysis

H. Bichsel, P. Chan, H.G. Fischer,* T.A. Trainor and X. Zhu

The future heavy-ion physics programs at SPS, RHIC and LHC will rely strongly on TPC tracking devices. These devices will have to function with very high track densities, requiring optimization of the TPC technology. The NA35 TPC track data from sulfur-nucleus runs on the CERN SPS represent an extensive and unique data set with which to develop optimum tracking strategies in a high density environment. We have identified and analyzed the major sources of variance in these data, and are developing strategies to minimize these variances.

Within the TPC the sources of variance that have been well studied in the past include diffusion, Landau fluctuations and binning structures, such as pad layouts, time samples and sector boundaries. Systematic errors arising from distortions in the pad planes and drift fields are also well known.

Our recent analysis of NA35 TPC data has revealed additional sources of variance resulting from or made apparent by high track densities or beam tracks. These include alien clusters and cluster fragmentation, where clusters are contiguously occupied bin aggregates. Cluster fragmentation can occur when a low energy delta electron produces a highly structured secondary track which is broken up by the track finder program into separate orphan clusters. Alien clusters are associated with the wrong track through chance proximity. The probability of alien clusters is a function of track density and orphan cluster production. Attachment of alien clusters in the volume of the TPC mainly increases the rms errors of the track geometry parameters. However, at sector boundaries (e.g., the TPC wall) asymmetric attachment results in significant systematic errors in mean values of track parameters and corresponding distortions of inclusive spectra. Pad calibration errors revealed by studies of beam tracks are also seen to be a significant source of random error.

Methods currently being developed at Seattle to minimize these variance sources include more general cluster finding techniques, cluster moment analysis to provide a rejection criterion, and optimized alien cluster rejection by means of location-dependent fiducial volumes around tracks. The cluster moment criterion is a generalization of the well-known technique of reducing dE/dx variance by rejecting a fraction of clusters based on cluster charge (zeroth moment). This idea is extended and applied also to track geometry parameters.

In addition to reducing systematic spectrum distortions, we are motivated by interest in increased sensitivity to large source sizes as determined by HBT analysis. One upper limit on source size as determined by the HBT technique is the degree of small-scale "mixing" of phase space resulting from track variances. This is related to but not equivalent to the question of two-track resolution. The present analysis should serve to increase this upper limit and determine the true uncertainty in measured source dimensions. The following articles describe some of this work in greater detail.

*EP Division, CERN, Geneva, Switzerland.

7.6 Cluster moment analysis for NA35 TPC data

P. Chan, J.G. Cramer, T.A. Trainor and X. Zhu

In the CERN ultra-relativistic heavy ion experiment NA35, a time projection chamber (TPC) was used to provide 3D visualization of particles produced in the collision of 200 GeV/nucleon sulfur and deuterium nuclei from SPS with various targets. The TPC has a volume of 2.6 $m \times 1.6\ m \times 1.1\ m$ divided into 60 vertical planes along the TPC length, each with 256 bins (pads) by 512 bins (time-buckets) for sampling of charge deposition from ionization of charge particles traversing the TPC volume. Neighboring bins (in both pads and time direction) are grouped together to form clusters. The track reconstruction program (TRAC) selects valid clusters, computes their mean positions and charge they are collected, and determines particle trajectories.

We have observed that the deviations of cluster centroids from the best fit track in pad space (σ_y) are larger than the values obtained from simulations using known gas detector physics. Moreover, from simulations done by Hans Bichsel, we see charge deposition due to delta electrons change the statistics, particularly the mean position of a cluster.[1] Such clusters would not only confuse present cluster finding algorithm but would also degrade the quality of tracks reconstructed. To eliminate clusters associated with delta electrons, a statistical analysis of the clusters was done. Clusters associated with a track found by TRAC were examined by calculating the second, third and fourth moments about the mean of the clusters. We expected to see some clusters with higher moments that deviate significantly from the normal population.

However, as shown in Fig. 7.6, the expected deviation was not found. It turns out that TRAC breaks up large clusters into smaller independent clusters. Therefore the moment analysis failed to identify clusters associated with delta electrons. We conclude that in order to utilize moment analysis effectively, the track reconstruction program TRAC must be modified to identify clusters appropriately.

Fig. 7.6: $\sqrt{m_2}$, $\sqrt[3]{m_3}$, and $\sqrt[4]{m_4}$ vs m_o, where m_i is the i^{th} central moment of the cluster.

[1]H. Bichsel, *Calculation of energy deposition in argon gas for NA 35 and NA 49 TPCs*, this report.

7.7 Alien clusters and calibration anomaly

P. Chan, J.G. Cramer, D.J. Prindle, T.A. Trainor and X. Zhu

In the variance studies,[1] we are primarily interested in the magnetic field off data due to the simple geometry. In the following studies, we analyze two such runs: run 1848 and run 1797. Run 1848 is a central event run, and run 1797 is a Sulfur beam run. The runs are evaluated using TRAC[2] which gives as output tracks and the associated clusters. The scattering of the clusters with respect to the track position is the subject of study. For convenience, we denote the RMS scattering of the clusters in pad direction as σ_y and that in drift direction as σ_z.

Fig. 7.7 (a) shows the position resolutions σ_y and σ_z as a function of z (drift direction) and y (pad direction) for the central event run 1848 . Each point corresponds to a particle track. The apparent "hooks" at the TPC boundaries arises from the inclusion of alien clusters, ie clusters not belonging to the track. The alien clusters degrade TPC resolutions in the volume and produce the hooks at the boundaries. This manifestation can be understood as follows. At the boundaries of a TPC, there is no cluster on one side of a track. If the criteria for accepting clusters in track finding is too tolerant, alien clusters can be preferably included on the other side of the track, producing large σ's. This is indeed the case for TRAC. Effectively TRAC accepts clusters within a radius of 3.5 mm or greater which is more than 7σ away from the true position. To clean up the hooks, we reduce this radius to 1.5 mm. Fig. 7.7 (b) shows the effect after this cleanup. The hooks are gone and the resolutions improve. Since track density and resolutions are not uniform inside the TPC, it is expected that the optimum radius should depend on the position inside the TPC. Further study is needed to optimize this parameter.

Since Sulfur beam is highly ionizing, the sulfur tracks are localized with excellent position resolution. In this case, the electronic noise is the dominant contributor to the resolution. Fig. 7.7 (c) shows σ_y as a function of y for the Sulfur beam run 1797. We observe an anomaly at $y = 58.4$ cm. Within 100 micron of change in y, the resolution σ_y nearly doubled, jumping from 200 micron to 340 micron. The problem is traced to a few padrows which give outstanding beam position. Fig. 7.7 (d) shows the improvement after excluding these problematic padrows. The signals on those problematic padrows look normal, so the problem has to be in the relative gain calibration of the individual pads. From this study, we conclude that the error in the pad to pad gain calibration is not negligible. This suggests that for the future high track density experiments such as NA49 and STAR, it is very desirable to have a reliable pad to pad gain calibration.

[1] T.A. Trainor *et al.*, *NA35 TPC Landau Fluctuation and Diffusion Analysis*, this report.

[2] Tracking and Analysis Code, written by G. Roland, IKF, Frankfurt, Germany.

Fig. 7.7. (a) TPC resolutions for central event (TRAC); (b) TPC resolutions for central event (TRAC with reduced radius); (c) TPC resolution for Sulfur beam, all padrows; (d) TPC resolution for Sulfur beam, excluding problematic padrows.

7.8 NA35 TPC Landau fluctuation and diffusion analysis

T.A. Trainor

The error analysis presented elsewhere in this section covers mainly new sources of track parameter variance resulting from high track densities or the consequences of specific features of the NA35 TPC. In order to make clear the nature of these sources it was important to describe clearly the standard variance sources that have become well understood in the past. I have developed analytic representations of the two major variance sources, diffusion and Landau fluctuations, as functions of position in the TPC volume which can then be compared with observed error distributions in the data. Z. Zhu developed a Monte Carlo simulation code for the same purpose which is described elsewhere in this section.

Fig. 7.8-1 represents the effects of diffusion during drift of track electrons to the pad plane. A charge distribution localized at point of creation (on the left) arrives at the pad plane with a finite spread (on the right). The width parameters in the nondrift and drift directions are given in terms of TPC position along the drift as $\omega_y = 0.53mm\sqrt{z(cm)}$ and $\omega_z = 0.34mm\sqrt{z(cm)}$. On a given pad row the centroid of a cluster can be considered as the result of sampling a 2D gaussian distribution with the above "widths" by the total number of secondary charges intercepted by the row. This gives the diffusion component of the total variance.

Fig. 7.8-2 represents the effects of Landau fluctuations. The interaction of a fast charged particle with a medium involves Poisson-distributed collisions with primary atomic electrons. The distribution of energy transfers is determined by the Coulomb cross section. The resulting primary electron energy distribution goes as $1/E^2$ at higher energy, and is effectively cut off below atomic binding energies, with some complexity just above threshold. The result is a departure from Poisson in the distribution of charge along the energetic particle track which has the effect of lowering the **apparent** number of primary charges and thus increasing the effective Poisson variance. The corresponding effect on cluster and track parameters depends on the slope ($\tan\alpha$) of the particle track with respect to the pad row.

If tanα is nonzero then the primary electrons associated with a given pad row appear to be distributed in a rectangular distribution along the pad row with width given by $dx_0 \cdot \tan\alpha$, where dx_0 is the length of a pad along the nominal track direction. Some of these electrons have sufficient energy to produce secondary electrons at the point of creation or near by. The result of this is that the rectangular distribution appears to be sampled not by the number of primaries N, but by a smaller number N_{eff} $(1 < N_{eff} < N)$, because the distribution of secondaries effectively weights the primaries unequally. The variance in the cluster centroid determination produced by this effect is just $(dx_0 \cdot \tan\alpha)^2/N_{eff}$ where N_{eff} is the effective number of samples as discussed above.

The middle figure illustrates the effect. The rectangular projection is sampled by a number of primary electrons (shown after diffusion) one of which is energetic enough to produce secondaries. The resulting distribution is altered from the case with no secondaries produced. The best that can be done to reduce this variance is to orient the effective pad row direction normal to the local mean track direction. In that case the remaining spread in tanα about a mean value of zero will be determined by the distribution of particle momenta.

Fig. 7.8-3 represents a summary, in the horizontal ($\hat{x}$-$\hat{y}$) plane, of the above two variance sources plus a uniform platform of channel electronic noise, as distributed within the TPC volume. The lower two surfaces show this functional dependence. The upper two surfaces show the observed variances for TPC data as analyzed by the track finding program TRAC. The discrepancy between these two results motivated the track variance analysis described elsewhere in this section.

Fig. 7.8-2

7.9 Energy loss spectra for argon gas

H. Bichsel

In order to make reliable calculations of energy loss and energy deposition in any absorber, it is necessary to have a reasonably good energy loss spectrum $\sigma(E)$ for single collisions, in which energy E is lost by the charged particle. The Rutherford spectrum

$$\sigma_R(E) = k/E^2, \quad k = \frac{2\pi z^2 e^4}{mv^2}$$

is frequently used, but is not a very good approximation. A better one can be obtained with the Weizsäcker-Williams method, using the optical absorption function for the material.[1]

The collision cross section for argon (ρ =1.6 mg/cm^3) calculated with this approach, relative to the Rutherford cross section, is shown in Fig. 7.9-1. Contributions from each atomic shell are marked. Clearly, "distant collisions", given by dipole transitions, are quite important. The Rutherford cross section is shown by the horizontal line.

The total cross section, $\sigma_t = \int \sigma(E)\, dE$, gives the average number of collisions per cm experienced by particles. For 200 MeV π it is 24/cm, and the average energy loss per collision is 97 eV. About 1% of the pions will produce a δ ray with $E > 40$ keV and a range of about 15 mm.

The energy loss spectrum ("straggling function") $f(\Delta)$ for an absorber in which many collisions take place can be obtained with the convolution method.[2] Such a spectrum calculated for 200 MeV π traversing 4 cm of argon gas is shown in Fig. 7.9-2. For comparison the Landau function (based on the Rutherford cross section) is also shown (dashed line). The mean energy loss, calculated with the stopping power dE/dx=2.41 MeV/cm, $< \Delta >$=9.6 keV is shown; a more appropriate value to identify the function is the most probable energy loss, Δ_p =5.3 keV. A function including only collisions with $E < 3.2$ keV is given by the dotted line.

Fig. 7.9-1.

Fig. 7.9-2.

[1] Allison and Cobb, Ann Rev Nucl Part Sci **30** (1980) 253

[2] H.Bichsel, Rev. Mod. Phys. **60**, 663 (1988)

7.10 Calculation of energy deposition in argon gas for NA35 and NA49 TPCs

H. Bichsel

In the NA35 and NA49 time projection chambers (TPCs) the trajectories of energetic particles ($\beta\gamma \geq 2$) are observed. In order to determine the uncertainty in the location of the tracks, the structure of the primary ionization events must be known. The ionization is measured on "pads" with a length of 4 cm and a width of 6 mm, with the particles travelling along the length. Thus the ionization over a distance of 4 cm must be described (see previous section).

Secondary electrons (δ rays) which are produced if the energy loss E exceeds 15.9 eV (the ionization energy of Ar), will produce further ionization. The maximum energy loss for 200 MeV π is E_M =4.9 MeV (range about 15 m). The total number of ion pairs produced at Δ_p is $J = \Delta_p/w$ (with $w \sim$ 25eV, $J \sim 200$). For $E < 100$ keV, δ rays will be emitted at angles between 70^o and 90^o with respect to the particle trajectory.[1] Thus they will produce a displacement of the mean location of the observed ionization distribution from the particle track. These ionization distributions can be simulated with Monte Carlo calculations. It is not necessary to make them with the complete collision spectrum $\sigma(E)$ (section 7.9); since the lateral spatial resolution of the TPC is at best about 0.1 mm, we can use a primary energy deposition function ("core") given by the analytic function for energy loss with maximum energy loss E_M = 750 eV (the effective range of 750 eV δ rays is $\sim$ 0.026 mm). The energy deposition is shown in the figure: the energy deposited by the core is shown by the symbol, the solid line shows the energy deposition in 0.5 mm bins along the tracks of the δ rays.

Then the Monte Carlo calculation must only be made for $E > 750$ eV, with a mean number of 1.03 collisions over the pad length, and with a distribution of collisions given by a Poisson distribution. Thus, out of calculations for 10,000 pions, 3600 will make no δ rays with $E > 750$ eV, 3600 will make one collision, 1900 will make two collisions, etc. The calculation then is much faster. A program has been written to simulate the primary ionization events, and a first approximation to simulate the transport of the ions to the electrodes has been made. Further refinements are needed.

Fig. 7.10.

[1] The mean free path between collisions with $E > 100$ keV is about 9 m.

7.11 NA35 TPC data analysis program (TRAC)

P. Chan, J.G. Cramer, D.J. Prindle, T.A. Trainor and X. Zhu

TRAC is a track reconstruction program written by Gunther Roland, IKF Frankfurt, to analyze NA35 TPC data. The program relieves the burden of going through a tremendous quantity of raw data to obtain useful information. We have been examining the algorithms used in TRAC and we are now coming to an understanding of the causes of large systematic shifts observed in the parameters of the reconstructed tracks.

To help us to determine the origins of the observed distortions, we have added several features to TRAC. By setting different switches before compiling the program, one can write to a file raw data, information on specific clusters, and/or tracks. A cluster moment analysis algorithm was added to TRAC to perform statistical analysis of clusters associate with tracks found by TRAC. Cluster centroid deviations, σ_y and σ_z are calculated directly from cluster and track parameters, instead of inferring from the uncertainty in determined track parameters. This information is now available in the output file.

After an in-depth study of the information provided by TRAC, we believe that in order to reduce systematic shift, several section of TRAC must be modified. In the cluster finding algorithm, TRAC breaks up a large cluster into smaller individual clusters. Fig. 7.11 shows examples of two clusters. On the left is a typical cluster of deuteron beam with the size of 3 bins (pads) by 6 bins (time-buckets). On the right is a cluster of δ electron emerging from lower right corner undergoes multiple scattering. In the latter case, TRAC divides it into five individual clusters, each enclosing a local maximum of charge. Therefore, not only is TRAC incapable of identifying cluster associates with δ electrons, but it also creates extra clusters which are likely to degrade track quality. To solve this problem, TRAC needs to be modified in such a way that contiguous bins are identified as in one cluster. Then cluster moment analysis can be used to distinguish clusters associate with δ electron. Such modifications are now being implemented.

Fig. 7.11. Left: Typical cluster of a deuteron beam. Right: Cluster of a δ electron emerging from lower right corner.

7.12 NA35 TPC phase space representations

T.A. Trainor

The NA35 TPC had a drift volume 1 m high and 1.2 m x 2.4 m in horizontal cross section. The pad plane, which defined the top surface of the drift volume, was divided into six or eight sectors during the fall, 1991 (6) or spring, 1992 (8) sulfur-nucleus run at the CERN SPS. Each sector contained 15 pad rows with 128 6 mm x 40 mm pads in each row. The total number of instrumented pads was 5760 for the first run and 11,520 for the second run. Some sectors were only partially instrumented in each run.

The signal from each pad, proportional to the induced charge resulting from track charges arriving at the pad plane from the drift volume, was sampled periodically and digitized. The resulting data represent a record of the charge deposited in discrete bins in the TPC drift volume as defined in three dimensions by the pad layout and the time sample structure.

The off-line track finder program TRAC[1] first looks for contiguously occupied bin aggregates, called clusters, among the raw data for an event. Two-dimensional clusters are identified for each pad row separately. The centroid of each cluster is then identified as a potential space point on a straight line track.

TRAC then examines the set of all identified space points for straight line correlations using a follow-your-nose tracking algorithm. Each such correlation is fitted with a straight-line hypothesis, and track parameters such as slopes, intercepts (in two planes), and mean energy loss (dE/dx) are obtained.

The final stage of this part of the data analysis consists of transforming the track geometry parameters to transverse momentum and rapidity. This requires details of the TPC position with respect to the beam and field profiles of the vertex magnet used for momentum analysis.

In order to determine the error propagation and identify sources of systematic errors and variance I have found it useful to develop a phase-space representation of the TPC data. With the beam direction designated as $\hat{x}$ the vertical (drift) direction is $\hat{z}$ and the horizontal direction is $\hat{y}$. I then define two phase space projections, y-space ($\hat{y}$,$\hat{y}'$) and z-space ($\hat{z}$,$\hat{z}'$). Each track is represented by one point in each of these spaces. Other ancillary spaces which are useful involve one of these geometry variables in combination with another track parameter such as dE/dx, cluster centroid rms deviation (σ_y, σ_z), curvature ($1/\rho$), or cluster number.

As an example of application of these spaces I show here the y-space corresponding to central (high multiplicity) events with sulfur on gold for which the vertex magnet field was off. One then expects a straight-line correlation in y-space and z-space corresponding to straight tracks radiating from a point source at the target. I also show the same space transformed so that the nominal correlation should be along $\hat{y}' = 0$. In this "focussed" space deviation from the expected correlation reveals statistical and systematic deviations resulting from multiple scattering on air and systematic effects in the track-finding algorithm. These spaces or variants resulting from linear transformations have been used extensively to unfold the error system for the NA35 data.

[1]Gunther Roland, IKF, Frankfurt, Germany.

Fig. 7.12.

7.13 Decoding the position-angle ambiguity of the NA35 TPC

J.G. Cramer

CERN Experiment NA35 uses a large time projection chamber (TPC) mounted about 5.5 m downstream of a large superconducting magnet producing a vertical magnetic field of 1.5 T. The TPC is suspended from overhead rails that all its positioning on either side of the 200 GeV/A particle beam, or even in the beam itself. A CERN surveying team sighted in the angle and position of the TPC at the beginning of both the Autumn 1991 and the spring 1992 runs of NA35. However, due to the movement of the TPC during the running periods and less-than-optimum construction of the support structure, the lateral (y_0) and vertical (z_0) location of the TPC and its rotation angle (ϕ_z) about the vertical axis are not sufficiently determined, without additional calibrations, for precise determination of the momenta of the particles tracked in the TPC.

For this reason it is necessary to use calibration field-off (B=0) runs to more precisely determine the location and orientation of the TPC. Unfortunately, in locating the TPC by extrapolating tracks back to the target position there is an ambiguity between y_0 and ϕ_z in interpreting the calibration data. This difficulty could have been avoided by performing the B=0 calibrations with *two* well separated targets in the beam, but unfortunately this was not done.

There are therefore several alternatives for breaking the (y_0,ϕ_z) ambiguity. (1) assume that the TPC does not rotate as it is translated; (2) take the TPC rail position as an accurate indication of its lateral position, and use the B=0 data to deduce the value of ϕ_z; (3) use some physics information like spectrum shape to deduce the trajectories corresponding to $1/p = 0$ on magnet-on runs; (4) obtain additional information from secondary scatterings of the beam; and (5) match the TPC tracks to streamer chamber tracks, where streamer chamber data is available.

Alternatives (1) is not satisfactory. There is some evidence from runs with the beam passing through the TPC that the device undergoes at least small rotations (on the order of 0.5 mr) when it is moved laterally. Alternative (2) can be used, since the position error in y_0 is at worst a few millimeters, and (3) can be used as a consistency check, but recent analyses using this procedure have lead to unacceptably large variations in ϕ_z. Alternative (5) has recently been demonstrated by the MPI Munich group to be feasible, but it is time consuming and requires a sizable data base of analyzed streamer-chamber pictures.

Therefore, we have been investigating alternative (4), analysis of B=0 runs with attention to secondary scatterers of the beam. This is done by selecting only TPC tracks that intersect the beam path at the same point (within a few millimeters) in both the x-y and the x-z planes. It is found that in addition to the the target, two other scattering centers are apparent in the data, one at S_4, the veto scintillator and one near the TPC which is probably the foil entrance to the TPC hut. We have preliminary indications that, at least for some B=0 data, there are enough tracks form these secondary scattering centers to (y_0,ϕ_z) ambiguity. This investigation is still in progress.

7.14 Monte Carlo simulations of NA49 TPC performance

H.G. Fischer* and X. Zhu

We have written a Monte Carlo program to simulate TPC response to particles produced in relativistic heavy ion experiments. In NA49 the track density is much higher than in NA35, and the cluster unfolding and track finding procedures are much more demanding. We expect this Monte carlo program to serve as a valuable tool in developing NA49 analysis software and in understanding the experimental data. The program is in working condition now and has been adapted for NA35 TPC analysis.[1]

The procedure of the simulation is as follows: as the incident ionizing particle traverses the TPC volume, it generates primary electrons which in turn produce secondary electrons. These secondary electrons drift toward the multiwire proportional chamber where the avalanches induce charge on the pad plane. For every single avalanche, the induced charge is binned into pads and folded with the electronic response of the preamp/shaper to give a time signal. The superposition of the signals from all the avalanches gives the pad signal. The pad signal is folded with electronic noise and digitized. The digitized data can be analyzed within the program, or be written to disk or tape so that it can be analyzed with more sophisticated programs. We will explain the procedure in more detail in the following sections.

The number of primary electrons produced by an ionizing particle obeys Poisson statistics. Explicitly the probability density for two primary ionizations separated by a distance s is[2] $P(s) = \exp(-s/\lambda)/\lambda$ where λ is the average distance between collisions. The interaction of an ionizing particle with gas molecules is a very complex process. For simplicity, we assume that the incident particle interacts with only one electron in the gas molecule through free Coulomb interaction and knocks out the electron only if the energy transfer E is greater than E_0, the ionization energy of the gas. This gives a $1/E^2$ energy distribution, and an angular distribution peaked near 90 degrees. The $1/E^2$ energy distribution is responsible for the Landau fluctuation. The secondary electrons are produced in a single step and are distributed uniformly along the trajectory of the primary electron. The number of secondary electrons is $N = E_{prim}/w$ where E_{prim} is the energy of the primary electron and w is the energy needed to produce one electron-positive ion pair in the gas.

In drifting the electrons toward the readout chamber, we use a three dimensional Gaussian distribution for the diffusion. The σ's of the Gaussian are proportional to the square root of the drift distance. Inside the readout chamber, the $E \times B$ effect introduces additional fluctuation in the presence of a magnetic field. This is modeled with a constant Lorentz angle. The distribution of the avalanche amplitude is assumed to be exponential.[3]

The induced charge distribution on the pad plane has been calculated by many authors under various approximations.[4] In the simulation, we use the empirical formula obtained by E. Mathieson *et al.* The pad signal is now in unit of electrons, and is converted to ADC counts using a multiplication factor which is chosen such that the most probable amplitude is 70 ADC counts, as observed in the NA35 experiment. Further fluctuation due to the electronic noise is added in

*PPE Division, CERN, 1211 Geneva 23, Switzerland.

[1]T.A. Trainor *et al., NA35 TPC Landau Fluctuation and Diffusion Analysis,* in this report.

[2]G. F. Knoll, *Radiation Detection and Measurement*, p. 96.

[3]G. F. Knoll, *Radiation Detection and Measurement*, p. 175.

[4]E. Mathieson *et al.*, Nucl. Instr. and Meth. **227** (1984) 277, and references therein.

individual time buckets. The electronic noise is modeled as a Gaussian distribution of σ=0.8 ADC counts.

7.15 NA49 beam hodoscope simulations

P. Freund* and T.A. Trainor

In order to minimize systematic errors in inclusive spectra derived from NA49 TPCs it is essential to determine precisely the relationship between the incident beam trajectory and the TPC coordinate systems on a projectile-by-projectile basis. The precision of this determination should be comparable to the precision with which tracks are determined within the TPC systems. This requires a beam hodoscope structure properly registered to each TPC coordinate system (pad plane, drift field).

It is planned to construct the NA49 beam hodoscope with four silicon strip detectors. These detectors, arranged in pairs, will measure the phase space coordinates in two planes for each incident beam particle. A test setup consisting of one detector pair was included in the spring, 1992 NA35 run. The results of this test were very promising.

There are two design questions which arise. What is the best placement of the strip detectors to obtain maximum phase space information, and how can the hodoscope systems be best registered to the TPC coordinate systems? I carried out an analysis of these problems in order to find optimum solutions.

The optimum placement problem was solved by representing the complete hodoscope in phase space and adding real beam data from a beam-in-TPC run during spring, 1992. The result of this analysis was that a good placement of the two pairs of strip detectors was 20 m and 5 m upstream from the target and that the strip pitch (250 μ) was too fine for the upstream detectors, so that wirebonding 2 or 4 strips together was preferred at that location. The downstream location was also compatible with the need to reject interactions in these silicon detectors (300 μ thick) with downstream scintillator detectors.

The problem of coordinate system registration can be solved by survey. However, in order to reduce errors, especially angle errors in the horizontal plane, to the desired level, a great deal of effort must be put forth. An alternative solution is much more convenient and can be repeated at will. This involves placing two or more targets in the beam upstream of a TPC. With the vertex magnets off all particles travel in straight lines from the beam-target intersection points. In each TPC the corresponding straight line correlations from two or more targets must intersect at the beam locations in those spaces, even though the beam does not fall within the acceptance of the TPC. The two correlations extrapolate to the effective beam location in that phase space. For each event the beam position determined by the hodoscope is compared to the beam position as inferred from the two-target correlations to complete the registration.

*MPI, Munich, Germany.

7.16 Vertex determination using the STAR SVT

P. Chan, J.G. Cramer, D.J. Prindle, T.A. Trainor, X. Zhu

The STAR experiment at RHIC will examine collisions between counter-rotating beams of heavy ions. Each beam will be bunched with a bunch length on the order of 20 cm and a transverse width a few mm. Thus the collisions will be distributed along the beam direction and for each collision we will need to measure the vertex position. We have developed an algorithm that uses space points measured by the Silicon Vertex Tracker to determine the vertex position much better than 1 mm. This algorithm is quite fast, partly because it does not rely on tracking information.

The vertex finding algorithm relies on the fact that the majority of tracks passing through the SVT have very little curvature over an arc length of 10 to 15 cm. For a particle with $p_\perp = 100$ MeV/c in a 0.5T magnetic field we expect

$$\phi(R = 15cm) - \phi(R = 5cm) = 5.1^\circ$$

If we plot SVT hits in ϕ bins of 6° most of the tracks will have all their SVT hits within one bin. Some of the tracks will be split among adjacent ϕ bins.

The second angle that defines a straight line is θ. Since calculating θ takes some time we note that

$$\frac{Z_i - Z_0}{R_i} = \frac{1}{\tan(\theta)}$$

where Z_i and R_i are the Z coordinate and radius for each hit, Z_0 is the primary vertex position of the event and θ is constant for the track. We can define a variable $\bar{Z}_i$

$$\frac{Z_i - Z0}{R_i} = \frac{\bar{Z}_i - Z0}{R_{ref}}$$

or

$$\bar{Z}_i = \frac{R_{ref}}{R_i} * Z_i + Z0 * (1 - \frac{R_{ref}}{R_i})$$

which is useful because it is a constant for the track and is fairly quick to calculate. We note that $\bar{Z}_i$ depends on Z_0. For the purposes of vertex finding the reference radius, R_{ref} should be chosen near the geometric mean radius.

The basic vertex finding algorithm is now easy to see. We make a guess at Z_0 and plot all SVT hits in appropriately sized bins of ϕ versus $\bar{Z}$. When we are nearly correct in our guess of Z_0 we find many bins containing an SVT hit from each of the three layers.

The number of triplets per 1 mm step in Z_0 for one Au-Au event is shown in Fig. 7.16. The peak near the vertex position of 8.334 cm is clearly visible above the background. We also show a close up of the region near the peak.

We have spent some time to minimize the cpu time of the vertex finder. On an HP-710 it takes about 0.75 cpu-seconds to determine the vertex position of a central Au-Au event. Since each ϕ bin is independent we can gain up to a factor of 100 by using a parallel computer. This would be fast enough that this algorithm could be used online.

The vertex finding algorithm has been tested on small samples of central Au-Au, Si-Si and p-p events. The algorithm failed on one p-p event which had a single track through the SVT and on one Au-Au event in which the primary vertex was near -23 cm. In all other events the calculated vertex was within 0.5 mm of the generated vertex.

Fig. 7.16. Number of triplets per 1 mm scan in Z_0.

7.17 Pattern recognition in the STAR SVT

H. Babcock, P. Chan, J.G. Cramer, D.J. Prindle, T.A. Trainor, X. Zhu

We have developed a pattern recognition method which is useful for finding tracks that originate at the primary vertex and pass through the STAR SVT. This algorithm uses the vertex position to group the SVT hits in ϕ versus θ. Each group is a set of points that is topologically consistent with a track.

The so called 'grouping' technique is essentially an extension of the vertex finding method presented in the previous section. The method relies on tracks being nearly straight lines over the small arc-lengths measured in the SVT allowing one to map reconstructed points onto a $\phi - \theta$ space where hits from the same track tend to group closer to each other than the typical distance between tracks.

In order to study the topology of 'correct' groups we have written a display program that produces a graphical display of Monte Carlo simulations of the SVT data. This display plots the hits in ϕ versus θ using a different color for each layer, and connecting points which the grouping algorithm decides are connected. Groups which contain an 'incorrect' hit are tagged by coloring them red. In this way we have quickly developed topology requirements that are quite efficient in finding good groups and rejecting bad ones.

The grouping algorithm has been tested on central Au-Au events generated using the Fritiof event generator and tracked through the STAR detector using GEANT. Central Au-Au events are expected to have the highest track densities of all the types of events to be studied by the STAR detector. Because of the high track densities these are the hardest events to reconstruct. In these events over 94% of the primary tracks that had three SVT hits are reconstructed correctly. For tracks with $p_\perp > 200$ MeV/c the finding efficiency is over 97%. The number of possible tracks, number of tracks found and ratio are shown as functions of $p_\perp$ in Fig. 7.17.

Fig. 7.17. Track finding efficiency with grouping technique.

7.18 Tiling the STAR SVT for increased detection efficiency

J.G. Cramer

The STAR silicon vertex tracker (SVT) is an array of silicon detectors placed near the interaction vertex of the STAR detector for tracking, precise vertex determination, detection of short-lived particles, dE/dx particle identification, and extension of momentum coverage of the STAR detector system to small transverse momentum. In its full implementation, the STAR SVT should have essentially 100% detection efficiency in its coverage region.

The detection elements of the SVT are silicon drift detectors (SDD). One of the SDD designs under consideration is the "STAR-2" configuration, which has an active region 56.2 mm wide and 70.5 mm tall. At each end of the active region is a non-detecting (dead) row of pads for charge collection. The active area of the detector is pinched in along its mid line by a triangular dead region bounding each side and containing "guard electrodes" that reduce the local potential to zero near the cut edges of the device. The resulting active region of the detector has an "hour-glass" shape bounded by dead regions on all four edges.

The geometry of the SDD creates a problem of efficiency, in that, if the devices are simply mounted end-to-end on adjacent parallel "ladders" there will be significant dead regions at the ends and edges of each SDD, leading to a detection efficiency of only about 89%. The problem of the dead areas at the ends of the SDD can be solved, as suggested by LBL engineers, by "tiling" the SDD units along the long axis of the ladder. Such longitudinal tiling is accomplished by mounting alternate SDDs on the top and bottom ladder surfaces and adjusting their positions so that the boundary of the active area of an upper detector is immediately above the equivalent boundary of the lower detector.

We have addressed the problem the triangular dead areas at the sides of the SDD by proposing an *offset lateral tiling geometry* in which two adjacent SDD ladders are offset along the longitudinal axis by half the length of an SDD (35.25 mm). With this offset, the "bulge" of one detector can be made to line up with the "waist" of the laterally adjacent detector. This strategy is not sufficient in itself, because the SVT ladders are not coplanar, and the overlapping edges must not interfere. This problem can be dealt with by arranging the ladders as a "pinwheel", so that each ladder overhangs the adjacent ladder on one side. Then, a particle travelling through the dead waist area of one SDD will also pass through the active bulge region of its neighbor, resulting in full azimuthal coverage by the SVT.

This tiling strategy will provide essentially 100% efficiency for the STAR SVT in its region of coverage. The "price" of such full coverage is that about 11% of the particles will have to pass through twice as much silicon (600 μ instead of 300 μ) in a given SVT layer. This seems an acceptable price to pay for full SVT coverage.

7.19 Estimating dE/dx in the STAR SVT with maximum likelihood analysis

J.G. Cramer and P. Chan

In the relativistic domain there are two regions where energy loss (dE/dx) may be used for particle identification: the $1/\beta^2$ region (where $p < m_0$) and the relativistic rise region (roughly $p > 2m_0$). Here, p is the momentum and m_0 is the rest mass of the particle of interest, both in energy units. Particle identification in the relativistic rise region requires very precise determination of dE/dx (around 5%) and is useful primarily in gaseous media. Here we are concerned with silicon detectors and will focus on the $1/\beta^2$ region, where dE/dx determinations on the order of 15% are sufficient.

The STAR silicon vertex tracker (SVT) consists of three layers of silicon. Consequently, there are typically three energy loss measurements. A method is needed for determining ϵ_0, the most probable energy loss, with good accuracy and without undue loss of information using only three samples. To investigate alternative schemes for achieving this goal we have performed Monte Carlo simulations, using an analytic approximation of the energy loss distribution function expected for 300 MeV/c pions passing at normal incidence through a 300 micron slab of silicon. We have generated 10^5 Monte Carlo events and examined four alternative schemes for extracting the most probable energy loss: (1) a straight arithmetic average of 3 samples, (2) taking the minimum of 3 samples; (3) averaging the lowest 2 of 3 samples; and (4) fitting the 3 samples to the expected energy loss distribution using the maximum likelihood method. Table 7.19 shows the results of this simulation. Here $< \epsilon_0 >$ is the estimate of the most probable energy loss, σ is the standard deviation of this determination, and % Dev. is the $\sigma/< \epsilon_0 >$ expressed as a percentage.

Table 1: *dE/dx Performance of 3-layer SVT*

Procedure	$< \epsilon_0 >$	σ	**% Dev.**
Average of 3	240.08	53.09	22.11
Minimum of 3	187.33	28.16	15.03
Average 2 of 3	205.92	30.83	14.97
Max Likelihood	211.64	28.84	13.63

We conclude from this study that a three layer SVT can provide dE/dx information to an accuracy of about 14%. Using a four-sigma criterion for the separation of particles, this means that the separation of electrons, pions, kaons and protons is quite feasible in the $1/\beta^2$ region of energy loss using dE/dx information from the STAR SVT combined with momentum measurements. Separation of pions from muons, however, is not feasible. As a rule of thumb, each particle type (except muons) can be distinguished from all others provided its momentum p is such that $p \leq m_0$.

7.20 STAR SVT: support apparatus and trigger system for 1993 TRIUMF test run

J. Hoffman* and T.A. Trainor

In spring, 1992 a prototype silicon drift detector (SDD) of the STAR0 configuration (1 cm x 1.5 cm) was tested with a 300 MeV/c pion beam at TRIUMF in Vancouver, B.C.[1] This was part of the R&D program for the STAR silicon vertex tracker (SVT), consisting of three layers of SDDs to provide central tracking for the STAR detector system at RHIC.

In late 1993 it is planned to continue this in-beam testing with the next generation of SDDs, the so-called STAR1 detectors (4 cm x 4 cm). The qualities of interest include uniformity of position resolution over the detector surface, tracking performance with a three-detector combination, resolution degradation with increasing nonnormal angle of incidence of the particle trajectory, dE/dx performance with small sample number and the nature of very large charge deposition events as observed in the 1992 run.

In preparation for this run a support apparatus and trigger system have been designed and the support structure and scintillator system have been fabricated at UT. The floor-mounted support structure, compatible with the beam elevation at TRIUMF, includes precision indexed motorized supports for three SDD assemblies. The central support is also rotatable about the vertical in order to test incidence angle effects. The SDDs, housed in aluminum shielding boxes (constructed at Wayne State University) along with preamp assemblies, are registered to the support structure through index marks on the exterior of the boxes.

The trigger scintillators consist of two 10 cm x 10 cm solid paddles and a 1 cm ID annulus to define the pion beam, and a 1 mm aperture in a third paddle to define a small region used to probe detector response nonuniformities over the surfaces of the detectors.

*Physics Department, University of Texas, Austin, TX.

[1]Nuclear Physics Laboratory Annual Report, 1992, p. 51.

7.21 Autocorrelation multiplicity trigger simulations

T.A. Trainor

For the heaviest A-A collisions at RHIC and LHC charged particle multiplicities at mid rapidity will be very large. The ability to trigger on topology features like jets using traditional methods will be very limited by the breakup of the jets themselves and by the presence of a soft QCD background. This means that alternative fast trigger algorithms must be developed based on detecting subtler and more general structures in the multiplicity and transverse energy distributions in order to improve substantially the physics content of the data stream at the 10–100 μs time scale.

I report here the basis for such fast algorithms: the differential autocorrelation function and associated power spectrum. A generalized 2-D autocorrelation function is calculated for multiplicity or E_t binned on (η, ϕ), and this is compared to the standard result for Poisson or other statistical distribution. The power spectrum of the resulting differential distribution is then the basis for trigger decisions. The lowest moments of the power spectrum in turn span a space within which cuts can be made to select different kinds of fluctuations or kinematic features in (η, ϕ). By this means a trigger facility is provided that can explore in a model independent **or** dependent way departures from a random particle or energy distribution. If the f_i represent multiplicity elements then the autocorrelation on a finite 1-D domain with size N and the differential autocorrelation are given by

$$B_m = \frac{1}{N-m} \sum_{i=1}^{N-m} f_i \cdot f_{i+m}$$

$$b_m = \frac{N-m}{N}(B_m - < f >^2 + \frac{\sigma^2}{N}) \qquad m \in \{1, N-1\}.$$

The example shows a multiplicity distribution with two included features, each containing 5% of the total multiplicity. The corresponding differential autocorrelation and power spectrum are also shown. The mean total power (50) for such two-feature distributions is to be compared to the mean power for the Poisson background alone (3). One can see that the total power or zeroth moment of the power spectrum provides a very selective trigger criterion for general nonPoisson structure in the distribution. Higher moments allow selection for details of the features. The autocorrelation itself permits trigger selection on specific topologies, such as back-to-back jets.

7.22 STAR conceptual design report: trigger specification

T.A. Trainor and Star collaboration*

As part of the approval process for the STAR detector system for RHIC a conceptual design report (CDR) was prepared and submitted on (sometime in April...15?), 1992. I review here the trigger system conceptual design as developed for that report by the STAR Trigger Working Group.

It was first recognized that the trigger system in a large detector system is a critical factor in determining the physics content of the produced data. In the physics programs for RHIC and LHC detectors the issues on which one might base trigger criteria are still not yet well understood, and some may not be until well into the experimental program. It is therefore important to maintain the maximum amount of flexibility in the trigger system.

In contrast, there are strong financial constraints which limit the detector subsystems which provide input to the trigger system and the degree of complexity of the system itself. The trigger design problem then is to maximize trigger performance within a particular funding profile.

The proposed STAR detector components were separated into a baseline system and upgrade subsystems. The trigger design had to be compatible with the baseline system in order to function at turn on. Within the baseline STAR detector those fast detector subsystems suitable for trigger input were 1) scintillator annuli at high η which serve to determine the collision vertex position for an event in under 100 ns, 2) a scintillator barrel array in $|\eta| < 1$ which provides a fast multiplicity distribution, and 3) TPC endcap wire chambers to continue the multiplicity distribution to $1 < |\eta| < 2$. The trigger information, until tracking information is available (10 ms), is then multiplicity near midrapidity and vertex location, known to about 4.5 cm and 150 ps.

The most important upgrades from the point of view of trigger issues were considered to be an electromagnetic calorimeter, and annular gas detectors to extend the range of multiplicity coverage beyond $\eta = 2$. The EMCAL especially would open up a broad range of trigger criteria based on correlations between multiplicity and E_t and structure in the E_t distribution.

Trigger decisions were divided into three broad areas depending on input rates and process times. The level zero or minimum bias trigger is based on a logical OR of all multiplicity elements. It is formed in 100 ns. It signals that some transport has occurred out of the beam phase space. The vertex position is added at this point to discriminate against beam-gas background and bad beam-beam events from decaying beams. The level one trigger is based on some estimate of collision geometry from the total multiplicity (or E_t, if the EMCAL is available). This is also described as a centrality trigger. It is possible with fast processors to obtain some additional information at this level about fluctuations in mean values and distributions. The level one time scale is 1 μsec. The level two trigger involves detailed calculations of distribution properties from fast trigger detectors,

*Argonne National Laboratory, Argonne, IL; Boskovic Institute, Zagreb, Croatia; Brookhaven National Laboratory, Upton, NY; University of California, Davis, CA; University of California, Los Angeles, CA; Carnegie Mellon University, Pittsburgh, PA; City College of New York, Upton, NY; Creighton University, Omaha, NE; University of Frankfurt, Frankfurt am Main, Germany; John Hopkins University, Baltimore, MD; Kent State University, Kent, OH; Lawrence Berkeley Laboratory, Berkeley, CA; University of Notre Dame, Notre Dame, IN; University of Pittsburgh, PA; Institute of High Energy, Protvino, Russia; Purdue University, West Lafayette, IN; Rice University, Houston, TX; Space Sciences Laboratory, Berkeley, CA; Texas A&M, College Station, TX; Warsaw University, Warsaw, Poland; Warsaw University of Technology, Warsaw, Poland; University of Washington, Seattle, WA; Wayne State University, Detroit, MI and Weizmann Institute of Science, Rehovot, Israel.

that is a complete extraction of information from all nontracking detectors, with a decision available in about 100 μsec. Level three trigger decisions are based on tracking detector data and are made on time scales from 10 ms up to 1 second, depending on the complexity of the algorithm.

The trigger electronics, in addition to the detector elements, were also sketched out. The principal observation was that for the STAR system, operating in connection with a storage ring, it was essential to provide pipeline storage systems for all fast detector data. It was observed that the trigger process for a stored beam is primarily a filter process on an initially periodic structure, in contrast to a process on a stochastic beam incident on a fixed target. The pipeline structure would then permit review of all beam crossings by the level zero trigger, with the minimum bias events being forwarded to derandomizing buffers for the next trigger level, and so forth.

7.23 Parallel plate avalanche detector generic research and development

T.A. Trainor and X. Zhu

We have studied the gas gain dependence on the electric field and gas pressure for isobutane and Ar/CH4 mixtures. The dimension of the Parallel Plate Avalanche Counter(PPAC) was described last year.[1] In this study, the cathode of the PPAC is illuminated with an intense uv source to produce a continuous flux of photoelectrons. The DC current at the anode is measured with a Keithley model 411 current meter. The measurement is performed at a set of gas pressures and for each pressure at several bias voltages.

The gas gain G is inferred from the anode current I as $G = I/I_0$ where I_0 is the current with unity gain as is determined from the ion saturation plateau in the gain curve. A typical gain curve is shown in Fig. 7.23 (a). The solid line is a fit as outlined below.

The gas gain is related to the first Townsend coefficient α as $G = e^n$ with $n = \alpha d$. Here n is the gas multiplication factor and d=1.25 mm is the PPAC gap. We parameterize n as $n = Ap\exp(Bp/V)$,[2] where A and B are constants depending on gas property, p is the gas pressure, and V is the bias voltage. Equivalently the above parameterization can be written as $\ln(n/p) = \ln A - B(p/V)$. In Fig. 7.23 (b), we plot $\ln(n/p)$ as a function of p/V. On this universal plot, all the measurements at different bias voltages and gas pressures should fall on a single straight line. A linear fit is performed to determine the A and B coefficients. The deviation from the straight line at low p/V is caused by the production of extra current through the field extraction of secondary electrons at the cathode.

In a separate experiment, we measured the pulse heights of alpha particles and photoelectrons as a function of the bias voltage. Fig. 7.23 (c) shows observed pulse heights compared with those predicted by the Townsend relation with our observed A and B coefficients. Of particular interest is the saturation of the alpha particles due to space charge. Some space charge saturation is also evident for the photoelectron events. This space charge is associated with individual avalanches. The event rate is much too low to build up a continuous space charge.

Fig. 7.23. Detector response curves.

[1] Nuclear Physics Laboratory Annual Report, University of Washington, p. 54 (1992).

[2] G. Brunner, Nucl. Instr. and Meth. **154** (1978) 159.

8 Cluster Impact Phenomena

8.1 Odd-even structure in atomic carbon cluster size distributions

R. Vandenbosch

In the course of our previous work on carbon cluster-impact fusion we have noted a striking odd-even effect in the yield of C_n^- clusters produced by Cs sputtering, with the yield of even-n clusters greatly enhanced over those with odd-n for $n < 10$ and odd-n clusters greatly enhanced over even-n for $n > 12$.[1] These results are displayed in Fig. 8.1-1. It is also known from other studies that the yield of C_n^+ clusters inhibits the opposite odd-even effect, particularly for n <10.[2] I present here a simple molecular orbital (MO) theory explanation for these observations. Our starting point is the generally greater stability of chains compared to rings for n <10, and of monocyclic rings over chains for larger n.[3] We consider first the molecular orbitals of straight chains. $2n + 2$ electrons go into sigma orbitals along the axis of the chain (z-axis). The remaining $2n$-2 electrons go into the degenerate π_x and π_y orbitals. The Hückel MO π_x energy levels for n =4 and n =5 are shown at the left of Fig. 8.1-2. One can see that for even n an extra electron to make the C_n^- anion can go into a lower-energy bonding orbital, whereas for odd n it has to go into a non-bonding orbital. This accounts for the favoring of even-n anions. The electron removed from the neutral cluster to make a positive ion comes from a bonding orbital for either odd or even n, and the favoring of odd C_n^+ cations reflects the greater stability of odd-n neutrals.

Now consider the molecular orbitals for monocyclic rings. We assume there are $2n$ electrons in the sigma orbitals along the ring (taken to lie in the yz plane). We neglect ring strain and assume that the π_x and π_{yz} orbitals are degenerate. (Our conclusions will not be altered if the π_x and π_{yz} orbitals are displaced with respect to each other due to deviations from colinearity of the π_{yz} orbital axes). The energy levels of the π_x orbitals from Hückel MO theory are shown at the right of Fig. 8.1-2. There are n electrons each to go into the π_x and π_{yz} orbitals. One can see that one must add an electron to a non-bonding orbital to make the C_{16}^- anion, whereas the C_{17}^- anion can be made by adding an electron to a bonding orbital. Similarly for C_{14}^- the extra electron has to go into a more antibonding orbital than does the extra electron in C_{15}^-. These effects lead to a striking odd-even effect in the measured electron affinities,[3] and to the odd-n anions having 30–40 times more yield than the even-n anions as shown in Fig. 8.1-1.

An easy although slightly oversimplified way to understand the shift in anion stability from even to odd when going from chains to rings is to realize that two non-bonding electrons on one end of a chain are available to put into the π orbitals when one closes the chain into a ring. One each goes into the π_x and π_{yz} orbitals, leading to a shift instability from even to odd.

[1] R. Vandenbosch, D. Ye, J. Neubauer, D.I. Will, and T. Trainor, Phys. Rev. A **46** 5741 (1992).
[2] W. Weltner, Jr. and R. J. Van Zee, Chem. Rev. 89, 1713, (1989).
[3] S. Yang, K.J. Taylor, M.J. Craycraft, J. Conceicao, C.L. Pettiette, O. Cheshnovsky, and R. E. Smalley, Chem. Phys. Lett. 144, 431 (1988).

Fig. 8.1-1. Carbon cluster anion size distributions obtained by Cs ion bombardment of graphite.

Fig. 8.1-2. Schematic molecular orbital energies for chains (a) and rings (b). The arrows indicate the occupancy for neutral Cn clusters.

8.2 Cluster size distributions for Cs impact of C, Al, Si, and Cu

R. Vandenbosch and D.I. Will

We have previously noted a striking pattern of odd-even variations of cluster intensity in our study of cluster impact fusion of carbon clusters. The preceding contribution in this Report discusses this distribution from the point of view of molecular orbital theory. Motivated by the interesting structure in the cluster size distribution for carbon, we have studied several other elements.

The element most chemically similar to carbon is silicon. The cluster size distribution for silicon however was found to fall very rapidly and monotonically, as is illustrated in the figure. The next element which we investigated was aluminium. This element was chosen because of a recent report[1] that a 13-atom cluster with icosohedral symmetry would be particularly stable. Indeed we see a peak in the aluminium size distribution at n=13. A peak at n=13 has been seen in Xe cluster distributions, as well as other peaks at 55 and 147 which coincide with the number of spheres for complete-shell iscosahedral packing.[2] In Al there may however be another explanation for this peak. Aluminium has 3 valence electrons, so that a 13 atom cluster anion will have 13 x 3 + 1 = 40 electrons. This is a magic number for a spherical potential well and has been shown to give rise to a peak in the cluster size distribution for alkali metals.

The authors[1] who predicted special stability for n=13 for Al also reported that a cluster with a carbon atom substituted for the central aluminium atom would also be especially stable. We therefore tried to make such a cluster by sputtering both heterogeneous mixtures of aluminium and graphite, and also by sputtering aluminium carbide (Al_4C_3). No evidence for an $Al_{12}C$ cluster was obtained.

We have also studied nickel and copper. The nickel results are preliminary (and not reported here) as normal isotopic nickel was used. The copper study employed enriched ^{63}Cu. The results for nickel are similar to copper in overall falloff but do not exhibit as obvious odd-even structure. The odd-even structure for copper is interesting, and will be pursued.

Fig. 8.2-1. Cluster size distributions for anions of several elements produced by Cs ion sputtering.

[1] S.N. Khanna and P. Jena, Phys. Rev. Lett. 69, 1664 (1992).
[2] O. Echt, K. Sattler, and E. Recknagel, Phys. Rev. Lett. 47, 1121 (1981).

9 External Users

9.1 Radiation effects on opto-electronic devices

G.A. Geissinger* and E.W. Smith*

Experiments were performed to permit an analysis of opto-electronic devices in a hostile radiation environment. The analysis is being used to improve the performance of new circuit designs. The Van de Graaff accelerator at the University of Washington was able to provide a variety of particle types and a wide range on energies so that the effect of both high energy primary particles and fast secondaries could be studied independently.

Monoenergetic particle beams were used over a range of different energies in order to study the influence of specific reaction cross sections. With these basic data, it is possible to model the response of various device designs to a broad energy spectrum. This permits a determination of the device response to the wide range of reactions channels that are encountered in different radiation environments. Minor, inexpensive design modifications may then be incorporated in order to optimize the performance of a specific device for use in high or low altitude space craft orbits, or for operation within a nuclear reactor.

9.2 Summary of single event effects testing by BPSRC

J.D. Ness,† E. Normand,† D.L. Oberg† and J.L. Wert†

Boeing personnel have continued heavy ion testing of selected semiconductor devices in support of Boeing and NASA programs. These investigations are of single event effects on microelectronics as may be seen in high altitude or space environments. Previous testing[1] was done with a simple test chamber attached to the NPL 60-inch scattering chamber. Only lower energy ions from the tandem Van de Graaff have been used in the past. Of these ions, only the masses below fluorine (and, depending on the device, chlorine) have sufficient range to acceptably simulate the radiation in the natural environment. A minimum range of 40 μm in silicon is required by NASA. This year we have started using the superconducting linac booster to provide higher energy (260–300 MeV) nickel ions for testing as they have the required range and are representative of the heaviest mass cosmic rays seen in space. NASA is requiring that all testing of power MOSFETs be done with such energy and mass ions. (An improved technique for testing power devices was previously discovered by us at the NPL.[2])

BPSRC (Boeing Physical Science Research Center) personnel have developed a new dual chamber test system for the NASA Space Station Freedom program. It is depicted in Fig. 9.2. The beam is scattered from gold foils in the center chamber and devices under test can be positioned and rotated in either or both of the side chambers. This allows two independent tests to be carried

*Ball Aerospace Systems Group, Electro-optics and Cryogenics Division, Boulder Industrial Park, Boulder, CO 80302.

†Boeing Defense and Space Group, P.O. Box 3999, MS 2T-50, Seattle, WA 98124.

[1] Nuclear Physics Laboratory Annual Report, University of Washington (1992) p. 65.

[2] D.L. Oberg and J.L. Wert, *IEEE Trans. Nuc. Sci.*, **NS-34**, 1736 (1987).

out simultaneously. In addition, several devices can be exposed to the scattered beam at the same time. These options allow for very efficient testing.

Several papers have been submitted to the IEEE Natural and Space Radiation Effects Conference this year. These represent work done by Boeing partially at the University of Washington Nuclear Physics Laboratory.

Fig. 9.2. NASA/Boeing dual single event effects test chamber.

9.3 Production of radionuclides by ^{3}He irradiation of carbon and oxygen

B. Jardine* and W.G. Weitkamp

The isotopes ^{11}C, ^{13}N, ^{15}O and ^{18}F have important uses in medicine, especially in positron emission tomography (PET), but because of their short half lives they must be produced at the site at which they are to be used. A collaboration of scientists from the University of Washington Department of Radiology and Science Applications International Corp. has been developing a radiofrequency quadrupole accelerator compact enough to produce PET isotopes in a hospital. This accelerator produces a 7 MeV ^{3}He beam and uses carbon and oxygen targets.

The most suitable target configuration for this system consists of thin foils of carbon or an oxide surrounded by He gas. Radionuclides recoiling into the gas are recovered quickly by pumping the gas into a fast chemical processing system. Last year we made a crude numerical model of such a target and tried adjusting foil and gas thickness to maximize isotope production.[1] However, it was realized that there was not adequate cross section data to make such an adjustment reliable. Both total reaction cross sections and differential cross sections for reactions to the excited states of the nucleus produced are needed to optimize the target design.

There is a good measurement of the total reaction cross section for the ^{12}C(^{3}He,α)^{11}C reaction and several sets of measurements of the differential cross section to the ground state of ^{11}C. In regions of overlap the various measurements[2,3] differ by about 40%. There are very few measurements of differential cross sections to the excited states of ^{11}C and few measurements of cross sections for the ^{12}C(^{3}He,d)^{13}N reaction.

For the ^{16}O(^{3}He,p)^{18}F reaction, available total cross section measurements have large uncertainties and differ by a factor of 2.[4,5] There are few measurements of the total cross section for the ^{16}O(^{3}He,α)^{15}O reaction. There are measurements of differential cross sections to the ground states of both ^{18}F and ^{15}O but few measurements of differential cross sections to excited states of either nucleus.

We have measured a sample of the required differential cross sections including those for the ^{12}C(^{3}He,α)^{11}C reaction at several energies from 3.5 to 7 MeV using carbon foil targets and conventional Si detector telescopes. Alpha particles from reactions to excited states up to 4.8 MeV can be readily identified and measured. However, the most important differential cross sections at forward angles are obscured by ^{3}He beam particles in the Si detectors. It should be possible to make clean measurements at forward angles using the Laboratory magnetic spectrometer.

Measurements of the ^{16}O(^{3}He,p)^{18}F and ^{16}O(^{3}He,α)^{15}O reactions were made at angles from 45° to 135° and energies from 4.4 to 6.9 MeV using a gas cell containing 100 mm of O_2 and solid state detector telescopes. Excited states of ^{18}F up to 3.36 MeV can be readily identified and measured although not all the states can be completely resolved. Again the important forward

*Physics Department, University of Washington, Seattle, WA 98195.

[1] Nuclear Physics Laboratory Annual Report, University of Washington (1992) p. 67 and 69.

[2] R.S. Blake *et al.*, Nucl. Phys. **77**, 254 (1966).

[3] H.-M. Kuan, T.W. Bonner and J.R. Risser, Nucl. Phys. **51**, 481 (1964).

[4] S. Gorodetzky *et al.*, Nucl. Instrum. and Meth. **42**, 269 (1966).

[5] J. Gass and H.H. Müller, Nucl. Instrum. and Meth. **136**, 559 (1976).

angle differential cross sections must be measured with the magnetic spectrograph.

A more detailed report on these measurements is in preparation.

10 Instrumentation

10.1 Background study for detection of atomic electrons in coincidence with nuclear scattering.

J.F. Amsbaugh, J. Beck, C.E. Hyde-Wright and W. Jiang

We would like to measure atomic electrons in coincidence with α-helium nuclear scattering near 90 degrees in the CM and at 30–40 MeV bombarding energy. The time of flight and angular distributions of the electrons would be measured in coincidence with the scattered α. This is an interesting 3-body system consisting of two electrons in the time-dependent (classical) field of the two α-particles. The beam energy and scattering angle are chosen to insure that the projectile and recoil velocities are much greater than typical atomic electron velocities.

He$(\alpha, \alpha' e)e\alpha$ and He$(\alpha, \alpha' ee)\alpha$ true coincidence events must be detected in the presence of a background of α singles in accidental coincidence with atomic ionization electrons. The (α, α) cross section is approximately $1b$.[1] The ionization cross section is $\geq 10^7 b$.[2] We have modified the linac's Time Structure Monitor (TSM)to study the production and collection of ionization electrons. We were particularly concerned about possible backgrounds from ionization electrons bouncing long distances along the beam pipe.

A sketch of our apparatus is shown in Fig. 10.1-1. An inner cylinder is elevated to -2400 V. This cylinder has two 0.5"ϕ apertures for the beam. Ionization electrons from the gas in the inner region drift ballistically in the inner field-free region. The inner cylinder is surrounded by a shielding block at -2000 V. This block has beam ports 0.36"ϕ. Electrons are collected at the cathode of a two-stage chevron Micro-Channel-Plate detector (MCP). The electrons are first accelerated across a gap and then partially decelerated to the cathode potential of -2000 V. The acceleration fields are shaped by wire arrays across the 0.9" apertures. This field configuration was chosen to suppress ionization electrons from outside the inner region and to suppress the collection of secondaries from the shielding block. The beam is collimated by a 0.25"ϕ Ta aperture 23 cm upstream. Secondary electrons from the aperture are swept out of the beam by a chicane consisting of two permanent U-magnets forming two 1 cm gaps each with equal and opposite integrated field strength of ≈ 500 G-cm. Although the manufacturer[3] would not vouch for the performance of the MCP at pressure greater than 10^{-6} Torr, we found no degradation of performance after several hours of operation at absolute He pressures $\leq 10^{-4}$ Torr

For convenience, we used a 0.30 nA beam of 52.5 MeV $^{16}O^{6+}$ for our tests. The beam is chopped on the ion source deck to select only one bunch in 100 at the 12.5 MHz buncher at the low energy end of the tandem. After extensive tuning to minimize beam scraping at the Ta aperture, we obtained the MCP time spectra shown in Fig. 10.1-2. Drift time increases to the left, with 0.243 ns per channel. The lower and upper curves are for absolute He pressures of 3×10^{-7} Torr and 1.3×10^{-5} Torr, respectively. The vertical scale is counts per 100 nC (electrical) corrected for acquisition deadtime. The result is approximately 1 count per unit.

[1] H.E. Conzett *et al.*, Phys Rev **117** 1075 (1960).
[2] F. Sauli, "Principles of Operation of Multiwire Proportional and Drift Chambers" CERN 77-09.
[3] Galileo Electro-Optics, P.O. Box 550 Sturbridge MA 01566.

We believe the narrow peak at ≈chan 1300 is due to direct collection of ionization electrons. The broad peak from chan. 1200–1250 is due to electrons making one or more bounces on the inner cylinder. The yield in this region at low pressure is due in part to beam halo scraping on the downstream aperture of the the shielding cylinder. The bump around chan. 1100 is correlated with the Faraday cup, 40 cm downstream of our apparatus. The long tail at late times is a combination of very slow electrons and the time structure of our beam. We are presently designing an improved test apparatus in which the HV surfaces are replaced with wire arrays.

10.2 Gamma-ray Multiplicity Detection Array

Z.M. Drebi, M.S. Kaplan, M. Kelly, K.A. Snover, D.P. Wells and D. Ye

Construction of a γ-ray multiplicity detection array consisting of 23 NaI elements is nearly completed. Each individual element is a 3 inch $\times$ 4 inch cylindrical NaI detector with the front surface facing the center of the array. The center to front surface distance is 6 inches for all elements. This array is designed for use in conjunction with the existing 10 inch $\times$ 15 inch NaI detector or the three Compton-suppressed Ge or BaF_2 detectors.

This instrument can provide measurements in the following quantities.

1. multiplicity – related to the angular momentum;
2. angular distribution of γ-rays (from the hit pattern of detectors) – related to spin orientation and γ-ray multipolarity;
3. time distribution of γ-emission – for identifying or tagging formation of isomers.

Since all these quantities are measured on an event-by-event basis, it is possible to set gates on parameters to select or filter a specified class of events.

The mechanical configuration of the array provides each element with identical solid-angle coverage which makes the multiplicity response function easy to estimate. The array has a total detection probability of 23% for a 1 MeV γ ray. For events of 20 γ rays of 1 MeV, the measured multiplicity distribution is calculated to peak at $M_\gamma = 4$ with a $FWHM = 3.98$. A spherical gap of 12 inch diameter at the center of the array offers sufficient space to accommodate some elaborate target systems.

Due to the small cross section for high-energy γ-ray production, experiments measuring high-energy γ-ray spectra with the 10 inch$\times$ 15 inch NaI detector require the individual element in the multiplicity array to sustain a high count rate up to 200 KHz. Special measures are taken to achieve this.

1. Low voltage is applied to photomultipliers to reduce the tube current.
2. A passive RL shaping circuit is added immediately after the photomultiplier to shorten the decay time to within 250 ns to reduce pileup.
3. To retain the output pulse amplitude, two Philips 776 fix-gain ($\times$10) amplifiers are used for each detector.

This setup results in a timing resolution of 2.1 ns for 1.3 MeV γ rays from ^{60}Co. All analog signal related electronics are placed in the experimental area near the detector setup. Only the logical timing signal of each element is sent to the acquisition system to be converted into digital format and recorded.

11 Van de Graaff, Superconducting Booster and Ion Sources

11.1 Van de Graaff accelerator operations and development

C.E. Linder, D.W. Storm and W.G. Weitkamp

Last year we reported difficulty with the charging belt dumping charge onto the column when the charging current exceeded a critical value.[1] This problem appears to have been solved. We redesigned the insulator on the inner belt guide, using an 8 mm diameter pyrex glass rod. This gives about a 60% increase in insulating surface. We have replaced 75% of the insulated inner belt guides on the side of the column on which the upcharge travels. The belt is set so it moves toward the inner belt belt guides above the critical upcharge current. There have been no reported episodes of charge dumping onto the column since the new guides were installed.

The major maintenance problem during the year, which led to the longest continuous shut down of the accelerator (30 days) since it was turned on in 1965, was the failure of a water chiller. Water from this unit cools the tandem drive motor, the ion sources and the tandem vault. The chiller has been in operation since 1963 and has been overhauled a number of times, but this failure was not curable by a simple overhaul. After several delays, a temporary unit was brought on line and replaced several weeks later by a permanent unit. The new unit has a number of advantages over the old unit; among other things it has a digital trouble shooting system and dual compressors so it can be overhauled without shutting down the entire system. It is also operates much more quietly.

A second major loss of beam time occurred because of problems with the charging belt. A belt installed in August 1992 developed 4 vertical cracks after less than 1000 hours of operation and had to be removed. The only plausible explanation of the cause of these cracks appears to be that the belt material was somehow improperly cured.

From time to time we have had trouble with the sparking in the circuitry of the 6BK4B beam triode tube which controls the corona current. Previously[2] the cathode bias on this tube was increased to from 6.5 to 10 V. However, this setting requires a plate voltage of 15 kV to maintain 50 μA of corona current. By reducing the bias back to 6.5 V *and* reducing the dynamic range of the control circuit from ± 8 V to $\pm$ 5 V, we have reduced the plate voltage corresponding to 50 μA to 11 kV and we still avoid biasing the grid positive with respect to the cathode.

We have continued to install new resistors in the tandem; at present we have replaced all but 96 of the 368 full-value resistors. Our resistor assembly consists of 4 Kobra[3] resistors in a PVC tube. Since most of the new resistors have been in place for more than 6 months, we have some data on the stability of these resistors. We find that the resistors decrease in value at a rate of 4.8%/year, and that the standard deviation of the spread in values increases 3.6%/year. To minimize this drift in resistance value, we are currently investigating the installation of shielded resistors. Prototypes shields using the Florida State design[4] have been completed and test resistors ordered. We plan to test 3 different types of resistors in the accelerator.

[1] Nuclear Physics Laboratory Annual Report, University of Washington, p. 86 (1992).
[2] Nuclear Physics Laboratory Annual Report, University of Washington, p. 73 (1991).
[3] K&M Electronics, West Springfield MA 01089.
[4] K.R. Chapman, *Symposium of North Eastern Accelerator Personnel,* Kansas State University, 1990, (World Scientific, T.N. Tipping and R.D. Krause, eds., 1991,) p. 175.

During the year from March 1, 1992 to February 28, 1993 the tandem operated 3773 hours. Additional statistics of accelerator operations are given in Table 11.1.

Table 11.1
Tandem Accelerator Operations
March 1, 1992 to February 29, 1993

Activity	*Days Scheduled*	*Percent*
A. Nuclear Physics Research, Ion Sources Alone	6	2
B. Nuclear Physics Research, Tandem Alone		
Light Ions	39	11
Heavy Ions	26	7
Accelerator Mass Spectrometry	33	9
Subtotal	98	27
C. Nuclear Physics Research, Booster and Tandem Coupled		
Light Ions	17	5
Heavy Ions	31	8
Subtotal	48	13
D. Outside Users		
Ball Aerospace Systems Group	2	<1
Boeing Company, Tandem Alone	5	1
Boeing Company, Tandem and Booster Coupled	4	1
Subtotal	11	3
E. Other Operations		
Tandem Development	24	6
Tandem Maintenance	113	31
Unscheduled Time	65	18
Subtotal	202	55
Total	365	100

11.2 A proposal to upgrade the tandem accelerator

D.W. Storm and W.G. Weitkamp

The University of Washington Model FN Tandem Accelerator has been in operation since 1965; for 27 years it has done a reasonably satisfactory job of filling the needs of the Laboratory without major modification. However, developments in the technology of charging systems and beam tubes and problems with maintenance have induced us to propose an upgrade to this accelerator.

We would like to install a pelletron charging system and a set of spiral inclined field beam tubes in this machine. We expect this upgrade will accomplish the following: improve the stability of the beam in position, energy, intensity and transit time through the accelerator; improve the transmission of beams through the machine, especially at low energies and for heavy ions; increase the energy of beams which can be run; increase the range of nuclear species which can be run through the booster and improve reliability of the accelerator.

In preparing this proposal, we have drawn on the extensive experience of the 10 other North American labs which have upgraded EN or FN tandems to pelletron charging systems, spiral tubes or both in recent years. All 10 labs have reported excellent success with these upgrades.

We expect the pelletron charging system to be a superior system to our existing belt charging system. We are currently experiencing several problems with our belt system which should be solved by installing a pelletron. First, irregularities in the charging current on the belt couple to the inclined field tubes to induce a pronounced vertical motion on the beam as it exits the tandem. We have been able to reduce but not eliminate this "vertical jitter" by replacing the charging screens with thin metal charging electrodes.[1] Second, the belt produces dust which can induce terminal sparking and insulator breakdown.

Users of pelletron charging systems report no evidence of vertical jitter and minimal fluctuation in terminal potential because charge is deposited on the pellet chains by induction, a process insensitive to surface irregularities, which are a common problem with belts. And, pelletrons run completely dust free and need be replaced only once in every 5-7 years instead of annually. It takes only one day to replace a chain; replacing a belt takes about two weeks.

There are three difficulties with our present vertical inclined field beam tubes which should be reduced by the installation of spiral inclined field beam tubes. First, our present tubes have been in the machine for nearly 60,000 hours and are showing signs of damage, limiting high voltage performance. Second, the transmission of beams through the machine is poor for very low energy beams and for heavy ions. And third, vertical inclined field tubes couple strongly to variation in charging current, as mentioned above, inducing vertical jitter on the beam and in some cases, intensity fluctuations as well.

Spiral beam tubes have demonstrated superior transmission, especially at low energies and for heavy ions because of improved beam optics and residual gas pumping and have a proven record of stable operation, showing no signs of coupling to charging current irregularities.

[1] T.A. Trainor, *Symposium of North Eastern Accelerator Personnel*, Kansas State University, Oct. 24–26, 1990, (World Scientific, T.N. Tipping and R.D. Krause, eds., 1991) p. 58.

In order to install a pelletron in our tandem, two modifications must be made: first, the present 400 MΩ resistors must be replaced with 800 MΩ resistors. As mentioned in Section 11.1 of this report, we have begun a program to upgrade the resistor housings. Second, lucite rods which control terminal functions must be moved. This presents no significant problem; work will begin when the pelletron is ordered.

A proposal for funding this upgrade was submitted to the D.O.E. and has recently been funded.

11.3 Booster operations

D.T. Corcoran, G.C. Harper, M.A. Howe, D.W. Storm, D.I. Will and J.A. Wootress

During the March 1, 1992 to Feb 29, 1993, the booster was operated for 48 days, as compared to 71 days in the same period a year earlier. Beams ranged in mass from ^{4}He to ^{64}Ni, with emphasis on ^{4}He.

No particular improvement was made in the fields at which the resonators operate, but no degradation was noted either. We have generally been able to operate 37 or 38 of the 39 resonators (including buncher and rebuncher) routinely. One had a stuck coupler and another had a damaged rf feedthrough. The feedthrough has been replaced and at the end of February all but one resonator was operable.

The rebuncher was used to provide optimum energy resolution during a ^{4}He run, where the excitation function and angular distribution for $^{4}\text{He} + {}^{4}\text{He} \rightarrow {}^{8}\text{Be} + \gamma$ was measured. Resolution of better than 30 KeV (0.1%) was obtained.

We have again not had to replace any more compressors. The strategy of running the compressors unloaded instead of shutting them down and of starting with the full line voltage continues to be successful in extending the lifetime significantly. One compressor has run 55k hours and another 53k hours.

11.4 Cryogenic operations

M.A. Howe, D.I. Will, and J.A. Wootress

The booster linac is cooled by liquid helium which is thermally shielded by liquid nitrogen. The liquid nitrogen is delivered in lots of ~6000 gallons by semitrailer tanker. In 1992 liquid nitrogen consumption was similar to 1991 at 231,000 gallons. [1] The helium is purchased as high purity bulk gas and liquified by our helium refrigerator. Usage of 169,300 SCF in 1992 was up 47% from that in 1991 due to several significant leaks (all but one of which have since been eliminated.) The leak which remains appears to be in one or both aluminum plate-fin heat exchangers providing liquid and vapor nitrogen precool for the helium.

Due to difficulties sealing charcoal bed inlet and outlet valves while baking, pumping and purging the beds, stems of twelve extended-stem valves on our helium refrigerator were pulled. The stem extensions consisted of stainless steel (SS) tubing spotwelded to SS end caps. Spotwelds had broken or cracked on four stems so all twelve were reinforced with circumferential TIG welds, and four spares were built. The following table summarizes our maintenance for 1992 January 1 to 1992 December 31:

[1] Nuclear Physics Laboratory Annual Report, University of Washington (1992) p. 84.

Item	In Use	Major Services	Times Performed
Refrigerator			
Cold Box	98%	warm/pump/purge	3
Main Dewar	100%	warm/pump/purge	0
Top Expander	~6371 Hrs	warm/pump/purge	20
	~100 RPM	main, valve rod and valve seals	1
		wristpin, crank, and cam follower brngs	1
		flywheel bearings and belts	1
Middle Expander	~8078 Hrs	warm/pump/purge	18
	~120 RPM	main, valve rod and valve seals	1
		wristpin, crank, and cam follower brngs	1
		flywheel bearings and belts	1
		replaced both cross-heads	1
		replaced one cross-head guide	1
Wet Expander	~4612 Hrs	warm/pump/purge	6
	~40 RPM	main, valve rod and valve seals	1
		wristpin, crank, and cam follower brngs	1
		flywheel bearings	1
		replaced one cross-head guide	1
Screw Compressors			
RS-1	54,882 Hrs	total/running	
	5412 Hrs	1992/replaced charcoal and oil	1
RS-2	52,549 Hrs	total/running	
	8228 Hrs	1992/replaced charcoal and oil	0
RS-3a	23,336 Hrs	total/running	
	8027 Hrs	1992/replaced charcoal and oil	1
Distribution System	99%	warm/pump/purge lines	6

11.5 An object-oriented programmable controller

C.E. Linder and M.A. Howe

One of the lab controllers (a 20 year old Texas Instruments 5TI-1000 Sequencer) has been replaced with a 80386 PC running an object-oriented control program written in C++. This new controller, which has become known as the GORDO, has the job of controlling the tandem vacuum system, the low energy buncher interlocks, the faraday cup interlocks, some of the radiation safety system, and the AMS data collection cycling. The GORDO is configured to use up to 240 I/O modules of which 160 are optically isolated inputs and 80 are solid state relay outputs. Depending on the type of module used, I/O can be either 120V AC or 5V DC.

The GORDO user interface is designed to mimic the typical modern graphical user interface. By using pull down menus the user can select, place, and connect the various switches, logic gates, and output relays that are needed to implement a particular ladder or logic diagram. Input switches are assigned I/O bit numbers that correspond to a particular input module and output devices are assigned to solid state relay modules. Logic diagrams become active as soon as they are connected to output relays. Multiple display pages are used to organize diagrams according to function or location. Since devices and connections change color and appearance (i.e. the switches are drawn open or closed) determining the state of a logic circuit becomes the fast, easy inspection of a picture on the PC screen.

Lay out and editing tools are also available to change any logic diagram in real-time without interrupting the control functions of other logic diagrams. For example, a new input switch can be spliced into a diagram to augment an interlock without shutting down whatever is being controlled by that logic diagram. The new switch becomes active immediately.

Virtual control relays (special output devices which are not connected to the real world) are used to pass signals from page to page and also to provide a feedback mechanism. CSX bits (virtual switches not connected to input modules) are also available to provide software remote control. The controller is connected to the linac control system via a 9600 baud RS-232 serial line. It is the 14th satellite of CSX. See Section 11.6 for a discussion of how information from the GORDO is used in CSX.

Diagrams are self documenting thru the use of text and clear layout design. If hardcopies are needed, any or all pages can be converted to postscript and sent automatically to the apple laser writer. Hardcopies can also be made from CSX or loaded onto a floppy for transport to another PC. Pages are documented via titles that can be put on each page. The system collects and places titles in an index page that allows the user quick access to any page. There are also input, output, control relay, and CSX bit index pages that allow particular I/O devices to be found easily.

The GORDO controller has proven to be very robust during power glitches. It has continued to run during the type of glitches that cause most of the other computers in the lab to crash. After major power interruptions the the GORDO will reboot and start the last saved control program automatically.

In the near future, the 5TI sequencer in cave 1 will be replaced with an identical PC based controller and will presumably be called the GORDO II.

11.6 Improvements to the linac control system

M.A. Howe

The domain of Linac Control System (CSX) was extended to the tandem this year by replacing the tandem 5TI sequencer with the GORDO controller (see section 11.5). Because the GORDO is connected to CSX via a 9600 baud RS-232 serial line, all of the tandem vacuum system, the interlocks for the tandem faraday cups, the low energy buncher interlocks, and some of the radiation safety system information is available to CSX for display and in some cases for control. The Gordo is the 14th satellite of CSX.

A CSX display page was developed to display the ladder diagrams that the GORDO uses internally. When this page is first called up, an index page of buttons appears–one button for each of the ladder diagram pages that GORDO can display. Touching one these page buttons tells the GORDO to do a remote draw of that ladder diagram onto the CSX touch screen. Touching the screen again will redisplay the index page. Any of the GORDO ladder diagrams can be captured for hard copy on the apple laser writer.

Another new CSX page displays the tandem vacuum status. The GORDO provides the information about the tandem beamline which CSX organizes into a picture that clearly shows the on/off, open/closed, good/bad status of the pumps, gatevalves, and pressures in the beamline. Checking the status of the beamline becomes a quick glance at this page.

The low energy buncher interlock information from the GORDO has been integrated into the CSX LE buncher display page. The buncher on/off status is used to control the buncher console LED which was previously always on and only showed the lock/unlock status of the buncher. Also the water flow interlock is displayed.

The linac CUPS page has been expanded to show the state of the LE and HE faraday cups.

The LINAC page now shows the status of the radiation doors leading to the tunnel, the tandem radiation barriers, and the gamma and neutron high radiation monitor trips. Other radiation safety system information will be displayed as it becomes available when the cave 5TI is replaced.

The SHOW command has been expanded to show the complete status of the linac pumping stations. This is very useful for people trying to monitor or recover the vacuum system at night from remote sites (i.e. home).

The cryo satellite stepper motor interface was finished and a stepper motor installed on the pressure building valve for the dewar. The linac He DEWAR page was modified to provide control of this valve.

11.7 Tandem terminal ion source

L. DeBraeckeleer, G.C. Harper, D.W. Storm, K.B. Swartz and W.G. Weitkamp

The mass-8 beta-decay experiment will eventually require a beam of 3-Mev ^{3}He. The necessary machine time estimated for this part of the experiment using the existing alpha source is several months. In order to reduce this time, a study has been initiated this year to determine the possibility of installing an ion source capable of producing high intensity beams of $^3He^+$ and $^4He^+$ in the terminal of the Van de Graaff.

In the configuration anticipated for the experiment, the foil changer in the Van de Graaff terminal would be removed from its port, which is 60° off of the beam axis, and in its place an RF discharge source would be installed. The beam from the ion source would be deflected through 60° back onto the Van de Graaff beam axis by a permanent magnet or an electromagnet assembly. Optical matching to the beam tube would be provided by an einzel lens expected to be located between the source and the deflection magnet.

Ion sources of this variety are specified to deliver 400 μamps of $^1H^+$ and 200 μamps of $^4He^+$ with expected output current inversely proportional to $\sqrt{m}$ where m is the mass of the ion in AMU. The gas load produced is of the order of 1 to 2 mTorr-l/sec. We expect to use an extraction voltage of 10 kV to 50 kV.

The technical problems that are presently being studied are beam transport, He gas pumping, and the Van de Graaff terminal AC power budget. Beam transmission problems encountered involve transporting a low energy beam through a small deflection magnet into the strong lens produced by the high energy beam tube and the inherent steering of an inclined field tube. The pumping system must remove a large load of helium gas from the terminal in a way that maintains an acceptable ion beam transport in an environment that has the potential to be highly collisional. Finally, there is the possibility that the power available in the terminal after an upgrade to a pelletron charging system will be large enough only to fill the power requirements of the RF discharge source and its associated power supplies. In that case alternatives to such luxuries as a terminal pumping scheme and an electromagnetic deflection system must be explored.

11.8 Tandem belt charge current monitor

G.C. Harper and C.E. Linder

A device has been developed which permits direct measurement of the tandem belt charging current. This is a diagnostic which can remain permanently installed without interfering with normal operation and immediately indicate irregularities in the distribution of charge on the belt. This measurement has the potential to flag "dead" spots on the belt or interruptions of the contact between the belt and the charging screen.

The belt charging circuit consists of a high voltage shunt regulator tube using a DC power supply of about 25 kV. This is connected in series with a constant current source whose plate voltage provides feedback to the cathode of the shunt regulator. The constant current supply directly feeds the charging screen through a high voltage coaxial cable. In this manner, the charging screen is maintained several kilovolts above ground and the screen voltage is adjusted to maintain a constant flow of charge onto the belt. Sometime in the past, a probe was built to measure the voltage between the screen and ground. This measurement revealed variations of the screen voltage which indicated that the constant current source was active but this alone did not prove that the regulator was actually working correctly. Direct measurement of the instantaneous time variation of the current was made difficult by the high potential of the screen which is the point at which this current must be measured.

A quick search of vendors was made for an optocoupler able to make analog current measurements of this nature while withstanding 30 kVDC of potential difference, but none was found which could supply such a device. We developed an optocoupler using an inexpensive, matched pair of infrared devices that we had on hand and a short rod of PVC plastic drilled to accommodate and align the optoelectronic components. The tube was filled with dry Argon at one atmosphere and the infrared LED and phototransistor were glued into the ends with epoxy. Small caps of PVC were attached to the ends of the tube to hold transient suppression networks and provide strain relief for the connecting wires. These caps were filled with RTV sealant to exclude insulating oil from the assembly when submerged. The optocoupler was hi-pot tested to 40 kVDC in air.

The LED used, a TIL-31 by Texas Instruments, is not intended to operate at the low DC currents characteristic of the belt charge system. At a nominal belt charge current of 200 μamp, the current gain of the optocoupler is about 0.01 and the -3 dB rolloff point is at about 50 Hz. The nonlinear response makes it necessary to use a transfer curve generated for the optocoupler to determine the DC component of the belt charge current from which the small, quasilinear AC component can be scaled.

Measurements using this device on the presently installed belt have shown that it can accurately reproduce the DC component of the belt charge current. At 200 μamp DC the AC component of the charge current measures about 20 μamp rms. The current is shown to flow continuously with no spikes or interruptions. Measuring the output signal with an audio frequency spectrum analyzer reveals frequency components all of which are integral multiples of the belt fundemantal frequency of 2.4 Hz. Relatively large components evident at 12 and 14 times the belt frequency presumably are due to the cure pattern observed to be physically present on the belt.

11.9 Injector Deck and Ion Sources

G.C. Harper and D.I. Will

The 300 kV isolation transformer continued to operate without incident all year. Lab policy now is that injector deck operating voltages from 0 to 240 kV are considered to be standard. Authorization must be received to operate the injector deck at voltages above 240 kV. The steel hardware used on the tank flanges has been replaced with fiberglass nuts and threaded rods which seems to have eliminated the corona problem on the outer surfaces of the tanks.

A new set of XY steerers has been built for the DEIS. Originally, the DEIS steerers shared a power supply with the 860 quadrupole doublet. This was a dual, unipolar supply whose outputs were switched to change polarity. The voltage range spanned was ± 3 kV. The supplies were nonlinear around zero, where they had been used for the DEIS beam, and the voltage was much higher than was useful for steering the beam. The new supplies have an operating range of ± 150 V making the beam tuning much less sensitive with the additional benefit of providing independent supplies for the two ion sources.

A request was made for a high intensity deuteron beam for the Mass 8 Beta Decay experiment. The 11 μamp deuterium beam previously available produced a counting rate that was considered too low for the experiment. The aperture diameter was increased from 0.5 mm to 0.9 mm. This increased the deuterium output to over 30 μamp at the expense of increasing the source operating pressure from 8.0 μTorr to 25.0 μTorr.

An experimenter's request for a ^{64}Ni beam (separated isotope cost $\sim$ \$40 per mg) led to a Ni beam development project on our modified 860*i* sputter source.[1] Middleton[2] reports ionization efficiencies beginning at 4.3% and rising with pit formation to 8% or 9%. For our source, ionization efficiencies over 1% were only achieved at reduced Cs focus potentials (< 1 Kv). Best efficiency was 15% averaged over a 4 1/2 day test run with natural nickel (measuring ^{58}Ni$^-$ beam and correcting for isotopic distribution). The actual experimental run achieved an average efficiency conservatively estimated[3] at over 5% (despite an unnecessary pellet change about half way through the 6 days).

---

[1] This is a General Ionex Corporation Model 860 Negative Ion Sputter Source modified as described in Nuclear Physics Laboratory Annual Report, University of Washington (1988) p. 52.

[2] A NEGATIVE ION COOKBOOK, Roy Middleton, October, 1989, nickel, Z=28.

[3] Only an estimated lower bound for efficiency is given since the ^{64}Ni beam out of the ion source was only measured with open slits infrequently. In particular, >2 microamps of ^{64}Ni beam was seen during tuning when each of the two pellets were new and the experiment ran for 135 hours producing well over 270 microamphours of 64Ni (since nickel beams increase in magnitude and ionization efficiency with pit formation). Total sputtering weight loss of 13.3mg includes only a small amount of aluminum holder.

12 Computer Systems

12.1 Acquisition system developments

E.A. Achterberg,* J.G. Cramer, M.A. Howe, C. Hyde-Wright and R.J. Seymour

Our principal data acquisition system ("Quark") consists of a Digital VAXStation 3200 running VMS v4.7a. We use VWS/UIS as the "windowing" software. The VAXstation supports a BiRa MBD-11 controlled CAMAC crate. The VAXStation's BA-23 cabinet is cabled into a BA-23 CC expansion cabinet, with a MDB DWQ11 Qbus to Unibus converter driving our old PDP 11/60's Unibus expansion bay. Our Qbus peripherals include a CMD CQD-220/TM SCSI adapter, a Seagate ST41650 1.38 gigabyte disk, a TTI CTS-8210 8mm tape drive, a DEC IEQ11 IEEE-488 bus controller, and a DEC DRV11-J. The Unibus bay contains a DR11-C, our Printronix lineprinter controller and a Unibus cable to the MBD-11.

This main CAMAC system contains interface modules for our dozen Tracor Northern TN-1213 ADCs. Those ADCs and other CAMAC modules are controlled by an in-house built synchronization interface, which includes routing-Or capabilities, and 32 10-digit 75 MHz scalers.

Additional CAMAC space is available for our LeCroy 2249's, 2228's and 2551's. We have two FERA 4300B ADCs, and two Phillips 7186 TDC's.

Our acquisition software is based upon TUNL's XSYS, with major modifications to their DISPLAY program.

We have two additional VAX-based acquisition systems. They are now independent systems (they had been a cluster), running the same software as Quark. Each consists of a VAXstation 3200 with an Able Qniverter directly connecting to an MBD-11. There is no Unibus "drawer" required. One has one 630 megabyte disk drive, and the other has two. They are both mounted in roll-around rack cabinets, and can be moved throughout the building as needed. Neither has the main system's complex external interfacing equipment.

During the spring of 1992, we installed our XSYS system at TANDAR, Argentina's vertical tandem Van de Graaff center in Buenos Aires. Some of the enhancements performed in that effort were then brought back to Seattle for incorporation here. These included additional DAP file syntax to allow multi-channel reading from the LeCroy modules, and to specify MBD-monitored delays in event readout.

12.2 Analysis and support system developments

J.G. Cramer M.A. Howe, C. Hyde-Wright and R.J. Seymour

All of our offline analysis VAXes are running VMS v5.5-2. We still have an 8 megabyte VAX 11/780, with connections to twenty-odd local terminals. Our in-house VAX complement now includes the 11/780, three VAXstation 3100/30's, a VAXstation 3100/38, five VAXstation 3200's, and a VAXstation 2000. There are three additional 3200's serving the Nuclear Theory group. One

*Tandem Argentina Lab, Dept. de Fisica-TANDAR-CNEA, Av. Del Liberator 8250, Buenos Aires, Argentina.

VAXstation II/GPX is currently located at SLAC. Three of the 3200's form the Online Acquisition systems described above. One serves as the Linac's control and display system. Those four machines are all still running VMS v4.7. TGV's Multinet provides us with TCP/IP access to Internet. Our principal Internet address is npl.washington.edu. Bitnet access is via the campus central site's VAXes and IBM 3090 system.

This year the offline systems jumped from a mixed collection of VMS versions, ranging from v4.7 through v5.4, to a homogeneous v5.5-2 environment. We also finally joined our off-line analysis VAXes into a single cluster. However, the 11/780 suffered such degradation in perceived performance that we re-isolated it to standalone operation.

Since it was the fastest VAX in the building, the VAXstation 3100/38's was upgraded to 32mb of memory. It serves as a boot node for three other VAXstations.

One VAXstation 3100/30 was brought to 24mb of memory to better support the X windowing system.

TUNL's XSYS is our primary offline analysis package, although we also run two versions of LAMPF's Q on two VAXStations. Conversion programs for other data formats are written on an as-needed basis.

The arrival of the two 40-MIPS HP 9000/710 workstations caused a number of ripples in our system usage patterns. Our 12-MIPS color DECStation 3100, running Digital's Ultrix v4.2, had been primarily used for running Wolfram's Mathematica. Some Monte Carlo programs were also moved to the DECStation. Since the HP's were about four times faster, they drew those programs away from the DECStation. Their sixteen to twenty times speed advantage relative to the VAXes enticed a few more users to migrate programs to the HP Unix environment.

Despite the faster number-crunching available on the HP systems, VMS's user-friendliness still keeps most casual users on the VAXes. In an effort to provide both speed and ease-of-use, we have been evaluating the purchase of a DEC Alpha AXP system. We have had two demonstration systems in-house, a "deskside" DECstation 3000/500, and a "desktop" DECstation 3000/400. The machines performed as advertised. With the 150-MHz 3000/500, we saw the expected fifty times speed increase over the VAXstations. We also experienced a slightly greater than expected improvement over the HP 710's. The 130-MHz 3000/400 performed about 15

We also provide some system management services for the Institute for Nuclear Theory. That remote site has three DECstation 5000/200's, each with 32 Mbytes of memory, color displays, a total of 5 gigabytes of disk, two 4mm DAT drives and a CDrom.

12.3 Migration of CERN and CEBAF software to DEC3100

J.F. Amsbaugh and R.J. Seymour

Several researchers have been running a Monte Carlo event analyzer, FASTMC, on a VAXstation 3100. This software is from the CLAS detector collaboration at the Continuous Electron Beam Facility (CEBAF). The software is written in Fortran77 and modules from the program library distributed by CERN are utilized. The VAXstation uses the VMS 5.2 operating system. It was decided to migrate the software to a color DECstation 3100, a RISC machine running under ULTRIX (Unix), to capitalize on its higher performance.

Simple, one would think, since the DECstation is a Unix workstation supported by CERN and recompilation of code, although taking time, is straightforward. This leaves the onerous problem of resolving the Fortran INCLUDE statement's explicit use of directories, to account for the differences between VMS and Unix. My approach was to explicitly change all file references, for now, so that users could use the program and I could learn the extent of the problem. Later, something would be done to make this automatic and conform with the CLAS software development standard[1]. This migration was much more problematic.

First attempts indicated the ULTRIX operating system should be upgraded to version 4.2 (Rev.96), for current site support and consistency with the CERN program library. This is really a rebuild, not an upgrade. The CERN program library was obtained via FTP and installed. Lastly, the CEBAF source code was copied over, split into small modules, compiled to object modules and arranged into archive libraries. Then what was needed was to edit the main program for input and output names etc., compile an executable, and run.

Many problems were encountered, first the Unix archiver (librarian in VMS) only accepts 14 characters and with subroutine module names like "response_shower.o" this is easily exceeded. Luckily, all the names used were unique in the first 15 characters. Next, the upgrade included changing the Fortran from MIPS ucode f77 Version1 to DEC Fortran for RISC ver3.04. The script that interprets the f77 command line to compile and load from archives to form an executable was unable to find all of the required Fortran libraries. In the end, this was done by hand. The two Fortran's run time libraries also were incompatible in I/O in that a file opened by one could not be read or written to by the other. This necessitated locally compiling the CERN library as well as the CLAS source code. The CERN distribution files lacks all the files needed to completely rebuild the library but was sufficient for FASTMC. The of the code was able to crash the compiler.

Finally, the code ran and the table below is the measured performance for analyzing 100,000 events. In our machination to resolve some issues of versions and compatibility we ported the software to a DECstation 5000/200 at the Institute for Nuclear Theory and it's performance is included.

Performance Analysing 100k Events		
VAXstation 3100	184 min.	optimized
DECstation 3100	64 min.	no-optimize
DECstation 3100	46 min.	optimized
DECstation 5000/200	28 min.	optimized

[1]CLAS Note 90-008

13 Nuclear Physics Laboratory personnel

Faculty

Eric G. Adelberger, Professor
John G. Cramer, Professor
Hans Bichsel, Affiliate Professor
Ludwig de Braeckeleer, Research Assistant Professor[2]
George W. Farwell, Professor Emeritus
Pieter M. Grootes, Research Professor, Geological Sciences and Physics
Isaac Halpern, Professor
Blayne R. Heckel, Associate Professor
Charles E. Hyde-Wright, Assistant Professor
Kurt A. Snover, Research Professor
Derek W. Storm, Research Professor; Director, Nuclear Physics Laboratory
Thomas A. Trainor, Research Associate Professor
Robert Vandenbosch, Professor
William G. Weitkamp, Research Professor; Technical Director, Nuclear Physics Laboratory

Research staff

Azzeddine Elmaanni, Research Associate
Jens H. Gundlach, Research Associate
Mitchell Kaplan, Research Associate[3]
Paul Magnus, Research Associate
Douglas Wells, Research Associate[4]
Yue Su, Research Associate
Danzhao Ye, Research Associate
Zhiping Zhao, Research Associate
Xianzhou Zhu, Research Associate

Predoctoral research associates

James Beck	Ziad Drebi	Gregory Smith
Jeff Bierman	Michael Harris	Alejandro Sonzogni
Thomas A. Brown	Weidong Jiang	Kenneth Swartz
Nick Cabot[4]	S. John Luke[5]	Brian McLain
Pakkin Chan	Michael Kelly	Douglas P. Rosenzweig
Aaron Charlop	Diane Markoff	William Schief[6]

[2]On leave November 1992 through April 1993.
[3]Now at: University of Washington Medical Center, Department of Radiology, Seattle, WA 98195.
[4]Now at: Environmental Radiation Section, Department of Health, Radiation Protection Division, Olympia, WA 98504.

Professional staff

John F. Amsbaugh, Research Engineer
David R. Balsley, Research Scientist[7]
Gregory C. Harper, Research Engineer
Mark A. Howe, Research Engineer
Allan Myers, Electronics Technician
Duncan Prindle, Research Scientist
Richard J. Seymour, Computer Systems Manager
Rod E. Stowell, Electronics Engineer/Electronics Shop Supervisor[8]
H. Erik Swanson, Research Physicist
Timothy D. Van Wechel, Electronics Engineer[9]
Douglas I. Will, Research Engineer

Technical staff

Dean T. Corcoran, Engineering Technician
James Elms, Instrument Maker
Louis L. Geissel, Instrument Maker, Student Shop Leadman
Carl E. Linder, Engineering Technician
Hendrik Simons, Instrument Maker, Shop Supervisor
John A. Wootress, Accelerator Technician

Administrative staff

María G. Ramírez, Administrative Assistant
Karin Hendrickson, Office Assistant

Part time staff

Hazen Babcock	Britt Jud
Sara Chanthaseny	Lawrence Norton
James Evan III	Todd Rudberg
Shawn Golliher	David Wright

[4]Now at: Physics Department, University of Washington, Seattle, WA.
[5]Now at: Lawrence Livermore National Lab, L-397, Livermore, CA 94551.
[6]Now at: University of Washington, Department of Bioengineering, Seattle, WA 98195.
[7]Fully supported by NSF PALE grant.
[8]Retired.
[9]On leave: July 15, 1992 – July 15, 1993.

13.1 Degrees granted, academic year 1992–1993

Ph. D. Degrees:

"High Energy γ ray Emission in Nuclear Reactions: A Tool to Study Nuclear Dynamics?," Stanley John Luke, Ph. D. Thesis, University of Washington, (1992).

"A New Test of the Weak Equivalence Principle," Yue Su, Ph. D. Thesis, University of Washington (1992).

"Experimental study of inclusive pion inelastic scattering and pion photoproduction," Douglas Paul Rosenzweig, Ph. D. Thesis, University of Washington, (1993).

13.2 List of publications from 1993

Published papers:

"Measurements of the electric and magnetic form factors of the neutron from $Q^2 = 1.75$ to 4.00 $(\mathrm{GeV/c})^2$," A. Lung, L. Stuart, P.E. Bosted, L. Andivahis, J. Alster, R.G. Arnold, C.C. Chang, F.S. Dietrich, W. Dodge, R. Gearhart, J. Gomez, K. Griffioen, R. Hicks, C.E. Hyde-Wright, C. Keppel, S. Kuhn, J. Lichtenstadt, R. Miskimen, G.A. Peterson, G.G. Petratos, S.E. Rock, S. Rokni, W.K. Sakumoto, M. Spengos, K. Swartz, Z. Szalata, and L.H. Tao, Phys Rev Lett, **70** 718, (1993).

"N^* Electroproduction and propagation in nuclei," L.B. Weinstein, J. Morrison, A. Perry, H. Baghaei, W. Bertozzi, W.U. Boeglin, J.M. Finn, J. Glickman, C.E. Hyde-Wright, N. Kalantar-Nayestanaki, R.W. Lourie, J.A. Nelson, S. Penn, W.W. Sapp, C.P. Sargent, P.E. Ulmer, B. H. Cottman, L. Ghedira, E.J. Winhold, J.R. Calarco, J. Wise, P. Boberg, C.C. Chang, N.S. Chant, P.G. Roos, D.Chang, K. Aniol, M.B. Epstein, D.J. Margaziotis, C. Perdrisat, V. Punjabi, R. Whitney, Phys Rev **C47** 225–230 (1993).

"Measurements of νW_2 and $R = \sigma_L/\sigma_T$ from inelastic electron-aluminum scattering near $x = 1$," P.E. Bosted, A. Lung, L. Andivahis, L. Stuart, J. Alster, R.G. Arnold, C.C. Chang, F.S. Dietrich, W. Dodge, R. Gearhart, J. Gomez, K. Griffioen, R. Hicks, C.E. Hyde-Wright, C. Keppel, S. Kuhn, J. Lichtenstadt, R. Miskimen, G.A. Peterson, G.G. Petratos, S.E. Rock, S. Rokni, W.K. Sakumoto, M. Spengos, K. Swartz, Z. Szalata, and L.H. Tao, Phys Rev **C46** 2505–2515 (1992).

"Measurements of the Electric and Magnetic Form Factors of the Proton from $Q^2 = 1.75$ to 8.83 $(\mathrm{GeV/c})^2$," P.E. Bosted, L. Andivahis, A. Lung, L. Stuart, J. Alster, R.G. Arnold, C.C. Chang, F.S. Dietrich, R. Gearhart, J. Gomez, K. Griffioen, R. Hicks, C.E. Hyde-Wright, C. Keppel, S. Kuhn, J. Lichtenstadt, R. Miskimen, G.A. Peterson, G.G. Petratos, S. Rock, S. Rokni, W. Sakumoto, M. Spengos, K. Swartz, Z. Szalata, and L.H. Tao, Phys Rev Lett, **68** 3841–3844 (1992).

"Contribution of the induced tensor form factor to the A=8 β, ν, α angular correlation," L. DeBraeckeleer, Phys. Rev. C. **45** 1935 (1992).

"Reexamination of an anomaly in near-threshold pair production," L. DeBraeckeleer, E.G. Adelberger and A. García, Phys. Rev. A **46** R5324, (1992).

"Recent results from experiment NA35," NA35 Collaboration (P. Seyboth *et al.*, Nucl. PHys. **A544** 293c, (1992).

"Production of charged kaons in central S+S and O + Au collisions at 200-GEV/nucleon," NA35 Collaboration, CERN-NA-035 Experiment, M. Kowalski *et al.*, Nucl. Phys. **A544**, 609c, (1992).

"Pion interferometry in ultrarelativistic nuclear collisions," NA35 Collaboration, CERN-NA-035 Experiment, D. Ferenc *et al.*, Nucl. Phys. **A544**, 531c, (1992).

"Comparison of inclusive inelastic scattering of π^+ and π^- from nuclei at 100 MeV," D.P. Rosenzweig, J.F. Amann, R.L. Boudrie, K.G.R. Doss, D.M. Drake, I. Halpern, M.A. Khandaker,

J. Nelson, D.W. Storm, D.R. Tieger and S.A. Wood, Phys. Rev. C **46** 1968, (1992).

"Interplay between pion absorption and inclusive-inelastic scattering on hydrogen and helium isotopes for 96.5 MeV kinetic energy pions," D.W. Storm, Few Body Systems, Suppl. 5, 219-224 (1992).

"Radiocarbon AMS dating of pollen extracted from peat samples," T.A. Brown, G.W. Farwell, P.M. Grootes and F.H. Schmidt, Radiocarbon, **34**, 550, (1992).

"Evidence for a shape change of hot, fast rotating ^{45}Sc nuclei from GDR studies," M. Kicinska-Habior and K.A. Snover, Proc. of the 27th Zakopane School of Physics, Zakopane, Poland, 1992, Acta Polonica B **24** 433 (1993).

"Comparison of giant dipole resonance decay in stiff ^{90}Mo and soft ^{100}Mo excited nuclei," M. Kicinska-Habior, K.A. Snover, J.A. Behr, C.A. Gossett, J.H. Gundlach and G. Feldman, Phys. Rev. C **45** 569, (1992).

"Angular momentum distributions in subbarrier fusion reactions," R. Vandenbosch, Annu. Rev. Nucl. Part. Sci. 42:447-481, (1992).

"Critical angular momentum of cluster evaporation: ^{16}O(^{16}O,α)^{28}Si and ^{16}O(^{16}O,^{8}Be)^{24}Mg," J. Czakanski, W. Zipper, M. Siemaszko, W. Dünnweber, W. Hering, D. Konnerth, W. Trombik, K.G. Bernhardt, H. Bohn, K.A. Eberhard and R. Vandenbosch, Nuclear Physics **A542** 278-294 (1992).

"Fusion yields for carbon-cluster impact on CD_2 targets," R. Vandenbosch, D. Ye, J. Neubauer, D.I. Will and T.A. Trainor, Phys. Rev. A **46** 5741, (1992).

"High energy γ rays from ^{14}N + $^{\mathrm{nat}}$Ag at 35 MeV/nucleon," S.J. Luke, R. Vandenbosch, W. Benenson, J. Clayton, K. Joh, D. Krofcheck, T.K. Murakami and J.D. Stevenson, Phys. Rev. C **47** 1211, (1993).

"Δ contribution to the paramagnetic polarizability of the proton," N.C. Mukhopadhyay, A.M. Nathan, L. Zhang, Phys. Rev. D. **47**, R7, (1993).

"Test of the equivalence principle for ordinary matter falling toward dark matter," G. Smith, E.G. Adelberger, B.R. Heckel and Y. Su, Phys. Rev. Lett. **70**, #2, (1993).

"Comment on "Is the weak axial-vector current renormalized in nuclei?"," D.P. Wells, E.G. Adelberger, P.V. Magnus, A. García, Phys. Rev. Lett. 69, 2446, (1992).

"Isomer-to-isomer beta decay of ^{180}Hf^{m} and the nucleosynthesis of ^{180}Ta^{m}," S.E. Kellogg and E.B. Norman, Phys. Rev. C **46** 1115, (1992).

Papers submitted or to be published:

"Impact parameter dependence of pre-equilibrium particle emission," D.J. Prindle, R. Vandenbosch, S. Kailas, A.W. Charlop, and C.E. Hyde-Wright, submitted to Phys Rev C, November 1992.

“Measurement of the magnetic form factor of the neutron,” P. Markowitz, J.M. Finn, B.D. Anderson, H. Arenhovel, A.R. Baldwin, D. Barkhuff, K. Beard, W. Bertozzi, J.M. Cameron, C.C. Chang, G.W. Dodson, K. Dow, T. Eden, M Farkondeh, B. Flanders, C. Hyde-Wright, W. Jiang, D. Keane, J.J. Kelly, W. Korsch, S. Kowalski, R. Lourie, R. Madey, D.M. Manley, J. Mougey, B. Ni, T. Payerle, P. Pella, T. Reichelt, R.M. Rutt, M. Spraker, D Tieger, W. Turchinetz, P.E. Ulmer, S. Van Verst J.W. Watson, L. Weinstein, R.R. Whitney, W.M. Zhang, submitted to Phys Rev Lett, October 1992.

“Refinements of the nucleon-exchange transport model for the emission of hard photons and nucleons,” S.J. Luke, R. Vandenbosch, J. Randrup, submitted to Phys. Rev. C.

“Rotational state populations in ^{16}O + ^{154}Sm near-barrier fusion,” J.D. Bierman, A.W. Charlop, D.J. Prindle, R. Vandenbosch and D. Ye, submitted to Phys. Rev. C.

“Accelerator calibration of solar neutrino detectors,” E.G. Adelberger, L. DeBraeckeleer, W.C. Haxton and K.A. Snover, submitted to Phys. Lett.

“Statistical gamma decay of the giant dipole resonance in highly excited ^{46}Ti and ^{52}Cr, G. Feldman, K.A. Snover, J.A. Behr, C.A. Gossett, J.H. Gundlach and M. Kicinska-Habior, Phys. Rev. C., in press.

“Search for a phase transition in the nuclear shape at finite temperature and rapid rotation,” M. Kicinska-Habior, K.A. Snover, J.A. Behr, C.A. Gossett, Y. Alhassid and N. Whelan, Phys. Lett., to be published.

“Restoration of isospin symmetry in highly excited compound nuclei,” J.A. Behr, K.A. Snover, C.A. Gossett, M. Kicinska-Habior, J.H. Gundlach, Z.M. Drebi, M.S. Kaplan and D.P. Wells, Phys. Rev. Lett., to be published.

“Potentials that permit a uniqueness theorem,” D.F. Bartlett and Y. Su, submitted to Physical Review E.

“Intra-annual variability of the radiocarbon content of corals from the Galapágos Islands,” T.A. Brown, G.W. Farwell, P.M. Grootes, F.H. Schmidt and M. Stuiver, Radiocarbon **35(2)**, 1993, in press.

Published conference proceedings and invited talks:

“Further studies of belt properties,” W.G. Weitkamp, Symposium of North Eastern Accelerator Personnel, Hull Ontario, September 22, 1992.

“Recent results on giant dipole decay in highly excited nuclei,” K.A. Snover, Proceedings of the Conference on Future Directions in Nuclear Physics with 4π Gamma Detection Systems of the New Generation, Strasbourg, France, 1991, AIP Conf. Proc. **259** 299 (1992).

Abstracts and other conference presentations:

“Photo-production of strangeness on nuclei at CEBAF,” C.E. Hyde-Wright, Colloquium, March 3, 1993, Department of Physics, Old Dominion University, Norfolk VA.

“Virtual compton scattering,” C.E. Hyde-Wright, Invited talk, Workshop for a Future European Electron Accelerator, Clermont-Ferrand, France, June 1992.

“Photo-production of strangeness on nuclei at CEBAF,” C.E. Hyde-Wright, Nuclear Physics Seminar, April 1, 1993, Department of Physics, George Washington University, Washington DC.

“Looking for protons in the nucleus, quasi-elastic electron scattering,” C.E. Hyde-Wright, Nuclear Physics Seminar, April 2, 1993, Department of Physics, Carnegie Mellon University, Pittsburgh PA.

“Evidence for a shape change of hot, fast rotating ^{45}Si nuclei from GDR studies,” M. Kicinska-Habior and K.A. Snover, 27th Zakopane School of Physics, Zakopane, Poland, Aug–Sept. 1992.

“New constraints on composition dependent interactions with ranges down to 1 cm,” J.H. Gundlach, Proceedings of the Moriond Workshop, 1993.

“AMS Radiocarbon dating of pollen from lake sediments,” G.W. Farwell, T.A. Brown and P.M. Grootes, PALE Conference, Vladivostok, Russia, March 24–27, 1993 (Sponsored by the National Science Foundation and the Russian Academy of Sciences).

“^{14}C AMS dating of pollen from lake sediments and peat deposits,” T.A. Brown, G.W. Farwell and P.M. Grootes, 23rd Arctic Workshop, Arpil 2–4, 1993, Byrd Polar Research Center, Columbus, OH.

“The giant dipole resonance at high excitation energy and spin,” K.A. Snover, Proc. of the Internat. Nucl. Phys. Conf., Wiesbaden, Germany, July 26–August 1, 1992, Nucl. Phys. **A553**, 153c (1993) (invited paper).

“Giant dipole resonance in highly excited nuclei,” K.A. Snover, Gordon Conference on Photonuclear Reactions, Tilton, NH, August 1992.

“Autocorrelation multiplicity trigger,” T.A. Trainor, Quark Matter ’93, Tenth International Conference on Ultra-Relativistic Nucleus-Nucleus Collisions, June 20-24, 1993 Borlänge, Sweden

“Comparison of “candidate” 3-body Coulomb corrections to HBT,” J.G. Cramer and V. Efimov, Quark Matter ’93, Tenth International Conference on Ultra-Relativistic Nucleus-Nucleus Collisions, June 20-24, 1993 Borlänge, Sweden

“Nuclear Fission,” “Heavy Ion Fusion,” “Cluster Impact Fusion,” R. Vandenbosch, RIKEN, Winter School on Nuclear Physics, Yuzawa, Japan, February, 1993.

Other reports and proposals

“A proposal for the upgrade of the University of Washington Nuclear Physics Laboratory Tandem Accelerator,” W.G. Weitkamp, August 28, (1992).

FRONT ROW: Z. DREBI, J. BECK, G. SMITH, M. HARRIS, C. LINDER, K. HENDRICKSON, B. WEITKAMP, A. CHARLOP

SECOND ROW: A. ELMAANNI, J. GUNDLACH, X. ZHU, M. RAMIREZ, Y. SU, L. GEISSEL, D. MARKOFF, D. PRINDLE, H. BABCOCK, B. JUD, A. MEYERS, S. CHANTHASENY, E. SWANSON, Z. ZHAO

THIRD ROW: H. SIMONS, R. VANDENBOSCH, J. WOOTRESS, J. ELMS, P. CHAN, G. HARPER, D. CORCORAN, J. AMSBAUGH, P. MAGNUS, D. ROSENZWEIG, Y. HALPERN, B. MCLAIN, T. RUDBERG, J. BIERMAN, B. HECKEL, A. SONZOGNI, M. HOWE, R. SEYMOUR, W. JIANG, G. FARWELL, D. BALSLEY, P. GROOTES, D. STORM, J. CRAMER